Two-photon production of charged meson pairs at LEP

Katarzyna Grzelak

A thesis submitted for the degree of Doctor of Philosophy in Physics at the Warsaw University

Institute of Experimental Physics
Warsaw 2000

Supervisor: Prof. Krzysztof Doroba

Abstract

The cross-sections for the two-photon production of charged pion and kaon pairs have been measured using data collected by the DELPHI detector at LEP at e^+e^- centre-of-mass energies $\sqrt{s}$=91 GeV and $\sqrt{s}$=183 GeV. The cross-sections have been measured at invariant masses of the two-photon system above 1.6 GeV for the kaon and above 1.5 GeV for the pion final state, and for meson's scattering angles in the photon-photon centre-of-mass system in the region $|cos\theta^*| < 0.6$. The detailed study of background of muon pairs and trigger efficiency, crucial for this analysis has been performed. The obtained cross-sections have been compared with various theoretical models. The results for kaons agree well with leading order QCD calculations and are not described by QED-based models. In the contrary, the pion data exhibit more complex structure. The perturbative QCD models alone are not sufficient to describe the observed spectra.

The presented measurements are the first results from LEP concerning the exclusive two-photon production of charged kaon and pion pairs in the region of high invariant masses.

Glossary of terms

- ***** - denotes variables in $\gamma\gamma$ CMS system
- $_{\mathbf{true}}$ - denotes variables at the generator level
- $_{\mathbf{meas}}$ - denotes variables after detector simulation
- $_{\mu}{}^{\nu}$ - Lorentz indexes, $\mu, \nu = 0{,}3$
- $_{ab}$ - helicity indexes, $a, b = 0{,}+{,}-$ $(0{,}1{,}-1)$
- **X** - $\gamma\gamma$ final state
- $\mathbf{A}, \mathbf{B}$ - groups of trigger functions
- **Br** - branching ratio
- **CF** - logical combination of TDLs in terms of logical ORs and ANDs
- **CMS** - Centre-of-mass system
- **dE/dx** - Specific ionisation of a track
- **DF** - trigger Decision Function - logical product of TFs
- $\mathbf{d\Gamma_X}$ - phase-space volume element of final state X
- $\mathbf{d\Gamma}$ - phase-space volume element of the scattered particles
- $\mathbf{D_{J_z}}$ - resonance decay amplitude
- $\mathbf{d\Omega}$ - solid angle element
- **EMF** - Electromagnetic Forward Calorimeter
- **FCA** - Forward Chamber A
- **FCB** - Forward Chamber B
- $\mathbf{g}^{\mu\nu}$ - metric tensor
- **HCAL** - Hadron Calorimeter
- **HPC** - Heavy Projection Chamber
- **ID** - Inner Detector
- $\mathbf{Imp_{r\phi}}$ - distance of closest approach of the track to the electron beam collision point in the $r\phi$ plane
- $\mathbf{Imp_z}$ - distance of closest approach of the track to the electron beam collision point along the z-axis
- **J** - spin of the resonance
- $\mathbf{J_X}$ - total angular momentum of the final state X

- $\mathbf{J_z}$ - spin-projection along an arbitrarily defined z-axis
- $\mathbf{k_j} = (\epsilon_\mathbf{j}, \vec{\mathbf{k_j}})$ - four-momentum of a j-th produced particle; $\epsilon_j \equiv k_j^0$ - notation used in theoretical part
- L - Instantaneous luminosity
- $\mathcal{L}$ - Integrated luminosity
- $\mathcal{L}_{\gamma\gamma}$ - $\gamma\gamma$ luminosity function
- $\mathbf{L}$ - spatial orbital angular momentum of the final state
- $\mathbf{M}^{\mu\nu}$ - amplitude for the transition $\gamma\gamma \to X$
- $\mathbf{M_{ab}}$ - amplitude for the transition $\gamma\gamma \to X$ in the $\gamma\gamma$ helicity basis
- $\mathbf{M}/\overline{\mathbf{M}}$ - meson/anti-meson
- **majority** - the logical OR of possible coincidences of TFs inside a decision function
- $\mathbf{M_R}$ - mass of the resonance
- **MWPC** - Multi-Wire Proportional Chamber
- $\mathbf{N_{ab}}$ - resonance formation amplitude
- **OD** - Outer Detector
- $\mathbf{p} = (\mathbf{E}, \vec{\mathbf{p}})$ - four-momentum of the produced particle - notation used in part concerning data analysis
- $\mathbf{p_i} = (\mathbf{E_b}, \vec{\mathbf{p_i}})$ - four-momentum of beam particle, i=1,2
- $\mathbf{p_i^{'}} = (\mathbf{E_i^{'}}, \vec{\mathbf{p_i}}^{'})$ - four-momentum of deflected electron (positron), i=1,2
- $\mathbf{q_i} = (\mathbf{E_{\gamma i}}, \vec{\mathbf{q_i}})$ - four-momentum of a photon, i=1,2
- $\mathbf{p_T}$ - transverse momentum
- $\mathbf{P_T^2}$ - total transverse momentum squared for the event
- $\mathbf{Q}$ - particle's charge
- $\mathbf{Q^2} \equiv -\mathbf{q^2}$ - four-momentum transfer, photon virtuality
- **QCD** - Quantum Chromodynamics
- **QED** - Quantum Electrodynamics
- **RICH** - Ring Imaging Cherenkov Detector
- $\sqrt{\mathbf{s}}$ - e^+e^- centre-of-mass energy
- **SAT** - Small Angle Tagger
- **STIC** - Small Angle Tile Calorimeter

- $\mathbf{T_H}$ - hard scattering amplitude
- **TDL** - Trigger Data Line - trigger signal from the subdetector
- **TF** - logical product of CFs
- **TPC** - Time Projection Chamber
- **VD** - Vertex Detector
- **VFT** - Very Forward Tracker
- $\mathbf{W}_{\gamma\gamma}$ - invariant mass of $\gamma\gamma$ system
- $\mathcal{W}^{\mu'\nu'\mu\nu}$ - elements of tensor describing the final state X.
- $\mathcal{W}_{\mathbf{a'b'ab}}$ - elements of tensor describing the final state X in the $\gamma\gamma$ helicity basis
- **x,y** - fractions of meson's momentum carrying by one of the valence quarks
- $\mathbf{Y_J^\lambda}(\theta^*, \phi^*)$ - spherical harmonic function
- α - electromagnetic coupling constant
- $\alpha_\mathbf{s}$ - strong coupling constant
- β^* - particle velocity in $\gamma\gamma$ CMS
- $\Gamma_\mathbf{tot}$- total width of the resonance
- $\Gamma_{\gamma\gamma}$ - radiative width
- δ - intrinsic phase difference between the resonance and the Born amplitude
- $\Delta\mathbf{E}$ - energy uncertainty
- $\Delta\mathbf{p}$ - momentum error
- $\Delta\mathbf{t}$ - time uncertainty
- $\Delta\phi$ - angle between the tracks in the $r\phi$ plane
- $\Delta\eta$ - angle between the tracks in the three dimensions
- $\varepsilon_\mathbf{K}$ - kaon identification efficiency
- ε_μ - muon identification efficiency
- $\varepsilon_\mathbf{cf} = \frac{\mathbf{1}}{\mathbf{c_f}}$ - c_f is a correction factor due to existence of noise in the calorimeters
- $\varepsilon_\mathbf{MC}$ - detector efficiency, determined by Monte Carlo simulation - includes identification and reconstruction efficiency
- $\varepsilon_\mathbf{t}$ - trigger efficiency
- $\varepsilon = \varepsilon_\mathbf{t}\varepsilon_\mathbf{MC}\varepsilon_\mathbf{cf}$ - total efficiency

- $\varepsilon_{\mathbf{A}}$,$\varepsilon_{\mathbf{B}}$ - efficiencies of accepting a given kind of events by the trigger groups A and B, respectively.
- ζ - relative phase between the resonance and the Born amplitude
- θ - polar angle relative to z-axis
- $\theta^*_{\mathbf{z}}$ - angle between one of the final state particles (here positive particle was chosen) and the beam axis in the $\gamma\gamma$ centre-of-mass system
- $\theta^*_{\mathbf{c}}$ - angle between positive particle (pion,kaon,muon) and the flight direction of CMS in the $\gamma\gamma$ centre-of-mass system
- θ^* - angle between positive particle (pion,kaon,muon) and the photon direction in the $\gamma\gamma$ centre-of-mass system; in the chapter concerning data analysis, θ^* is approximated by θ^*_z
- $\rho^{\mu\nu}_{\mathbf{i}}$ - photon density matrix elements
- $\rho^{\mathbf{ab}}_{\mathbf{i}}$ - photon density matrix elements, $\gamma\gamma$ helicity basis
- $\sigma_{\alpha\beta}$ - cross-sections for interactions between transverse or longitudinal photons, $\alpha, \beta = \mathrm{T}, \mathrm{L}$
- $\sigma_{\gamma\gamma}$ - cross-section for interactions of real photons
- ϕ - azimuthal angle around the z-axis
- Φ - angle between electron and positron scattering planes
- $\phi_{\mathbf{M}}$ - probability amplitude for finding valence partons in a meson

Contents

List of Figures

List of Tables

Chapter 1

Introduction

In classical electrodynamics, due to the linearity of Maxwell's equations, electromagnetic waves cannot interact one with the other. However, in quantum electrodynamics such interactions can occur thanks to the Heisenberg uncertainty principle, described by the formula $\Delta E \Delta t \gtrsim \hbar$. According to this principle, a photon is allowed to violate the energy conservation rule by an amount of energy ΔE for a period of time Δt and to fluctuate into a system of charged objects Y carrying the same quantum numbers as the photon, $\gamma \to Y \to \gamma$. If the system Y is, for example, a pair of leptons and during such a fluctuation one of the leptons meets on its way another photon, the interaction between them can occur and new particles can be produced. For small energies of the photons, however, the cross-sections are extremely small. For example, for light of the wavelength 633 nm, the cross-section is about 4×10^{-31} nb. The situation changes above the threshold for the production of electron-positron pairs. The cross-section is rising rapidly to achieve typical values of few hundred nanobarns for the photon-photon centre-of-mass energies in GeV region [1].
Such highly energetic photons are provided by electron-positron accelerators. Each electron or positron, circulating in the beam pipe of an accelerator, can radiate virtual photon within a time limited by the uncertainty principle. In the laboratory system, these photons have small polar angles with respect to the beam axis. As a consequence, in e^+e^- accelerators we have also two colliding beams of quasi-real photons.
Contrary to the electron-positron interactions which take place in e^+e^- accelerators, photons usually do not have equal energies and the laboratory system is not identical with the $\gamma\gamma$ centre-of-mass system. As a result, a significant number of particles is produced at small polar angles with respect to the beam axis.
The continuous spectra of the photon energies allow simultaneous measurements at different $\gamma\gamma$ invariant masses. Events with different momentum transfers and different polarisations of the photons can be studied at the same time. Since the photon has charge-conjugation quantum number $C = -1$, in photon-photon collisions only resonant states with $C = +1$, forbidden in e^+e^- annihilation, can be produced. Because of the energy considerations, most of the photons have small virtuality.
In this thesis the interactions of such quasi-real photons have been studied. From the experimental point of view it means that scattered electron and positron were deflected by such a small angle that they remained undetected[1]. In particular, events with two charged particles (pions or kaons) in the final state have been investigated.
The data used in this thesis were collected by the DELPHI experiment at Large Elec-

[1]Such events are often called untagged.

tron Positron Collider (LEP) at the e^+e^- centre-of-mass energies $\sqrt{s} = 91$ GeV and $\sqrt{s} = 183$ GeV. As at present, LEP is the biggest e^+e^- accelerator with the highest beam energies, it is a source of the most energetic photons and gives the possibility to study two-photon interactions in previously not explored kinematical range.

Studying such a simple final state as production of pairs of charged particles can bring knowledge about different physical phenomena, depending on the photons energy. At low energy, the photon has long wavelength, sees the final state hadron as a point-like particle and couples to its electric charge. As the energy increases and the wavelength of the photon shortens, it sees the valence quarks and causes them to resonate. For quasi-real photons, the formation of a single resonance R by the collision of two photons is the inverse process to a radiative decay. Therefore, the cross-section $\sigma(\gamma\gamma \to R)$ is a measure of radiative decay width of the particle R.

When the energy increases still further, we reach the region which can be described by perturbative QCD.

Unfortunately, simplicity of the final state does not go with the simplicity of the measurement, especially in the detector designed to study Z^0 physics. Firstly, the trigger system in the DELPHI experiment has not been optimised for untagged gamma-gamma physics. As a consequence for most of the time there was not a dedicated trigger for untagged, low p_T and low multiplicity $\gamma\gamma$ events which in great number were definitely lost. The remained two-prong $\gamma\gamma$ events were accepted by different trigger functions in different periods of time. The trigger conditions were changing several times during each year. As trigger simulation in DELPHI does not exist, finding of the trigger efficiency became one of the crucial points of this analysis.

As the two-photon physics is untypical for the DELPHI experiment, there are not centrally created Monte Carlo samples needed for such an analysis. Therefore all used Monte Carlo samples were created by the author of this thesis, starting from installation of DELPHI simulation and reconstruction program in Warsaw on two UNIX systems: IRIX and HP-UX.

A significant experimental complication in the measurement of the process $e^+e^- \to e^+e^-\pi^+\pi^-$ is a high background from lepton pair production, which is in large extent irreducible. As the pion mass is similar to that of the muon, particle identification techniques based on difference in particles masses are ineffective in distinguishing $\pi^+\pi^-$ and $\mu^+\mu^-$ final states. In this thesis, the emphasis has been put on the study of hardly known region of high invariant masses in which perturbative QCD-based models can be tested. From the theoretical point of view, two-photon interactions provide the perfect initial state for studying QCD exclusive hard scattering as the simple point-like and colourless initial state allows to calculate two-photon cross-sections at large momentum transfer assuming neither photon structure function nor initial state interactions.

However, limited high-mass statistics and existence of high muon background caused very few collaborations to attempt this measurement. In particular, these are the first results from LEP. The cross-section for the production of charged kaon pairs and charged pion pairs have been measured as a function of the photon-photon invariant mass and cosine of the polar angle θ^* at which the mesons are produced in the $\gamma\gamma$ centre-of-mass system and compared to the theoretical predictions.

The production of charged pions and kaons in two-photon interactions became the field of interest of physicists even before the first e^+e^- storage rings were commissioned [2]. The first results concerning the exclusive production of charged hadron pairs come from early eighties and concern principally the production of the resonance $f_2(1270)$ in the channel

$\gamma\gamma \to f_2 \to \pi^+\pi^-$.
With an increase of two-photon luminosity and the energy of photons, came the possibility of an investigation of the high invariant mass region, beyond 1-2 GeV. Production of high invariant mass continuum has been studied by the three experiments: MARK II [3], TPC/Two–Gamma [4] and CLEO [5]. The last two collaborations measured the combined K^+K^- and $\pi^+\pi^-$ cross-sections while the TPC/Two–Gamma was the only experiment to measure these cross-sections separately.
The future of $\gamma\gamma$ physics, including the study of $\gamma\gamma \to \pi^+\pi^-(K^+K^-)$ channel is in planned Linear Collider and at present new results can be expected from B-factories.
This thesis is organised as follows:

- **Chapter Two** provides a brief introduction to the kinematics and theory of photon-photon interactions. Emphasis is placed upon the areas directly relevant to this thesis, namely exclusive production of meson and lepton pairs.

- **Chapter Three** provides a short description of the LEP accelerator and the components of the DELPHI detector relevant to the analysis performed in this thesis. In particular it contains description of the trigger system and off-line data processing structure.

- **Chapter Four** presents Monte Carlo generators and detector simulation program used in the analysis. It contains a discussion of generator parameters and describes some modifications of the generators.

- The main part of the analysis is described in **Chapter Five**. It starts from a description of a two-prong selection and discussion of particle identification, presents the importance of understanding the trigger efficiency, describes the method of finding this efficiency and corresponding results. Then, the calibration process, production of muon pairs in photon-photon collisions is checked for all considered data samples. The next part concerns production of kaon and pion pairs in the high invariant mass region and a discussion of possible backgrounds. The operational status of the DELPHI detector during the relevant data taking periods, as well as final luminosities used in this analysis are also discussed.

- **Chapter Six** contains final results concerning cross-sections for two-photon production of kaon and pion pairs, discussion of systematic errors.

- **Chapter Seven** contains the conclusions.

Chapter 2

Theory of photon-photon interactions

2.1 Introduction

In this chapter the theoretical framework that is needed for the understanding of photon-photon reactions at e^+e^- colliders is described. Emphasis is placed upon interactions of quasi-real photons leading to two-meson final states, what is directly relevant to the measurements performed in this thesis. More general reviews of the two-photon physics are given by Budnev et al. [2], Kolanoski [6], Poppe [7], Nisius [8], Berger and Wagner [9], Altarelli et al. [10].

2.2 The kinematics

The kinematical quantities for the reaction $e^+e^- \to e^+e^-X$, proceeding via the exchange of two photons, are depicted in Fig.2.1.

The colliding particles, electron and positron, have four-momenta denoted by p_i. Radiating a photon, i-th lepton is deflected by an angle θ_i with respect to the beam axis and has four-momentum $p_i^{'}$. Four-momenta of the photons are denoted by $q_i = p_i - p_i^{'}$. The photons have negative virtualities $q^2 \leq 0$, but for simplicity the positive quantity $Q^2 \equiv -q^2 \geq 0$ is commonly used. For unpolarised beams there are only five variables needed to determine the $\gamma\gamma$ system: energies $E_i^{'} \equiv p_i^{'0}$ of the scattered leptons, their polar angles θ_i and the angle Φ between electron and positron scattering planes. The photon energies expressed in terms of the scattered leptons are:

$$E_{\gamma i} = E_b - E_i^{'}$$

where E_b is the beam energy. The virtual photon masses squared are given by:

$$\begin{aligned} Q_i^2 &\equiv -q_i^2 = -(p_i - p_i^{'})^2 \\ &= -2m_e^2 + 2E_bE_i^{'}\left\{1 - \sqrt{1-\left(\frac{m_e}{E_b}\right)^2}\sqrt{1-\left(\frac{m_e}{E_i^{'}}\right)^2}\cos\theta_i\right\} \\ &= 2E_bE_i^{'}(1-\cos\theta_i) + m_e^2\frac{-2E_bE_i + (E_i^{'2}+E_b^2)\cos\theta_i}{E_bE_i^{'}} + O\left(\frac{m_e^4}{E_b^2}\right) \qquad (2.1) \end{aligned}$$

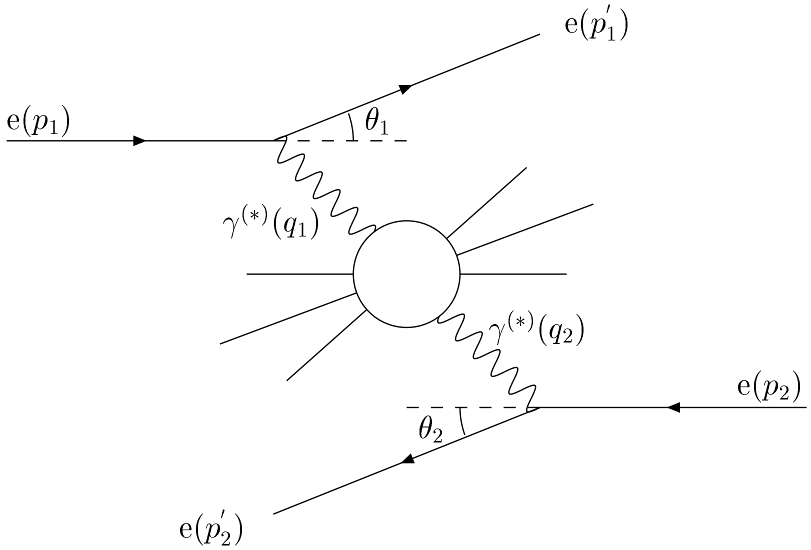

Figure 2.1: A diagram of the reaction $e^+e^- \to e^+e^-X$. The four-momenta of electron and positron before and after interaction are denoted by $p_i = (E_b, \vec{p_i})$ and $p_i^{'} = (E_i^{'}, \vec{p_i}^{'})$ respectively. Four-vectors of the photons are denoted by $q_i = (E_{\gamma i}, \vec{q_i})$.

For $E_i^{'} \gg m_e$ the above equation reduces to:

$$Q_i^2 \approx 2E_bE_i^{'}(1 - \cos\theta_i) + Q^2_{i\ min} \tag{2.2}$$

Since the scattering angles are essentially very small, the electron mass terms cannot always be neglected. In particular, for θ_i close to 0, the minimum photon virtuality is:

$$Q^2_{i\ min} = \frac{m_e^2(E_b - E_i^{'})^2}{E_bE_i^{'}} \tag{2.3}$$

The invariant mass of the $\gamma\gamma$ system, neglecting terms of the order of m_e^2, is given by:

$$W^2_{\gamma\gamma} = (q_1 + q_2)^2 \simeq 4E_{\gamma_1}E_{\gamma_2} - 2E_1^{'}E_2{'}(1 - \cos\theta_1\cos\theta_2 - \sin\theta_1\sin\theta_2\cos\Phi) \tag{2.4}$$

2.3 The $e^+e^- \to e^+e^-X$ cross-section

The cross-section for two-photon production of a system X can be written as [2]:

$$\begin{aligned} d\sigma(e^+e^- \to e^+e^-X) = & \frac{(4\pi\alpha)^2}{q_1^2q_2^2}\rho_1^{\mu\mu^{'}}\rho_2^{\nu\nu^{'}}M^{*\mu^{'}\nu^{'}}M^{\mu\nu} \times \\ & \times \frac{(2\pi)^4\delta(q_1 + q_2 - k)d\Gamma_X}{4\{(p_1p_2)^2 - m_e^2m_e^2\}^{1/2}}\frac{d^3p_1^{'}d^3p_2^{'}}{2E_1^{'}2E_2^{'}(2\pi)^6} \end{aligned} \tag{2.5}$$

where $M^{\mu\nu}$ is the amplitude for the transition $\gamma\gamma \to X$, $k = \sum_j k_j = q_1 + q_2$ is the total four-momentum of the final state X with mass $W = \sqrt{k^2}$ and the phase-space volume element $d\Gamma_X = \prod_j d^3k_j/2\epsilon_j(2\pi)^3$. The j-th produced particle has four-momentum k_j and energy $\epsilon_j \equiv k_j^0$.

The quantity ρ_i is a density matrix for virtual photon, generated by the i-th particle. For electron and positron beams, the matrix elements are:

$$\rho_i^{\mu\nu} = -\left(g^{\mu\nu} - \frac{q_i^\mu q_i^\nu}{q_i^2}\right) - \frac{(2p_i - q_i)^\mu (2p_i - q_i)^\nu}{q_i^2} \tag{2.6}$$

where the metric tensor $g^{\mu\nu}$ has components $g^{00} = 1$ and $g^{ii} = -1,\ i = 1..3$. This matrix is non-diagonal, what means that the virtual photons are polarised. The quantity α is the electromagnetic coupling constant.

After integration over the phase-space volume of the final state X, the expression for the cross-section can be written as:

$$d\sigma(e^+e^- \to e^+e^- X) = \frac{(4\pi\alpha)^2}{4\{(p_1p_2)^2 - m_e^2 m_e^2\}^{1/2}} \rho_1^{\mu\mu'} \rho_2^{\nu\nu'} \frac{1}{q_1^2 q_2^2} \mathcal{W}^{\mu'\nu'\mu\nu} d\Gamma \tag{2.7}$$

where tensor

$$\mathcal{W}^{\mu'\nu'\mu\nu} = \frac{1}{2}\int M^{*\mu'\nu'} M^{\mu\nu} (2\pi)^4 \delta(q_1 + q_2 - k) d\Gamma_X \tag{2.8}$$

describes the production of the final state X, the terms $1/q_1^2$ and $1/q_2^2$ are photon propagators which cause the photons to be predominantly quasi-real and radiated at small angles relative to the beam. The remaining terms represent vertices in which photons are produced. The phase-space volume element of the scattered particles (electrons and positrons) is:

$$d\Gamma \equiv \frac{d^3p_1' d^3p_2'}{2E_1' 2E_2' (2\pi)^6}$$

The tensor $\mathcal{W}^{\mu'\nu'\mu\nu}$ cannot be calculated rigorously for hadronic final states. It has 256 components, but taking into account Lorentz invariance, gauge invariance and T-invariance (symmetry in the substitution $\mu'\nu' \leftrightarrow \mu\nu$) only 8 of them are independent. Additionally, if beams are unpolarised two more vanish.

It is convenient to use the helicity basis and express the cross-section for the reaction $e^+e^- \to e^+e^- X$ in terms of cross-sections for interactions of photons with given helicities. The differential cross-section for this process can be then written as:

$$\begin{aligned} d\sigma(e^+e^- \to e^+e^- X) = {} & \frac{d^3p_1' d^3p_2'}{E_1' E_2'} \frac{\alpha^2}{16\pi^4 q_1^2 q_2^2} \left[\frac{(q_1q_2)^2 - q_1^2 q_2^2}{(p_1p_2)^2 - m_e^2 m_e^2}\right]^{1/2} \times \\ & \times [4\rho_1^{++}\rho_2^{++}\sigma_{\mathrm{TT}} + 2|\rho_1^{+-}\rho_2^{+-}|\tau_{\mathrm{TT}} \cos 2\tilde{\Phi} + 2\rho_1^{++}\rho_2^{00}\sigma_{\mathrm{TL}} + 2\rho_1^{00}\rho_2^{++}\sigma_{\mathrm{LT}} \\ & + \rho_1^{00}\rho_2^{00}\sigma_{\mathrm{LL}} - 8|\rho_1^{+0}\rho_2^{+0}|\tau_{\mathrm{TL}} \cos\Phi^*] \end{aligned} \tag{2.9}$$

Here Φ^* is the angle between the scattering planes of the colliding particles in the photon-photon centre-of-mass system.

The quantities σ_{TT}, σ_{TL}, σ_{LT} and σ_{LL} are the cross-sections for interactions between transverse photons (T) with helicities ± 1 or longitudinal photons (L) with helicity 0. Symmetry between both photons requires $\sigma_{\mathrm{TL}}(W_{\gamma\gamma}, q_1^2, q_2^2) = \sigma_{\mathrm{LT}}(W_{\gamma\gamma}, q_2^2, q_1^2)$.

The quantities τ_{TL} and τ_{TT} are the interference terms. If they are independent of Φ^*, the terms containing $\cos 2\Phi^*$ and $\cos\Phi^*$ vanish after integration over Φ^*. For a discussion of a general case see [8].

In the helicity basis the tensor describing production of the final state X, can be written as:

$$\mathcal{W}_{a'b'ab} = \frac{1}{2}\int M^*_{a'b'} M_{ab}(2\pi)^4\delta(q_1+q_2-k)d\Gamma_X \tag{2.10}$$

where indices a, b represent helicities of the interacting photons and M_{ab} are the helicity amplitudes. Expressing functions $\sigma_{\alpha\beta}$ and $\tau_{\alpha\beta}$ in terms of this tensor one gets for example:

$$\begin{aligned} \sigma_{\mathrm{TT}} &= \frac{1}{4\sqrt{A}}(\mathcal{W}_{++,++} + \mathcal{W}_{+-,+-}) \\ \tau_{\mathrm{TT}} &= \frac{1}{2\sqrt{A}}\mathcal{W}_{++,--} \end{aligned} \tag{2.11}$$

where $A = (q_1q_2)^2 - q_1^2q_2^2 = \frac{1}{4}[W_{\gamma\gamma}^4 - 2W_{\gamma\gamma}^2(q_1^2+q_2^2) + (q_1^2-q_2^2)^2]$.
The 3×3 matrices ρ_i^{ab} are now density matrices of virtual photons in the $\gamma\gamma$ helicity basis. It is worth to stress here that the matrix elements ρ_i^{ab} depends on the four-momenta of both photons.
The real photons can only have transverse polarisation, so the terms with at least one longitudinal photon have to vanish as $q_i^2 \to 0$ and have the following functional form: $\sigma_{\mathrm{LT}} \propto q_1^2$, $\sigma_{\mathrm{TL}} \propto q_2^2$, $\sigma_{\mathrm{LL}} \propto q_1^2q_2^2$ and $\tau_{\mathrm{TL}} \propto \sqrt{q_1^2q_2^2}$.

2.3.1 Approximate formulas

In the limit $q_i^2 \to 0$, the only surviving terms in the differential cross-section (equation 2.9) are:

$$\sigma_{\mathrm{TT}}(W_{\gamma\gamma}, q_1^2, q_2^2) \to \sigma_{\gamma\gamma}(W_{\gamma\gamma})$$

$$\tau_{\mathrm{TT}}(W_{\gamma\gamma}, q_1^2, q_2^2) \to \tau_{\gamma\gamma}(W_{\gamma\gamma})$$

where $\sigma_{\gamma\gamma}$ and $\tau_{\gamma\gamma}$ concern real photons interactions and depend only on $W_{\gamma\gamma}$. The $e^+e^- \to e^+e^-X$ cross-section can now be written in the form:

$$\begin{aligned} d\sigma(e^+e^- \to e^+e^-X) = {} & \left(\frac{\alpha}{4\pi^2}\right)^2 \frac{W_{\gamma\gamma}^2}{4E_b^2q_1^2q_2^2} \times \\ & \times \left[4\rho_1^{++}\rho_2^{++}\sigma_{\gamma\gamma} + 2|\rho_1^{+-}\rho_2^{+-}|\tau_{\gamma\gamma}\cos 2\Phi^*\right] \frac{d^3p_1' d^3p_2'}{E_1'E_2'} \end{aligned} \tag{2.12}$$

with density matrix elements [2]:

$$\rho_1^{++} = \frac{(2p_1q_2 - q_1q_2)^2}{2A} + \frac{1}{2} + 2\frac{4m_e^2}{q_1^2}$$

$$\rho_2^{++} = \frac{(2p_2q_1 - q_1q_2)^2}{2A} + \frac{1}{2} + 2\frac{4m_e^2}{q_2^2}$$

$$|\rho_i^{+-}| = \rho_i^{++} - 1$$

For $|q_i^2| \ll W_{\gamma\gamma}^2$ some kinematical relations have simplified form:

$$\Phi^* = \Phi \qquad W_{\gamma\gamma}^2 = 4E_{\gamma1}E_{\gamma2} = 2\sqrt{A}$$

$$-q_i^2 = \frac{q_{i\perp}^2}{1-\frac{E_{\gamma i}}{E_b}} + Q^2_{i\ min}$$

$$\rho_i^{++} = \frac{2E_b(E_b - E_{\gamma i})}{E_{\gamma i}^2}\left(1 - \left|\frac{Q^2_{i\ min}}{q_i^2}\right|\right) + 1$$

where the minimum photon virtuality $Q^2_{i\ min}$ is defined by equation 2.3.
If one now expresses the phase space volume element of the scattered particles by quantities connected to photons and colliding electrons and positrons [2]:

$$\frac{d^3p_1^{'}d^3p_2^{'}}{E_1^{'}E_2^{'}} = \frac{4\pi E_b^2}{2[(p_1p_2)^2 - m_e^2m_e^2]}d(-q_1^2)d(-q_2^2)dE_{\gamma 1}dE_{\gamma 2}d\Phi \tag{2.13}$$

the cross-section can be written as:

$$d\sigma = \left(\frac{\alpha}{2\pi}\right)^2 \frac{E_{\gamma 1}E_{\gamma 2}}{E_b^4 q_1^2 q_2^2}\left[\rho_1^{++}\rho_2^{++}\sigma_{\gamma\gamma} + \frac{1}{2}|\rho_1^{+-}\rho_2^{+-}|\tau_{\gamma\gamma}\cos 2\Phi\right] d(-q_1^2)d(-q_2^2)dE_{\gamma 1}dE_{\gamma 2}d\Phi/2\pi \tag{2.14}$$

Using the following definitions:

$$\begin{aligned} dn_i \ &\equiv \frac{\alpha}{2\pi}\rho_i^{++}\frac{E_{\gamma i}dE_{\gamma i}d(-q_i^2)}{E_b^2|q_i^2|} \\ &= \frac{\alpha}{\pi}\frac{dE_{\gamma i}}{E_{\gamma i}}\frac{d(-q_i^2)}{|q_i^2|}\left[\left(1 - \frac{E_{\gamma i}}{E_b} + \frac{E_{\gamma i}^2}{2E_b^2}\right) - \left(1 - \frac{E_{\gamma i}}{E_b}\right)\left|\frac{Q^2_{i\ min}}{q_i^2}\right|\right] \end{aligned} \tag{2.15}$$

and

$$\xi_i \equiv \frac{|\rho^{+-}|}{\rho_i^{++}} = \frac{\rho_i^{++} - 1}{\rho_i^{++}} \tag{2.16}$$

one can rewrite the cross-section in a simple form:

$$d\sigma = (\sigma_{\gamma\gamma} + \frac{1}{2}\xi_1\xi_2\tau_{\gamma\gamma}\cos 2\Phi)dn_1dn_2d\Phi/2\pi \tag{2.17}$$

The expressions 2.15 and 2.17 describe in fact the Equivalent Photon Approximation (EPA) where dn_i represents the number of equivalent photons. The quantities ξ_i are the photons polarisations.
For $Q_i^2 = 0$, the term containing $\tau_{\gamma\gamma}$ disappears because the angle Φ is undefined [8] and after integration of the formula over Φ one obtains:

$$d\sigma = \sigma_{\gamma\gamma}dn_1dn_2$$

After integration over q_i^2 in the region $Q^2_{i\ min} \leq -q_i^2 \leq Q^2_{i\ max}$ the photon spectra take the form:

$$\begin{aligned} dn_i \ &= \frac{\alpha}{\pi}\frac{dE_{\gamma i}}{E_{\gamma i}}\left[\left(1 - \frac{E_{\gamma i}}{E_b} + \frac{E_{\gamma i}^2}{2E_b^2}\right)\ln\frac{Q^2_{i\ min}}{Q^2_{i\ max}} - \left(1 - \frac{E_{\gamma i}}{E_b}\right)\left(1 - \frac{Q^2_{i\ min}}{Q^2_{i\ max}}\right)\right] \\ &= N(E_{\gamma i})\frac{dE_{\gamma i}}{E_{\gamma i}} \end{aligned} \tag{2.18}$$

The upper integration limit $Q^2_{i\ max}$ is determined by the experimental cut on the angle of the scattered electron $\theta_{i\ max}$ or by an effective cut-off Λ_γ [2], which for hadron production is of the order of the mass of the ρ meson: $Q^2_{i\ max} = E_bE_i^{'}\theta^2_{i\ max}$ or $Q^2_{i\ max} = m_\rho^2$. If $E_bE_i^{'}\theta^2_{i\ max} < \Lambda_\gamma^2$, then $Q^2_{i\ max} = \Lambda_\gamma^2$. The $Q^2_{i\ min}$ is given by the equation 2.3.

2.3.2 Luminosity function

At this point, it is customary to introduce the luminosity function $\mathcal{L}_{\gamma\gamma}$:

$$d\sigma(e^+e^- \to e^+e^-X) = dW_{\gamma\gamma}\frac{d\mathcal{L}_{\gamma\gamma}}{dW_{\gamma\gamma}}\sigma(\gamma\gamma \to X) \tag{2.19}$$

Under the conditions $q_i^2 \to 0$ and $|q_i^2| \ll W_{\gamma\gamma}^2$ i.e. in Equivalent Photon Approximation, the luminosity function can be written as a product of two photon fluxes where each flux is determined by the kinematics of one vertex only:

$$\frac{d\mathcal{L}_{\gamma\gamma}}{dW_{\gamma\gamma}} = \frac{1}{4}\frac{dN(E_{\gamma 1})}{E_{\gamma 1}}\frac{dN(E_{\gamma 2})}{E_{\gamma 2}} \tag{2.20}$$

From the experimental point of view, a useful form of the luminosity function is given by [2, 12]:

$$\frac{d\mathcal{L}_{\gamma\gamma}}{dW_{\gamma\gamma}} = \frac{2\alpha^2}{W_{\gamma\gamma}\pi^2}\left[f(z)\ln\left(\frac{Q_{max}^2}{m_e^2z^2}-1\right)^2 - \frac{1}{3}\left(\ln\frac{1}{z^2}\right)^3\right] \tag{2.21}$$

where $z = \frac{W_{\gamma\gamma}}{2E_{beam}}$ and

$$f(z) = \left(1+\frac{1}{2}z^2\right)^2\ln\frac{1}{z^2} - \frac{1}{2}\left(1-z^2\right)\left(3+z^2\right) \tag{2.22}$$

Dimensionless quantity $\mathcal{L}_{\gamma\gamma}$ does not have the property of a luminosity. To obtain the conventional relation between counting rate and the cross-section, one needs to multiply the luminosity function, $\mathcal{L}_{\gamma\gamma}$, by standard e^+e^- luminosity $\mathcal{L}$ (see section 3.1.1).

2.4 Lepton pair production

Two-photon lepton pair production (Fig.2.2) is a process which can be accurately calculated in perturbative QED. Lepton universality implies the identical form of the $\gamma\gamma \to l^+l^-$ cross-section regardless of lepton type. For real photons the cross-section is:

$$\frac{d\sigma(\gamma\gamma \to l^+l^-)}{d\Omega^*} = \frac{\alpha^2}{W_{\gamma\gamma}^2}\beta^*\frac{2\beta^{*2}\sin^2\theta^* - \beta^{*4}\sin^4\theta^* + 1 - \beta^{*4}}{(1-\beta^{*2}\cos^2\theta^*)^2} \tag{2.23}$$

where

$$\beta^* = \sqrt{1-\frac{4m_l^2}{W_{\gamma\gamma}^2}} = \sqrt{1-\frac{m_l^2}{E_l^{*2}}} \tag{2.24}$$

is the lepton velocity in the two-photon centre-of-mass system, m_l is the mass of the lepton and $d\Omega^* = d\phi^* d\cos\theta^*$. Quantities θ^* and ϕ^* are the polar and azimuthal angle, respectively, and E_l^* is the energy of the lepton in the $\gamma\gamma$ centre-of-mass system.

Integrating equation 2.23 over whole θ^* and ϕ^* range one obtains the following total cross-section for two-photon production of lepton pairs:

$$\sigma(\gamma\gamma \to l^+l^-) = \frac{2\pi\alpha^2}{W_{\gamma\gamma}^2}\left[2\beta^{*3} - 4\beta^* + (3-\beta^{*4})\ln\frac{1+\beta^*}{1-\beta^*}\right] \tag{2.25}$$

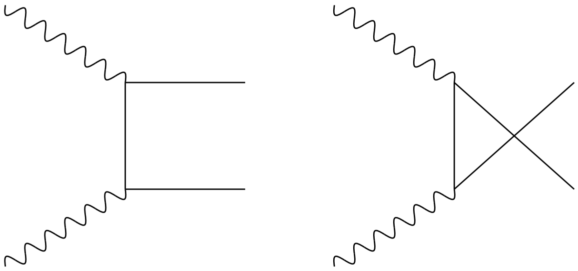

Figure 2.2: Diagrams for lepton pair production in two-photon interactions.

2.5 Resonance production

If the two photons couple to a resonance R [7, 13, 14], which then decays into the two stable particles (final state X), the helicity amplitudes M_{ab} can be factorised:

$$M_{ab} = \delta^{J_z}_{a-b}\delta^{J_X}_{J} \quad \cdot \quad N_{ab}(\gamma\gamma \to R) \quad \cdot \quad \frac{1}{W^2_{\gamma\gamma} - M^2_R + iM_R\Gamma_{tot}} \quad \cdot \quad D_{J_z}(R \to X) \tag{2.26}$$

as shown in Fig.2.3. The first term describes angular momentum conservation, N_{ab} is the

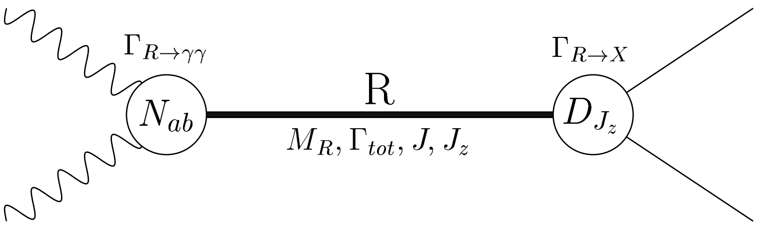

Figure 2.3: Factorisation of the helicity amplitudes in the resonance production.

resonance formation amplitude, the third term is the resonance propagator and D_{J_z} is the resonance decay amplitude. Mass, total width and spin of the resonance are denoted by M_R, Γ_{tot} and J respectively. The quantity J_z is a spin-projection along an arbitrarily defined z-axis. J_X is the total angular momentum of the final state.
The hadronic tensor (2.10) can now be written as:

$$\begin{aligned} \mathcal{W}_{ab,ab} &= \frac{1}{2}\int \left| \frac{N^{J_z=a-b}_{ab} D_{J_z}}{W^2_{\gamma\gamma} - M^2_R + iM_R\Gamma_R} \right|^2 d\Gamma_X \\ &= \frac{1}{2}|N_{ab}|^2 \frac{1}{(W^2_{\gamma\gamma} - M^2_R)^2 + M^2_R\Gamma^2_{tot}} \int |D_{J_z}|^2 d\Gamma_X \end{aligned} \tag{2.27}$$

As the formation of a single resonance by the collision of two real photons is the inverse process to a radiative decay, the relation between the amplitude N_{ab} and the radiative width, $\Gamma_{\gamma\gamma}$, can be written as:

$$\Gamma_{\gamma\gamma} = \frac{1}{32\pi(2J+1)M_R} \sum_{a,b=+-} |N_{ab}|^2 \tag{2.28}$$

The total width is defined as the average of the widths of the particular polarisation states $\Gamma_{\gamma\gamma}^{J_z}$ of the decaying meson

$$\Gamma_{\gamma\gamma} = \frac{1}{(2J+1)} \sum_{J_z} \Gamma_{\gamma\gamma}^{J_z} \tag{2.29}$$

where partial widths are defined in Table 2.1.

J_z	$\Gamma_{\gamma\gamma}^{J_z}$
-2	$\frac{1}{32\pi M_R}\vert N_{-+}\vert^2$
-1	0
0	$\frac{1}{32\pi M_R}(\vert N_{++}\vert^2 + \vert N_{--}\vert^2)$
1	0
2	$\frac{1}{32\pi M_R}\vert N_{+-}\vert^2$

Table 2.1: Partial widths $\Gamma_{\gamma\gamma}^{J_z}$ for resonance R with spin J=2 or higher.

As for helicity matrix elements N_{ab} the following relations follows from symmetry principles:

$$|N_{ab}| = |N_{-a-b}|$$

$$|N_{ab}| = |N_{ba}|$$

one can write

$$\Gamma_{\gamma\gamma} = \frac{1}{16\pi(2J+1)M_R}(|N_{++}|^2 + |N_{+-}|^2) \tag{2.30}$$

Similarly to $\Gamma_{\gamma\gamma}$, the partial width $\Gamma_{(R\to X)}$ is related to decay amplitude:

$$\Gamma_{(R\to X)} = \Gamma_{tot} \cdot Br(R \to X) = \frac{1}{2M_R}\int |D_{J_z}|^2 d\Gamma_X \tag{2.31}$$

where $Br(R \to X)$ is the branching ratio into final state X.
Combining equations 2.11, 2.27, 2.30 and 2.31 one obtains the formula for the cross-section for production of the resonance with spin J, decaying into two stable particles in two quasi-real photon interaction:

$$\sigma_{\mathrm{TT}} = \sigma_{\gamma\gamma} = 8\pi(2J+1)\left(\frac{M_R}{W_{\gamma\gamma}}\right)^2 \frac{\Gamma_{\gamma\gamma}\Gamma_{tot}Br(R\to X)}{(W_{\gamma\gamma}^2 - M_R^2)^2 + M_R^2\Gamma_{tot}^2} \tag{2.32}$$

In case of a resonance with spin J decaying into two spinless particles x^+x^-, the angular dependence is contained in the spherical harmonics $Y_J^\lambda(\theta^*, \phi^*)$, where λ is the helicity of the initial two-photon state and the differential cross-section, $d\sigma^\lambda/d\Omega^*$, is given by:

$$\frac{d\sigma^\lambda(\gamma\gamma \to R \to x^+x^-)}{d\Omega^*} = 8\pi(2J+1)\left(\frac{M_R}{W_{\gamma\gamma}}\right)^2 \frac{\Gamma_{\gamma\gamma}\Gamma_{tot}Br(R\to x^+x^-)}{(W_{\gamma\gamma}^2 - M_R^2)^2 + M_R^2\Gamma_{tot}^2}|Y_J^\lambda(\theta^*, \phi^*)|^2 \tag{2.33}$$

The functions $Y_J^\lambda(\theta^*, \phi^*)$ are normalised so that the integrals over Ω^* of the square of their absolute value are equal to one. For J=2, the functional forms of the spherical harmonics are:

$$\begin{aligned}
\lambda = 0: \quad Y_2^0 &= \sqrt{\frac{5}{4\pi}}\left(\frac{3}{2}\cos^2\theta^* - \frac{1}{2}\right) \\
\lambda = 1: \quad Y_2^1 &= -\sqrt{\frac{15}{8\pi}} e^{i\phi^*} \sin\theta^* \cos\theta^* \\
\lambda = 2: \quad Y_2^2 &= \frac{1}{4}\sqrt{\frac{15}{2\pi}} e^{2i\phi^*} \sin^2\theta^*
\end{aligned} \tag{2.34}$$

For wide resonances, the full width Γ_{tot} depends on $W_{\gamma\gamma}$ because the change of the phase-space in equation 2.31 cannot be neglected. Additionally, some dynamical effects (existence of a potential barrier due to the spin) are responsible for dependency of Γ_{tot} on $W_{\gamma\gamma}$. For the resonance decaying into two stable particles, with momentum p in the resonance centre-of-mass system and spatial orbital angular momentum L of the final state, one thus obtains:

$$\Gamma_{tot}(W_{\gamma\gamma}) = \Gamma^0_{tot}\left(\frac{p}{p_0}\right)^{2\mathrm{L}+1} \frac{M_R}{W_{\gamma\gamma}} \frac{f^2(pr)}{f^2(p_0 r)} \tag{2.35}$$

where

$$p(s) = \sqrt{\frac{1}{4}s - m^2}$$

and $p_0 \equiv p(M_R^2)$, $p \equiv p(W_{\gamma\gamma}^2)$. M_R and Γ^0_{tot} are the nominal mass and width of the resonance and m is the mass of the final state particle. The hadronic form factor f^2 is necessary to introduce a damping at high energies. In the widely used Blatt-Weisskopf model where interaction potential is constant within a sphere of radius r, the form factors depend on orbital angular momentum of the final state L. For example, for L=2 the $f^2(pr)$ is given by:

$$f^2(\mathrm{L}=2) \propto \frac{r^4}{(pr)^4 + 3(pr)^2 + 9} \tag{2.36}$$

The effective interaction radius r is constrained from hadronic scattering data and usually taken as $r \simeq 1$ fm. At the nominal resonance mass M_R, the form factors are equal to unity.
Using the Blatt-Weisskopf form-factor, the total width of a tensor resonance decaying into two spinless particles is finally given by:

$$\Gamma_{tot}(W_{\gamma\gamma}) = \Gamma^0_{tot}\left(\frac{p}{p_0}\right)^5 \frac{M_R}{W_{\gamma\gamma}} \frac{(p_0 r)^4 + 3(p_0 r)^2 + 9}{(pr)^4 + 3(pr)^2 + 9} \tag{2.37}$$

The different theoretical approaches lead to the conclusion that the tensor meson production by two real photons proceeds predominantly via a $\gamma\gamma$ helicity $\lambda = 2$. In the simplest way, the relative frequency of occurrence of possible helicity states can be estimated from Clebsch-Gordan coefficients. Assuming that the spins of the two photons are parallel and that there is no orbital angular momentum, one finds the ratio:

$$\sigma_{\lambda=0} : \sigma_{\lambda=2} : \sigma_{\lambda=-2} = \frac{1}{3} : 1 : 1$$

If one takes the absolute value of the helicity, the ratio is 6:1 in favour of helicity 2.

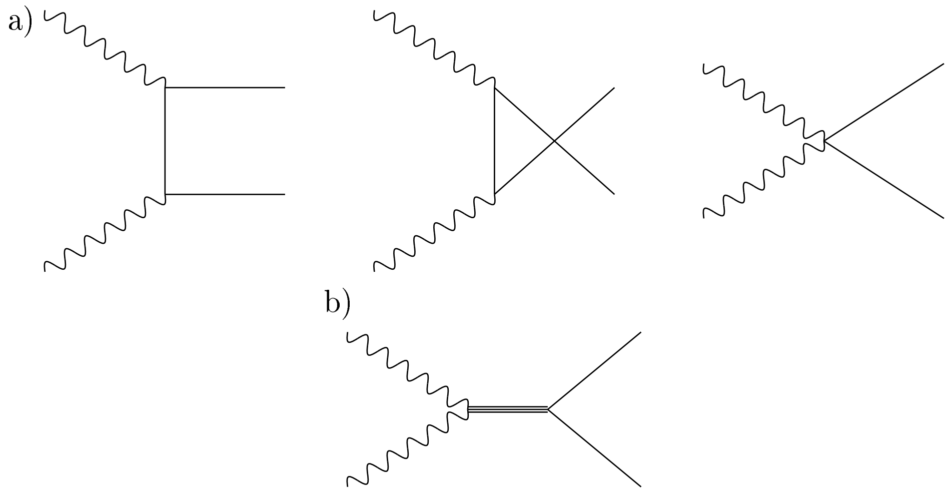

Figure 2.4: a) Born diagrams for two-photon production of two charged, scalar particles. b) Resonance contribution.

2.6 Born approximation for production of point-like pions and kaons

At low energies, the two-photon production of pion pairs can be described as QED coupling of the photons to point-like pions. Since pions are scalar particles, in comparison to lepton pair production, the third diagram has to be included in the matrix element. These QED lowest order diagrams are shown in Fig.2.4 The cross-section can be divided into two parts: one for total $\gamma\gamma$ helicity 0 (both photons with the same helicity) and the second for helicity 2 (photons with opposite helicities). The differential cross-sections for pion production by two real photons are:

$$\begin{aligned}
\text{total}: \quad & \frac{d\sigma(\gamma\gamma \to \pi^+\pi^-)}{d\Omega^*} = \frac{\alpha^2}{2W_{\gamma\gamma}^2}\beta^*\frac{(1-\beta^{*2})^2+\beta^{*4}(1-\cos^2\theta^*)^2}{(1-\beta^{*2}\cos^2\theta^*)^2} \\
\lambda = 0: \quad & \frac{d\sigma(\gamma\gamma \to \pi^+\pi^-)}{d\Omega^*} = \frac{\alpha^2}{2W_{\gamma\gamma}^2}\beta^*\frac{(1-\beta^{*2})^2}{(1-\beta^{*2}\cos^2\theta^*)^2} \\
\lambda = 2: \quad & \frac{d\sigma(\gamma\gamma \to \pi^+\pi^-)}{d\Omega^*} = \frac{\alpha^2}{2W_{\gamma\gamma}^2}\beta^*\frac{\beta^{*4}(1-\cos^2\theta^*)^2}{(1-\beta^{*2}\cos^2\theta^*)^2}
\end{aligned} \tag{2.38}$$

where β^* is the velocity of the meson in the $\gamma\gamma$ centre-of-mass system. After integration over the whole range of $\cos\theta^*$ the cross sections are:

$$\begin{aligned}
\sigma(\text{total}) &= \frac{\pi\alpha^2}{W_{\gamma\gamma}^2}\beta^*\left[2\beta^*(2-\beta^{*2})-(1-\beta^{*4})\ln\frac{1+\beta^*}{1-\beta^*}\right] \\
\sigma(\lambda=0) &= \frac{\pi\alpha^2}{W_{\gamma\gamma}^2}\left[\beta^*(1-\beta^{*2})+\frac{1}{2}(1-\beta^{*2})^2\ln\frac{1+\beta^*}{1-\beta^*}\right] \\
\sigma(\lambda=2) &= \frac{\pi\alpha^2}{W_{\gamma\gamma}^2}\left[\beta^*(3-\beta^{*2})+(\beta^{*4}+2\beta^{*2}-3)\ln\frac{1+\beta^*}{1-\beta^*}\right]
\end{aligned} \tag{2.39}$$

This approximation should be valid in the region where final-state interactions are negligible and where the wavelength of the photon is large compared to the size of the

pion. It has been shown experimentally [15, 16] that the approximation is reasonable up to the mass of $f_2(1270)$.
In case of charged kaon pair production, the rich resonance structure and small statistics of available data [17] do not allow for the statement that the Born approximation is a good description of that process.

2.7 Interference between resonance and continuum

The Born cross-section for $\gamma\gamma \to \pi^+\pi^-$, in the region of $f_2(1270)$ resonance is dominated by the helicity-2 contribution (Fig.2.5). Since f_2 is also predicted to be dominantly produced in a $\lambda = 2$ state (see section 2.5), the strong interference between the resonance and the continuum can be expected:

$$\begin{aligned}\frac{d\sigma}{d\Omega^*} &= |F_B^{\lambda=0}|^2 + |F_B^{\lambda=2} + F_R|^2 \\ &= |F_B^{\lambda=0}|^2 + |F_B^{\lambda=2}|^2 + |F_R|^2 + 2|F_B^{\lambda=2}||F_R|\cos(\delta+\zeta)\end{aligned} \tag{2.40}$$

$F_B^{\lambda=0}$, $F_B^{\lambda=2}$ and F_R represent two parts of the Born amplitude with different helicities and the resonance amplitude, respectively. δ is the intrinsic phase difference between the resonance and the Born amplitude. The additional phase, ζ, between the $F_B^{\lambda=2}$ and F_R amplitudes, is an unknown parameter of the model and is determined experimentally. From the fit to the data [15] it was found that the phase ζ is consistent with π.
Phase factors $\exp(2i\phi^*)$ are present in both Born and resonance amplitude, so the whole interference effect comes from the term:

$$F_R' \sim \frac{1}{W_{\gamma\gamma}^2 - M_R^2 - iM_R\Gamma_{tot}}$$

which is the part of resonance amplitude. The phase angle δ is therefore given by:

$$\cos\delta = \frac{Re(F_R')}{|F_R'|}$$

and one can rewrite equation 2.40 in a modified form:

$$\frac{d\sigma}{d\Omega^*} = |F_B^{\lambda=0}|^2 + |F_B^{\lambda=2}|^2 + |F_R|^2 - 2Re(F_R')|F_B^{\lambda=2}| \tag{2.41}$$

and the interference term is:

$$\begin{aligned}\left(\frac{d\sigma}{d\Omega^*}\right)_{int} &= 2\sqrt{\frac{40\pi\Gamma_{\gamma\gamma}\Gamma_{tot}Br(f_2\to\pi^+\pi^-)M_R^2}{W_{\gamma\gamma}^2}} \times \\ &\times \frac{W_{\gamma\gamma}^2 - M_R^2}{(W_{\gamma\gamma}^2 - M_R^2)^2 + M_R^2\Gamma_{tot}^2}|Y_2^2(\theta^*,\phi^*)| \times \\ &\times \sqrt{\frac{\alpha^2\beta^*}{2W_{\gamma\gamma}^2}\frac{\beta^{*2}(1-\cos^2\theta^*)}{1-\beta^{*2}\cos^2\theta^*}}\end{aligned} \tag{2.42}$$

The cross-section for two extreme cases of constructive ($\zeta = \pi$) and destructive ($\zeta = 0$) interference below f_2 mass is shown in Fig.2.5, together with resonance contribution and

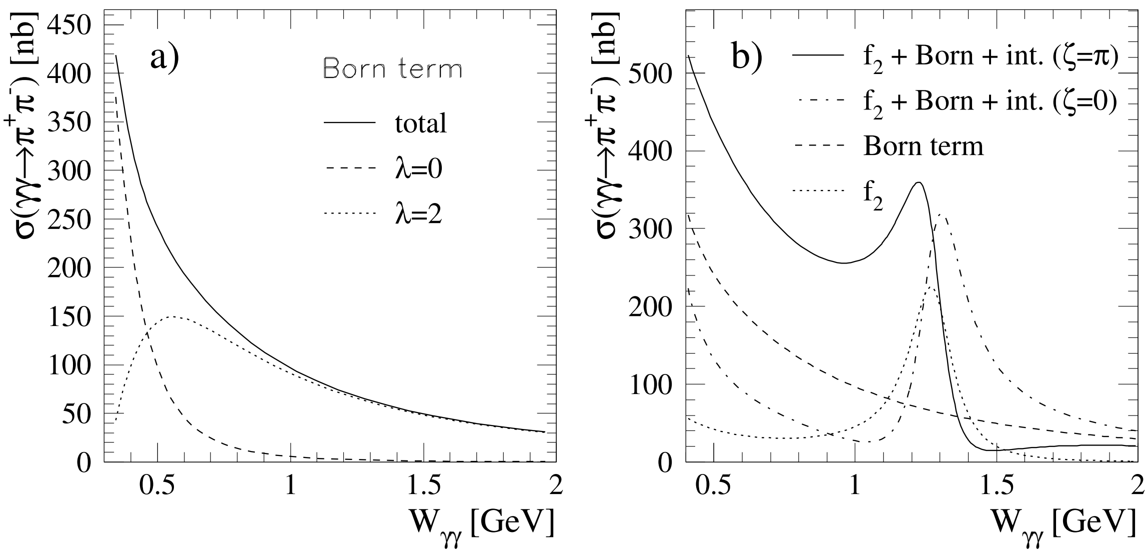

Figure 2.5: a) Cross-section for $\gamma\gamma \to \pi^+\pi^-$ in Born approximation for $\gamma\gamma$ helicities 0, 2 and the superposition of both. b) cross-section for $\gamma\gamma \to \pi^+\pi^-$ as a sum of Born continuum, resonance f_2 and the interference term in two extreme cases: constructive ($\zeta = \pi$, solid curve) and destructive ($\zeta = 0$, dashed-dotted curve) interference below the f_2 mass. The Born term (dashed curve) and resonance (dotted curve) with Γ_{tot}=186 MeV, $\Gamma_{\gamma\gamma}$=2.45 keV and M_R=1275 MeV are also shown separately.

Born contribution alone. It is clear that the interference effects can lead to the substantial shift and distortion of the f_2 peak.

In case of charged kaon pair production the known resonance structure is richer than in charged pion production: apart from the $f_2(1270)$, the production of the tensor resonances $a_2(1320)$ and $f_2^{'}(1525)$ has been observed.
As it was mentioned in the previous section, the available data samples were too small for a complete analysis of interference effects.

2.8 The finite-size model

The attempt to implement the structure of the π and K mesons in the Born approximation, described in section 2.6, was done by Poppe [7]. He started from the same Born diagrams, but took the coupling of the photons to be non point-like. In his approach the original QED amplitude is multiplied by the factor G:

$$M_{ab} = G M_{ab}(QED) \tag{2.43}$$

For real photons he obtained the following expression for this factor:

$$G = \frac{1}{2}\left\{ \frac{1-\beta^* cos\theta^*}{1+\frac{W_{\gamma\gamma}^2(1+\beta^* cos\theta^*)}{2x_0^2}} + \frac{1+\beta^* cos\theta^*}{1+\frac{W_{\gamma\gamma}^2(1-\beta^* cos\theta^*)}{2x_0^2}} \right\} \tag{2.44}$$

where x_0 is a scale parameter set by the pion form factor. Expressed in units of energy, $x_0 \approx m_\rho$.
As the consequence of equation 2.43, the term $(d\sigma/d\Omega^*)_{Born}$ is multiplied by G^2 and the interference term $(d\sigma/d\Omega^*)_{int}$ by G.

2.9 Models based on perturbative QCD

Exclusive two-photon processes such as production of meson pairs play a unique role in testing quantum Chromodynamics because of the simplicity of the initial state.
The detailed leading-order QCD calculations have been done by Brodsky and Lepage [18]. At large centre-of-mass angles, the $\gamma\gamma \to M\overline{M}$ amplitude can be factorised (Figs. 2.6, 2.7) into a hard-scattering amplitude T_H that describes valence parton interactions and into the probability amplitude ϕ_M for finding valence partons in each meson:

$$M^{ab}(W_{\gamma\gamma}, \theta^*) = \int_0^1 dx \int_0^1 dy \phi^*_M(x, \tilde{Q}_x)\phi^*_M(y, \tilde{Q}_y) T^{ab}_H(x, y; W_{\gamma\gamma}, \theta^*) \tag{2.45}$$

Indexes a and b represent photon helicities, x and y are the fractions of meson's momentum carrying by one of the quarks, and $\tilde{Q}_x \sim \min(x, 1-x)W_{\gamma\gamma}|\sin\theta^*|$ (similarly for $\tilde{Q}_y$). This factorisation allows the analytic separation of the perturbatively-calculable short-distance contributions from the long-distance non-perturbative dynamics associated with meson binding. The T_H amplitude has been computed with quarks collinear with the outgoing mesons.

The spin-averaged cross-section for the process $\gamma\gamma \to M\overline{M}$ is given by:

$$\frac{d\sigma}{d\cos\theta^*} = \frac{W^2_{\gamma\gamma}}{2}\left[\frac{d\sigma}{dt}\right] = \frac{1}{32\pi W^4_{\gamma\gamma}}\frac{1}{4}\sum_{ab}|M^{ab}|^2 \tag{2.46}$$

and finally, for helicity-zero mesons:

$$\begin{aligned} \frac{d\sigma}{d\cos\theta^*} = \frac{8\pi\alpha^2}{W^6_{\gamma\gamma}}|W^2_{\gamma\gamma}F_M(W^2_{\gamma\gamma})|^2 \times \\ \times\left\{\frac{1}{(1-\cos^2\theta^*)^2} - \frac{4}{9(1-\cos^2\theta^*)}g(\theta^*, \phi_M) + \frac{8}{81}g^2(\theta^*, \phi_M)\right\} \end{aligned} \tag{2.47}$$

Much of the dependence on ϕ_M has been removed from M_{ab} by expressing it in terms of

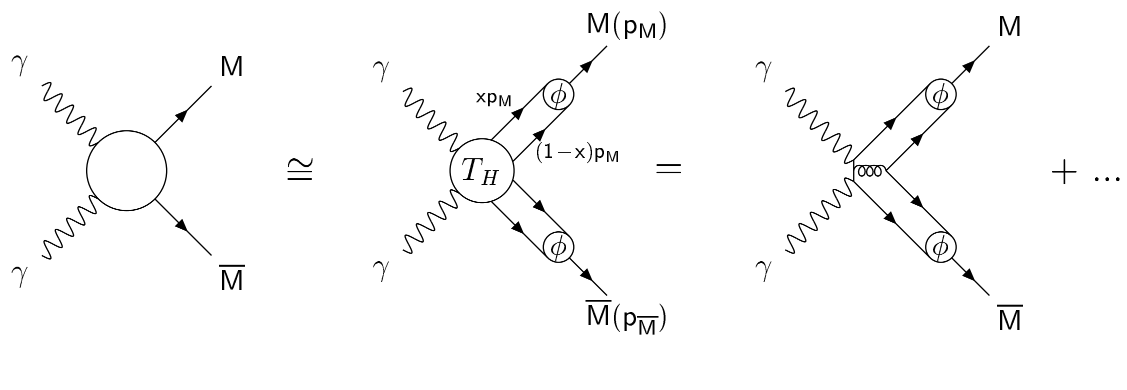

Figure 2.6: Factorised structure of the $\gamma\gamma \to M\overline{M}$ amplitude in QCD at large momentum transfer.

the meson form factor $F_M(W^2_{\gamma\gamma})$ which can be written as:

$$F_M(W^2_{\gamma\gamma}) = \frac{16\pi\alpha_s}{3W^2_{\gamma\gamma}} \int_0^1 dxdy \frac{\phi^*_M(x,\tilde{Q}_x)\phi^*_M(y,\tilde{Q}_y)}{x(1-x)y(1-y)} \tag{2.48}$$

when $\phi_M(x,Q) = \phi_M(1-x,Q)$ is assumed.
The remaining, weak dependence on ϕ_M is in the θ^* dependent factor $g(\theta^*,\phi_M)$:

$$g(\theta^*,\phi_M) = \frac{\int_0^1 dxdy \frac{\phi^*_M(x,\tilde{Q}_x)\phi^*_M(y,\tilde{Q}_y)}{x(1-x)y(1-y)} \frac{a[y(1-y)+x(1-x)]}{a^2-b^2\cos^2\theta^*}}{\int_0^1 dxdy \frac{\phi^*_M(x,\tilde{Q}_x)\phi^*_M(y,\tilde{Q}_y)}{x(1-x)y(1-y)}} \tag{2.49}$$

where $a = (1-x)(1-y) + xy$ and $b = (1-x)(1-y) - xy$.
The distribution amplitude, ϕ_M, specifies the momentum distribution of the quarks in the meson. The functional forms of this amplitude from various models are shown in Table 2.2. The quantity f_M is the meson decay constant. From the decays $\pi^+(K^+) \to \mu^+\nu_\mu + \mu^+\nu_\mu\gamma$ one obtains the following numerical values: $\sqrt{2}f_{\pi^+} = 130.7 \pm 0.1 \pm 0.36$ MeV and $\sqrt{2}f_{K^+} = 159.8 \pm 1.4 \pm 0.44$ MeV [1].

Model	Functional form
Non-relativistic	$\frac{f_M}{2\sqrt{3}}\delta(x-\frac{1}{2})$
Asymptotic QCD	$\lim_{Q^2\to\infty}\phi_M = \sqrt{3}f_M x(1-x)$
QCD sum rule (pion)[20]	$\frac{15f_\pi}{\sqrt{3}}x(1-x)(2x-1)^2$
QCD sum rule (kaon)[20]	$\frac{15f_K}{\sqrt{3}}x(1-x)[0.08+0.6(2x-1)^2+0.25(2x-1)^3]$

Table 2.2: A comparison of the functional forms of the meson distribution amplitudes from various models. Presently it seems that the pion distribution amplitude close to the asymptotic one, describes best the pion form factor data (see for example [21]).

The normalisation of ϕ_M is given by the condition:

$$\int_0^1 dx\phi_M(x,Q) = \frac{f_M}{2\sqrt{3}} \tag{2.50}$$

The meson form factor, $|F_M(W^2_{\gamma\gamma})|$, is proportional to the strong coupling constant α_s and to the meson decay constant f_M squared. Under the assumption that the parton

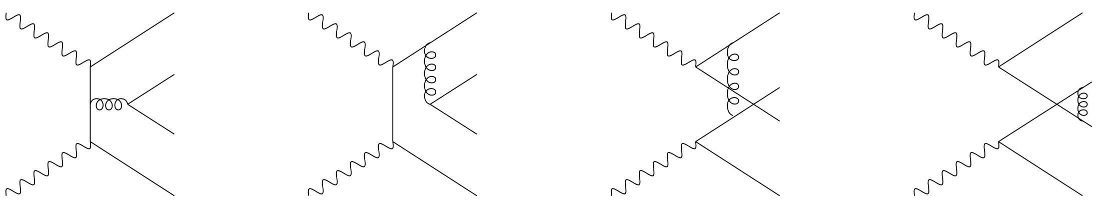

Figure 2.7: Diagrams contributing to T_H to lowest order in α_s

distribution amplitudes for kaon (ϕ_K) and for pion (ϕ_π) are similar in shape, the ratio of the cross-sections for $\gamma\gamma \to K^+K^-$ to $\gamma\gamma \to \pi^+\pi^-$ is completely determined by the ratio of meson decay constants [18]:

$$\frac{\frac{d\sigma}{d\cos\theta^*}(\gamma\gamma \to K^+K^-)}{\frac{d\sigma}{d\cos\theta^*}(\gamma\gamma \to \pi^+\pi^-)} \simeq \frac{|F_K|^2}{|F_\pi|^2} \simeq \left[\frac{f_K}{f_\pi}\right]^4 \simeq 2.2 \qquad (2.51)$$

Brodsky and Lepage have shown that in the case of charged pion production, if they approximate the pion form factor by $|F_\pi(W^2_{\gamma\gamma})| \simeq 0.4\mathrm{GeV}^2/W^2_{\gamma\gamma}$, the cross-section is essentially independent of the choice of the parton distribution amplitude. In the calculations all quark and hadron masses have been neglected.

The first attempt to calculate the next-to-leading order QCD predictions has been performed by Nižić [22]. He has used simplified form of meson distribution amplitude $\phi_M \sim \delta(x - \frac{1}{2})$, assuming that in next-to-leading order the cross-section is also independent of ϕ_M. He has calculated the corrections to the hard-scattering amplitude only, neglecting corresponding order α_s corrections to the meson distribution amplitude and has found that only for $W_{\gamma\gamma} > 10$ GeV the corrections to the lowest-order predictions are small ($< 25\%$).

The insensitivity of the cross-section for $\gamma\gamma \to \pi^+\pi^-$ to the pion distribution amplitude has been discussed by Benayoun and Chernyak [23], who argue that the ϕ_M dependence of the form factor cannot be ignored. Their predictions of the pion form factor based on the QCD sum rule derived ϕ_M, however, are in a good agreement with the approximation $|F_M(W^2_{\gamma\gamma})| \simeq 0.4\mathrm{GeV}^2/W^2_{\gamma\gamma}$ used in [18, 22]. This value of the form factor excludes distribution amplitude of the type $\phi_M \sim \delta(x - \frac{1}{2})$ as used by Nižić.

Finally, following [20], they argue that the SU(3) flavour symmetry breaking effects on ϕ_M are not small and one cannot approximate the ratio of the cross-sections by the ratio of decays constants. The differences between ϕ_K and ϕ_π nearly compensate those generated by f_K and f_π and the kaon and pion form factors are nearly equal [24]. In the first approximation this leads to the result that the ratio of $d\sigma(\gamma\gamma \to K^+K^-)$ and $d\sigma(\gamma\gamma \to \pi^+\pi^-)$ is close to 1. More precise calculation by Benayoun and Chernyak gives:

$$\frac{\frac{d\sigma}{d\cos\theta^*}(\gamma\gamma \to K^+K^-)}{\frac{d\sigma}{d\cos\theta^*}(\gamma\gamma \to \pi^+\pi^-)} \simeq 1.08 \qquad (2.52)$$

Although the authors claim that their prediction can be considered much more reliable for cross-section ratio, they also show results for absolute cross-sections, which does not differ significantly from the calculations by Brodsky and Lepage.

The changes of α_s in the calculation of pion and kaon form factors and the subsequent effect on the leading order result (equation 2.47) have been discussed by Ji and Amiri [25]. Instead of the usual one-loop formula for the running coupling constant:

$$\alpha_s(Q^2) = \frac{4\pi}{\beta\ln(Q^2/\Lambda^2)}$$

where Λ is a QCD scale parameter of order 100 MeV, $\beta = 11 - \frac{2}{3}n_f$ and n_f is the number of flavours, they use:

$$\alpha_s(Q^2) = \frac{4\pi}{\beta\ln[(Q^2 + 4m_g^2)/\Lambda^2]}$$

where m_g is interpreted as an "effective dynamical gluon mass". For $Q^2 \gg m_g^2$ these two formulas coincides one with the other, but for a very-low momentum transfer the

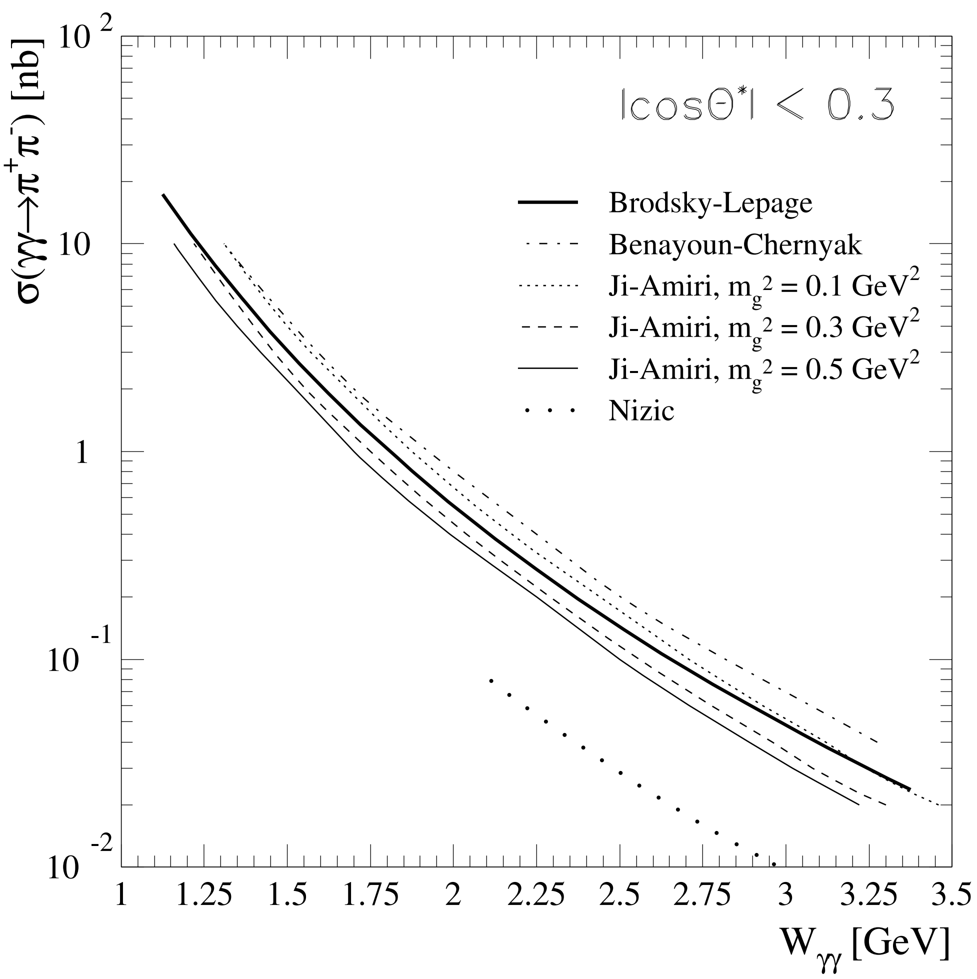

Figure 2.8: QCD-based predictions for the $\gamma\gamma \to \pi^+\pi^-$ cross-section. The angular range is restricted to $|\cos\theta^*| < 0.3$.

last formula "freezes" the coupling constant at some finite value. In the calculations, the QCD sum rule derived meson distribution amplitudes has been used. To investigate the sensitivity of the results to the choice of ϕ_M, they also calculated the pion form factor and the $\gamma\gamma \to \pi^+\pi^-$ cross-section using the quark distribution amplitude obtained by Dziembowski and Mankiewicz [26]. The difference between cross-sections in these two cases is negligible.
The cross-section predictions for two photon production of pion pairs for three different values of α_s (three different values of m_g^2) are shown in Fig.2.8, together with Brodsky and Lepage, Benayoun and Chernyak and Nižić predictions.

2.10 Summary of theoretical considerations

The system X produced in two-photon interactions at the e^+e^- colliders has, in general, boost in the direction of one of the incoming beams, because the photon energies are usually unequal. This leads to the situation where in significant fraction of events the final state mesons are produced close to the beam direction and remain undetected.
A simple estimate of the cross-sections which can be measured by an experiment is given by applying the cut $|\cos\theta^*| < 0.6$ (Fig.2.9). Under this condition, the cross-section for the process $\gamma\gamma \to e^+e^-$ becomes almost equal to the cross-section for $\gamma\gamma \to \mu^+\mu^-$, but both still remain higher than the cross-section for the production of pion pairs, which measurement is one of the main goals of this thesis.
The measurements performed in this thesis will be mainly shown in the angular range restricted just to $|\cos\theta^*| < 0.6$.

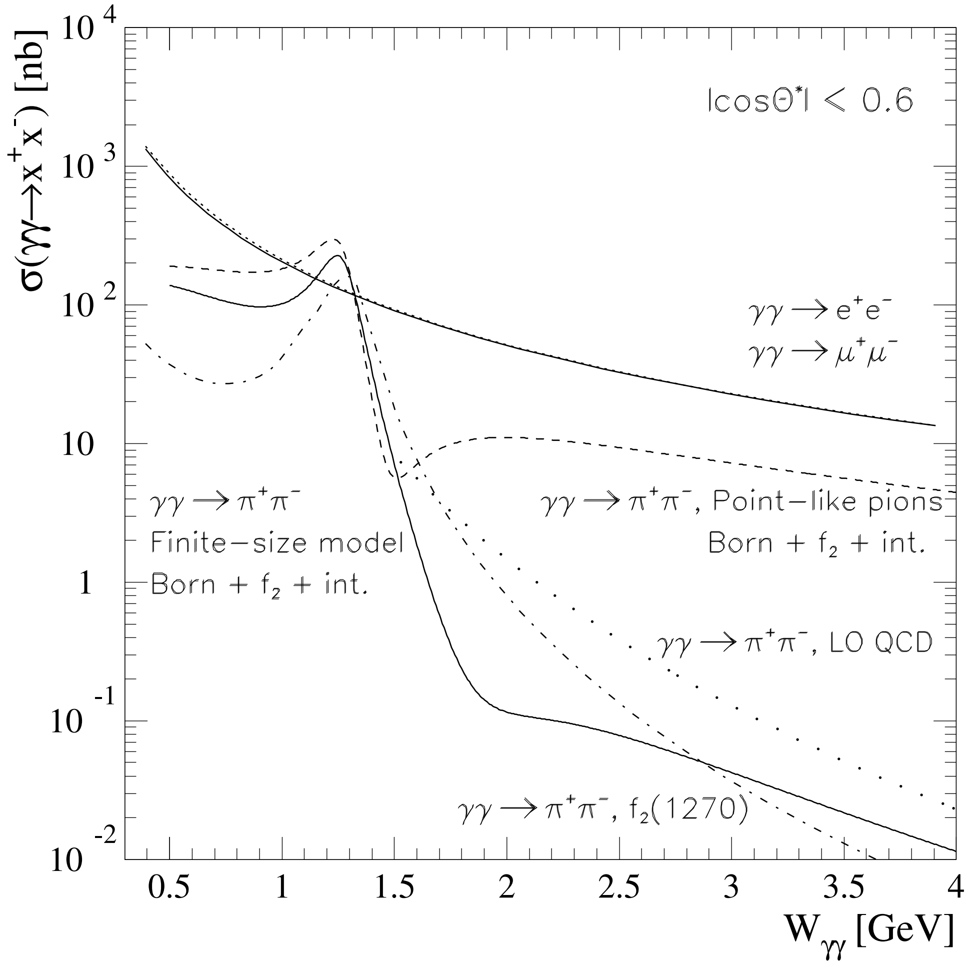

Figure 2.9: Theoretical predictions for two-photon production of: muon pairs (solid curve), electron pairs (dashed curve, just above the solid curve), resonance $f_2(1270)$ (dashed-dotted curve), pion pairs, with interference between the $f_2(1270)$ resonance and continuum included in point-like (dashed curve) and finite-size (solid line) approximation. The dotted curve, above the resonance one, is the leading-order Brodsky and Lepage QCD prediction for the production of charged pion pairs. The angular range is restricted to $|\cos\theta^*| < 0.6$.

Chapter 3

Experimental Setup

3.1 The LEP accelerator

The Large Electron Positron collider (LEP) is located on the French-Swiss border at the European Laboratory for Particle Physics (CERN). The LEP tunnel is 26.7 km in circumference and lies 45 to 175 meters below the surface. The ring consists of eight straight sections and eight arcs. Collision points between electron and positron beams are arranged at the centres of the four straight sections. The particles are accelerated using RF cavities located on the both sides of the interaction points[1]. The cavities are required to accelerate particles from energy of 22 GeV with which they are injected into LEP from the SPS accelerator to the nominal energy. Once the required energy is achieved, LEP operates as a storage ring, and the cavities are used to compensate the energy lost by particles due to synchrotron radiation.
The LEP cycle consists of several phases:

- filling of accelerator with electrons of energy 22 GeV;
- accelerating of the particles;
- optimalisation of the LEP parameters;
- closing of collimators protecting detectors from machine induced background such as synchrotron radiation;
- stable mode - collisions between electrons and positrons.

After a typically 12 hours the beams are dumped and a new cycle begins [27].
The beams are concentrated in bunches which are several centimetres long, and a few millimetres high. There are $\sim 2 \cdot 10^{11}$ particles in each bunch. The amount of bunches was changing in time. The initial $4 \times e^+$ on $4 \times e^-$ bunch configuration was extended to an $8 \times e^+$ on $8 \times e^-$ configuration and in last years, after increasing beam energies the particles can also circulate in four groups (trains) of up to four bunches.
Before each collision, the beams are focussed by superconducting quadrupoles to about 10 μm and 150 μm in the vertical and horizontal planes respectively.

Collisions take place every 11 μs (for eight bunches), in four points on the LEP circumference, where detectors: ALEPH, DELPHI, L3 and OPAL are situated (Fig.3.1).

[1] Only two out of four straight sections were used at the LEP1 phase, when energy of the beams was equal about 45.6 GeV.

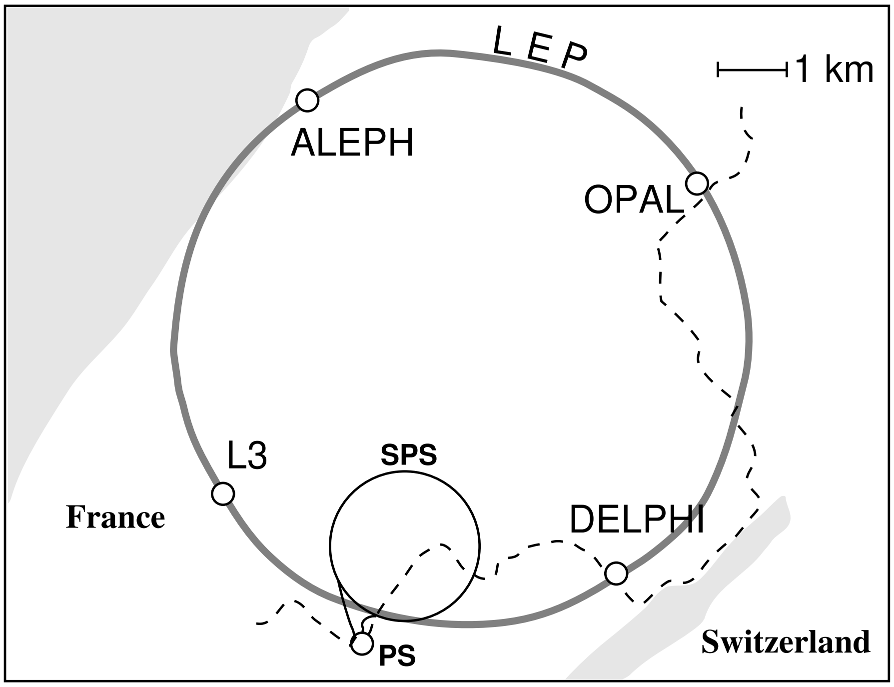

Figure 3.1: LEP accelerator and the four experiments: ALEPH, DELPHI, L3 and OPAL

3.1.1 Performance

The characteristic properties of an accelerator are its effective centre-of-mass energy and luminosity. At LEP the centre-of-mass energy is simply equal to the doubled beam energy. From 1989 to 1995, energy of the beams was around 45.6 GeV, to produce a large quantity of Z^0 bosons. Approximately four million Z^0 hadronic decays were collected by each of the four experiments. In the autumn of 1995, the energy was increased to 65 GeV per beam. The LEP2 phase started in 1996 with the beam energy rising from 81 GeV to 91.3 GeV in 1997. Energies available at the centre-of-mass system in years 1992-1997 are collected in Table 3.1. The second quantity which characterises potential of an accelerator is the luminosity, L, defined by the expression $\frac{dn}{dt} = \sigma \cdot L$, where $\frac{dn}{dt}$ denotes the event rate and σ stands for the cross-section for a given process. For two oppositely directed beams of relativistic particles the formula for L is:

$$L = f \cdot n \cdot \frac{N_{e^-} N_{e^+}}{4\pi\sigma_x\sigma_y}[\mathrm{cm}^{-2}\mathrm{s}^{-1}]$$

where N_{e^-} and N_{e^+} are the numbers of electrons and positrons in each bunch, n is the number of bunches in either beam, f is the revolution frequency, σ_x and σ_y are the dimensions of the bunches in the plane perpendicular to the beam direction. In practise, the integrated luminosity $\mathcal{L} = \int Ldt$ is very often used. Product of the integrated luminosity and the cross-section for the given process tells us how many events from that process can be expected in certain period of time.

Values of the integrated luminosity recorded by the DELPHI experiment in different years are shown in Table 3.1.

Year	1992	1993	1994	1995			1996		1997		
CMS energy $\sqrt{s}$ [GeV]	91	91	91	91	130	136	161	172	183	130	136
Integrated luminosity $\mathcal{L}[pb^{-1}]$	23	36.3	46	32	3	2.9	10	10	53.5	3	3

Table 3.1: The centre-of-mass energies and the integrated luminosities for LEP in years 1992-1997

3.1.2 A system of coordinates

In the standard DELPHI coordinate system the z axis is along the electron beam direction (anti-clockwise), the y axis points upwards and the x axis points towards the centre of LEP. The polar angle to the z axis is called θ, the azimuthal angle around the z axis is called ϕ and the radial coordinate is expressed by formula $r = (x^2 + y^2)^{1/2}$.

3.2 The DELPHI detector

The DELPHI (**De**tector with **L**epton, **P**hoton and **H**adron **I**dentification) detector [28, 29, 30] is one of the four general purpose experiments installed at the LEP accelerator. The design aims for high tracking efficiency and good calorimetry performance over nearly the full solid angle. The special emphasis has been put on the particle identification, in particular identification of charged hadrons, largely based on Cherenkov radiation phenomenon.
As illustrated in Fig.3.2 DELPHI consists of a central cylindrical barrel section and two forward endcaps (only one is shown). The endcaps can be moved to allow access to the subdetectors. An accelerator beam-pipe runs along the cylinder's axis. The detector has an overall length and diameter of over 10 m and is composed of 22 sub-detectors and the superconducting solenoid which provides a highly uniform 1.23 Tesla magnetic field.

On the basis of the role which the sub-detectors play in the particle reconstruction and identification, the sub-detectors can be divided into the three groups:

1. tracking detectors - for charged particles tracks reconstruction;
2. calorimeters - for measurement of particle energy;
3. detectors for particle identification.

3.2.1 Tracking detectors

The trajectory of a charged particle is determined from its ionisation deposits in the tracking detector. The curvature of a particle in the magnetic field is used to determine its charge and momentum.
In DELPHI, the tracking system is segmented into a relatively large number of independent tracking devices. The geometric acceptances of the tracking detectors described below are given in Table 3.2.

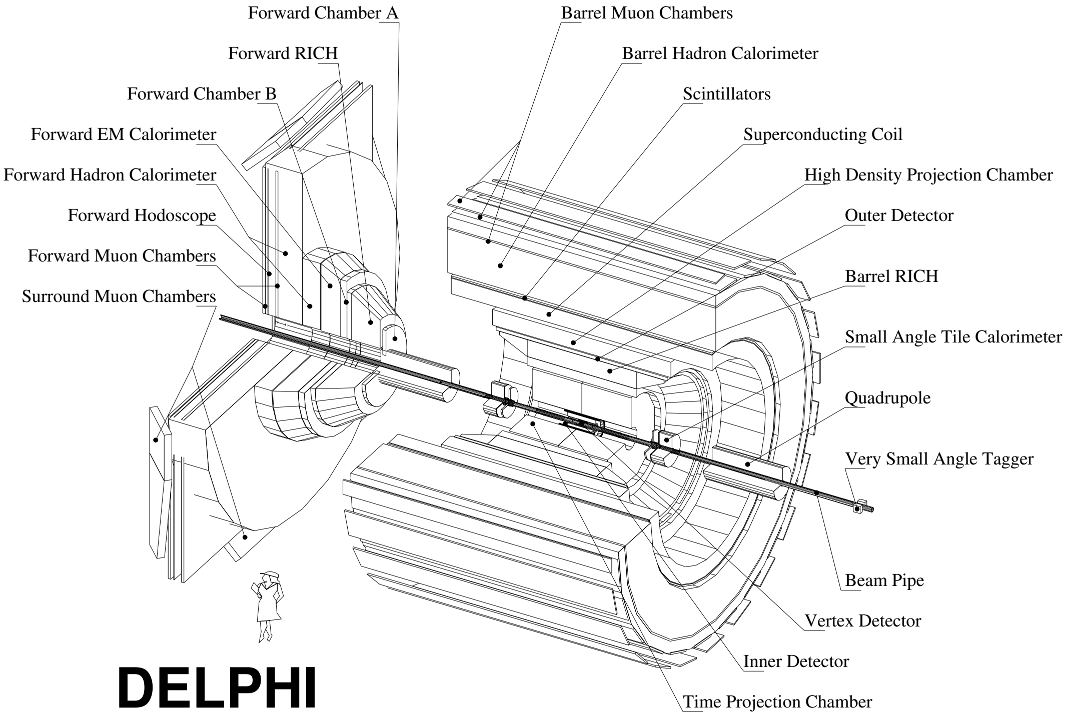

Figure 3.2: Schematic view of the DELPHI detector

- *Time Projection Chamber (TPC)*

The principal tracking detector of DELPHI is a 2 × 1.3 m long drift chamber (Fig.3.3). The TPC provides three dimensional spatial information, measurement of particle ionisation energy loss (dE/dx) and contributes to the trigger decision at all levels.

The two drift volumes of the TPC are separated by a perpendicular to the beam axis, thin high voltage (20 kV) electrode, producing an uniform electric field of 150 V/cm. The electric field, similarly to magnetic field is directed along the z axis. A charged particle passing through the cylinder volume produces by ionisation around 70 electrons per cm of gas. Under the action of electric field these electrons drift towards the end-plates, with a velocity of 6.7cm/μs. The endcaps of the TPC are built of multi-wire proportional chambers, divided into 6 sectors. In each sector, the drifting electron meets three planes of wires.
The first grid, called gate grid is composed of wires at small alternate potential +30 V and -30 V. This potential does not have significant influence on electrons movement, but captures much slower, positive ions (the ions velocity $v_J =$ 0.3 cm/ms) produced at the level of the sensitive wires. The second, cathod grid limits the electric field of the proportional chamber. The last grid is made of 192 anode sense wires at high voltage of 1430 V, separated by wires which form the field shielding the sense wires.
The charge avalanches near the sense wires induce pulses on the cathode pads. There are 1680 pads in each sector, organised in 16 concentric circles (Fig.3.4).

Detector name	Geometric acceptance		
	r [cm]	$\mid z \mid$ [cm]	θ [°]
Time Projection Chamber	29-122	$\leq$ 134	20-160
Silicon tracker in 1997 :			
Vertex Detector	6.6, 9.2, 10.6	$\leq$ 24	21-159
VFT - pixel detector	6.9-11.2		12-26
VFT - strip detector	6.8-11.2		10-18
Inner Detector:			
Inner part before 1995 r.	11.8-22.3	$\leq$ 40	17-163
Inner part after 1995 r.	11.8-22.3	$\leq$ 62	12-168
Trigger part before 1995 r.	23-28	$\leq$ 50	30-150
Trigger part from 1995 r.	23-28	$\leq$ 105	15-165
Outer Detector	198-206	$\leq$ 232	43-137
FCA	30-103	155-165	11-33
FCB	53-195	267-283	11-35

Table 3.2: Geometric acceptance for the tracking detectors

It is thus possible to reconstruct up to 16 space points per non-helical particle trajectory. In the $r\phi$ plane, the coordinates are determined from the induced charges on the cathode pads. The z coordinate, along the cylinder axis, is calculated from the arrival time of the primary ionisation electrons.
Since the charge collected at the endcaps is proportional to the energy loss of the particle, the signal amplitude from the sense wires also provide information on the dE/dx of a particle.

- *Silicon tracker*

The Silicon tracker in DELPHI consists of concentric cylinders of silicon strips known as the Vertex Detector, and starting from 1996 also of two layers of pixels and two of ministrips in the forward region, known as the Very Forward Tracker (Fig.3.5).

  – *Vertex Detector (VD)*

  The Vertex Detector is located in the closest possible position to the interaction point, next to the beam pipe. It was modified several times. At the beginning it consisted of two concentric shells of silicon strip detectors at average radii of 9 and 11 cm and covered the central region over a length of 24 cm. The detector provided measurement of up to 2 points along a track in the $r\phi$ plane. The third layer were installed after changing the beam pipe radius to 5.65 cm. In 1994 the most inner and outer layers were equipped with double-sided silicon detectors, having strips parallel and perpendicular to the z-axis and providing the position measurements also in the z direction. The last, significant modification took place in 1996. Since then, the Vertex Detector consists of three concentric layers, each 48 cm long, at average radii of 6.6, 9.2 and 10.6 cm (Fig.3.6). Each layer covers the full azimuthal angle in 24 sectors with overlaps between adjacent sectors. It is thus possible to reconstruct up to 6 points per track in the $r\phi$ plane, as well as in the z direction.

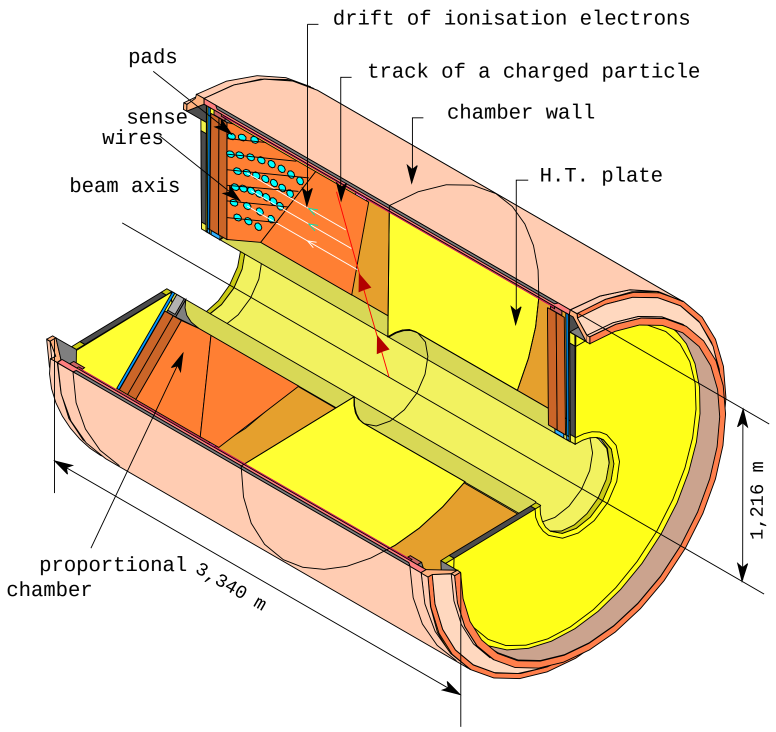

Figure 3.3: The internal structure of the Time Projection Chamber

The main objective of this detector is the reconstruction of vertices from the secondary interactions, in particular for the study of heavy flavour physics. It is also used to improve the precision of the particle impact parameter measurement.

– *Very Forward Tracker (VFT)*

In the years 1996-1997 the second part of the Silicon tracker, called the Very Forward Tracker was installed.
The aim of this detector is to improve the tracking efficiency and resolution in the polar angle region $\theta \in (10°, 26°)$ and $(154°, 170°)$. The detector is located at both ends of the VD. On each side it is built of two layers of mini-strip and two layers of pixel detectors. The pixel detectors provide measurement of up to 4 points along the track while mini-strip detectors can be used to reconstruct up to 2 points.

- *Inner Detector (ID)*

The Inner Detector provides fast trigger information and $r\phi$ coordinate measurements. The detector is located between the Vertex Detector and the TPC. It consists of two concentric sections: an inner drift chamber surrounded by triggering section. The drift chamber is divided into 24 azimuthal sectors. Inside each sector, there are 24 sense wires, strung parallel to the z-axis. The detector thus provide information about up to 24 $r\phi$ points per track. Since the beginning of 1995 a new, longer chamber has been operational. This new chamber, however, has exactly the same wire configuration as the previous one.

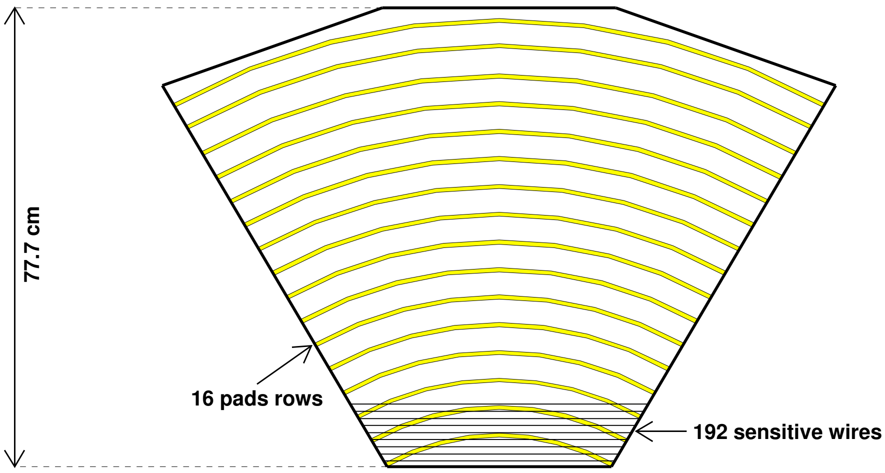

Figure 3.4: One of the TPC sectors

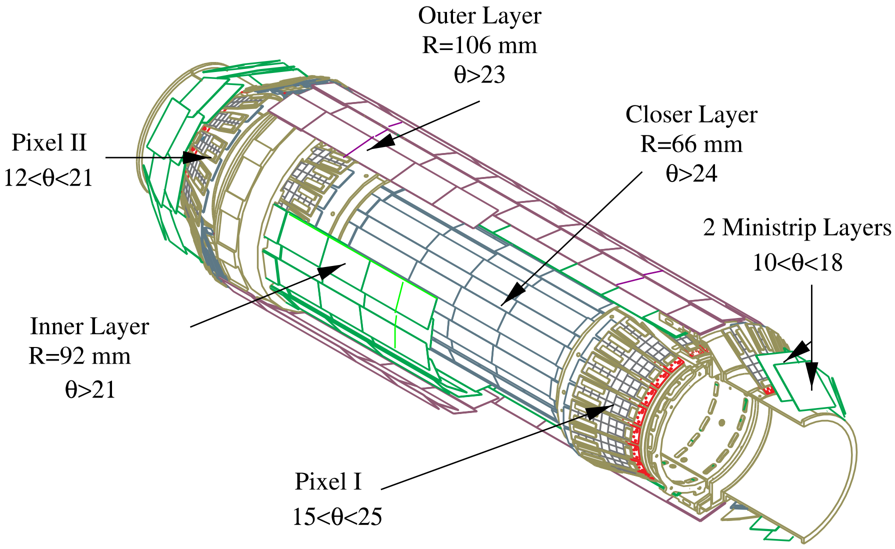

Figure 3.5: The internal structure of the Silicon tracker

The outer, *trigger* part, up to 1995 consisted of 5 cylindrical MWPC layers, with 192 anode wires parallel to the z-axis and 192 circular anode strips in each layer. The wires provided fast information about position of up to 5 points in the $r\phi$ plane while the strips provided information about the z coordinate.
In 1995, the MWPC detectors were replaced by 5 layers of straw tube detectors, with 192 tubes per layer. They have the same functionality as the old MWPC except for the measurement of the z coordinate, which was abandoned.

- *Outer Detector (OD)*

The Outer Detector is used to reconstruct the track elements about 2 meters away from the interaction point. It improves the momentum resolution of fast particles. The detector is also essential to provide fast trigger information in both the $r\phi$ plane and in the z direction.
The Outer Detector, similarly to the Inner Detector is divided into 24 azimuthal

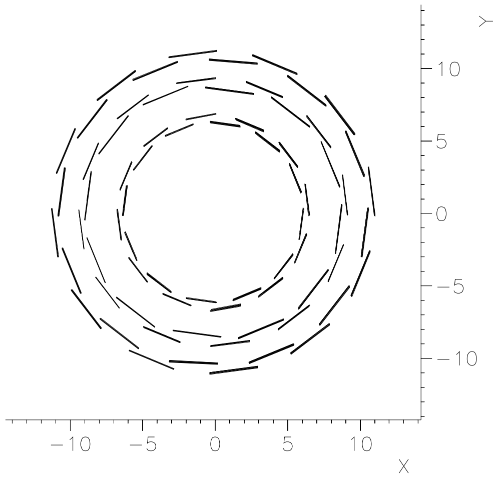

Figure 3.6: Cross-section of the Vertex Detector

sectors. It consists of five layers of drift tubes, operated in the limited streamer mode. All layers provide an $r\phi$ coordinate measurement and three also provide z measurement from the relative timing of signals at both ends of the tubes.

- *Forward Chamber A and Forward Chamber B*

  The FCA and FCB chambers are used to reconstruct track elements at polar angles θ between 11° and 35°. Similarly to the TPC, ID and OD detectors, they also provide fast trigger information.
  The chambers are positioned on both sides of DELPHI: the FCA next to the endcaps of the TPC and the FCB between the RICH and electromagnetic calorimeter. On each side, the FCA chambers contain three sets of two staggered layers of drift tubes, operating in the limited streamer mode. Additionally, each set of drift tubes is rotated by 120° with respect to the previous one, thus providing the measurement of 2×3 coordinates: xx', uu', vv', where x' is staggered with respect to x.
  The FCB is a conventional drift chamber with two independent semi-circular modules in each endcap. The 12 sense wire planes are rotated in pairs by 120° with respect to each other. It is possible to reconstruct up to 4 points along the track in the same coordinates as for the FCA.

3.2.2 Calorimetry

Calorimeters aim is to measure the energy of charged and neutral particles. They are usually made as a sandwich of a high density material in which a particle energy is absorbed and the detectors which transform this energy into a measurable signal[2].
Calorimeters can also provide information which can be used by the trigger system.
The DELPHI detector is equipped with hadronic calorimeter (HCAL) to measure hadrons energy and four electromagnetic ones to measure the energy of electrons and photons (HPC, FEMC, STIC/SAT and VSAT). The last two are positioned at the small angles with respect to the beam axis and are principally used for the luminosity measurement

[2]some materials, as lead glass, play both these roles at the same time

(see section 3.1.1) but also for detection of primary electrons, deflected after photon-photon interaction. The geometric acceptances of the calorimeters described below are given in Table 3.3.

Detector name	Geometric acceptance		
	r [cm]	$\mid z \mid$ [cm]	θ [°]
Electromagnetic calorimeters:			
HPC	208-260	$\leq$ 254	43-137
FEMC	46-240	284-340	10-36.5 i 143.5-170
STIC (from 1994)	6.5-42	220-249	1.7-10 i 170-178.3
SAT (to 1994)			2.5-8 i 172-177.5
VSAT	6-11	770-780	0.3-0.4
Hadronic calorimeter:			
barrel	320-470	$\leq$ 380	43-137
forward	65-470	$\leq$ 340-489	11-48.5

Table 3.3: Geometric acceptance for the DELPHI calorimeters. In case of VSAT, the acceptance in θ is for the particles of beam energy.

- *High-density Projection Chamber (HPC)*

  The HPC is a calorimeter which uses the time projection technique to collect the charge from electromagnetic showers. It provides not only energy measurement but also their full, three-dimensional reconstruction.
  The detector consists of 144 modules arranged in 6 rings, located in the barrel part of the DELPHI detector between the Outer Detector and the superconducting solenoid.
  Each HPC module is a small TPC with layers of high density material dividing the gas volume. These layers are made out of lead wires which act as the conversion material and also provide the drift field. As in the TPC, each module is equipped with a proportional wire chamber with cathode pads of a changing geometry (Fig.3.7).

  For triggering purposes, in each module a plane of scintillators is inserted into one of the HPC drift channels, close to the shower maximum.

  The energy resolution for the HPC can be parametrised as:

  $$\sigma(E)/E = 0.043 \oplus 0.32/\sqrt{E}$$

  for energy E in GeV [3].

- *Forward Electromagnetic Calorimeter (FEMC)*

  The FEMC calorimeter is situated in both endcaps of the DELPHI detector, between the FCB chambers and hadronic calorimeter. Each endcap contains an array of 4532 lead glass blocks, formed in a shape of truncated pyramids which are mounted to point near to the interaction region.
  The charged particles of the electromagnetic shower that develops in the calorimeter

[3] $a \oplus b = \sqrt{a^2 + b^2}$

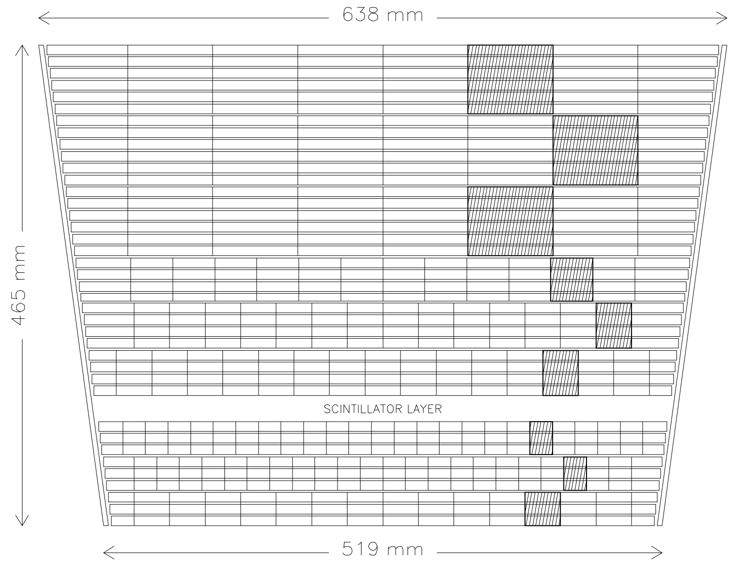

Figure 3.7: Cross-section of one HPC module demonstrating the organisation of the HPC readout. Shown are pads, scintillator layer and module dimensions. Hatched area illustrates possible shower development.

emit Cherenkov photons (see section 3.2.3). Because of the magnetic field, phototriodes are used for the readout. The energy resolution is given by formula:

$$\sigma(E)/E = 0.03 \oplus 0.12/\sqrt{E} \oplus (0.11/E)$$

where E is in GeV. FEMC contributes to the trigger decision at all levels.

- *Hermeticity detectors*

  In order to cover the holes in the electromagnetic calorimetry and provide full hermecity of the detector, various lead-scintillator sandwich counters have been installed: 90-degree and 40-degree counters and so called ϕ Taggers that are placed directly after the ϕ cracks between the HPC modules.

- *Electromagnetic calorimeters STIC and SAT*

  The Small Angle Tile Calorimeter (STIC) is composed of two cylinders placed on both sides of the DELPHI interaction point. Its aim is to measure energy of electrons and photons produced at small angles with respect to the beam axis. Such electrons comes mainly from Bhabha ($e^+e^- \rightarrow e^+e^-$) process used to determine the e^+e^- luminosity and from two-photon interactions. The luminosity measurement is discussed in section 5.4.
  Each cylinder is built of 47 lead-scintillator layers. The light produced in the scintillator is read by wavelength shifting optical fibres, placed perpendicularly to the scintillator tiles. The relative precision on the measured energy can be parametrised as

$$\sigma(E)/E = 0.015 \oplus 0.14/\sqrt{E}$$

  where E is in GeV. Since the end of 1995, the detector is also equipped with two layers of silicon strips, embedded in the calorimeter, which help to reconstruct the shower direction. Additionally, in front of the calorimeter two layers of scintillator are situated. They are used to separate charged from neutral particles.

The STIC calorimeter replaced in 1994 the other calorimeter with smaller geometric acceptance - the Small Angle Tagger (SAT). Each arm of this detector consisted of a calorimeter and a tracker. The calorimeter was built of the three layers of silicon detectors while the tracker was built of lead sheets and plastic scintillating fibres. The energy resolution is given by:

$$\sigma(E)/E = 1.2 \oplus 11.4/\sqrt{E} + 2.3$$

where E is in GeV. Both SAT and STIC calorimeters provide trigger signals, mainly used to trigger on the Bhabha events.

- *Hadron Calorimeter (HCAL)*

  The aim of the Hadron Calorimeter is to measure energy of the hadrons in the barrel part as well as in the endcaps of the DELPHI detector. The conversion material of the calorimeter is also the return yoke of the DELPHI solenoid. HCAL is the sampling calorimeter with layers of limited streamer tubes inserted into slots between the 5 cm thick iron plates. In the barrel region, the energy resolution of the calorimeter is found to be

  $$\sigma(E)/E = 0.21 \oplus 1.12/\sqrt{E}$$

  where E is in GeV. HCAL contributes to the trigger decision with signals corresponding to the three energy thresholds: 0.5, 2 and about 5 GeV.

3.2.3 Detectors for particle identification

Hadron identification in the DELPHI detector is based on two phenomena: particle specific ionisation energy loss and emission of Cherenkov radiation. Electrons can also be identified in electromagnetic calorimeters. Finally, high-momenta muons can be distinguished from hadrons thanks to their high penetration ability. Therefore muon chambers are situated inside and just outside of the Hadron Calorimeter.

- *Time Projection Chamber and Vertex Detector*

  Both detectors have been described in the section concerning tracking detectors. They are, however, used not only to reconstruct tracks of the charged particles, but also to identify them by measurement of their ionisation energy loss, dE/dx. The sense wires of the TPC provide up to 192 ionisation measurements per track, while VD can provide up to 6 measurements.

- *Ring Imaging Cherenkov Counter (RICH)*

  Out of four detectors at LEP DELPHI is the only one, where the emission of Cherenkov light is used for particle identification.
  Charged particle travelling faster than the local speed of light in a dielectric medium,

cause the molecules of the medium to emit Cherenkov light in a cone around the particle trajectory. The opening angle of this cone depends on the refractive index of the radiator medium and on the velocity of the particle. Thus Cherenkov angle and momentum measurements, combined together give an estimate of the particle's mass. For a given refractive index, with the increase of a particle's momentum the Cherenkov angle achieve the certain value independent of its mass. To identify particles over a wide momentum range, two different radiators are used in the DELPHI detector: a liquid radiator (D_6F_{14}) and a gas one (C_4F_{10}). The liquid radiator is used to identify particles of low momenta, between 0.7 and 8 GeV, and a gas radiator is used from 2.5 to 25 GeV.
The barrel RICH covers polar angles between 45° and 135°.

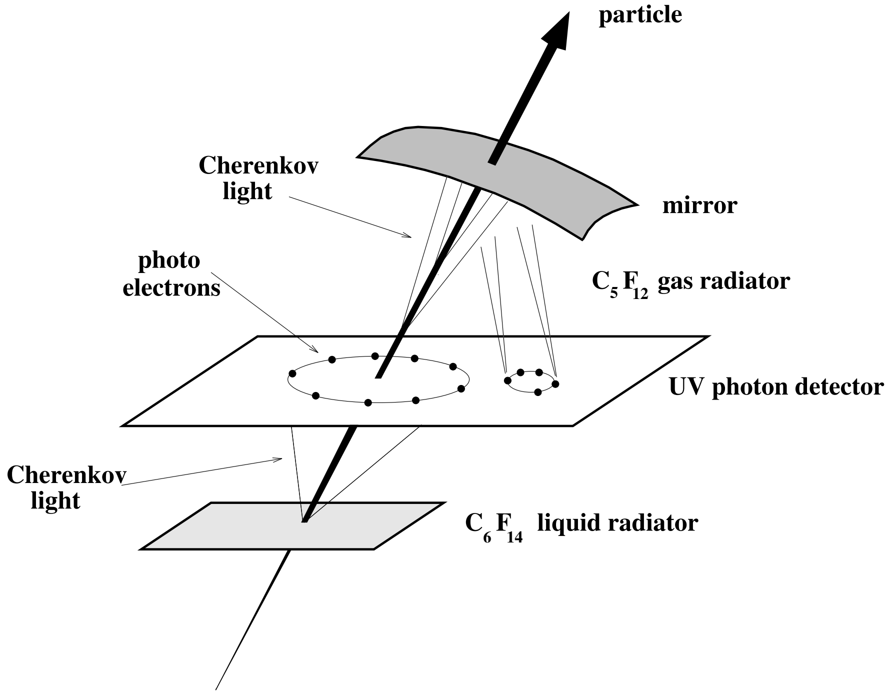

Figure 3.8: Principle of operation of the DELPHI Ring Imaging Cherenkov detector

A particle travelling from the interaction point, first meats on its way the 1 cm thick liquid radiator. The Cherenkov light is projected directly onto a UV-sensitive photon detector which converts UV-photons into photo-electrons. These electrons appear in a ring-like or parabolic configuration, depending on the particle incident angle. Forty-two centimetres thick gas radiator is situated behind the photon detector. The Cherenkov light from this radiator is reflected by focusing mirrors onto the same photon detector (Fig.3.8).
This detector is a TPC-like drift chamber, inside which the electrons liberated by Cherenkov photons drift towards the multi-wire proportional chamber. The walls are made out of quartz to allow Cherenkov photons transmission.
The Forward RICH, situated in endcaps, covers the angles $15° < \theta < 35°$ and $145° < \theta < 165°$. Principle of operation is the same as in case of barrel detector.

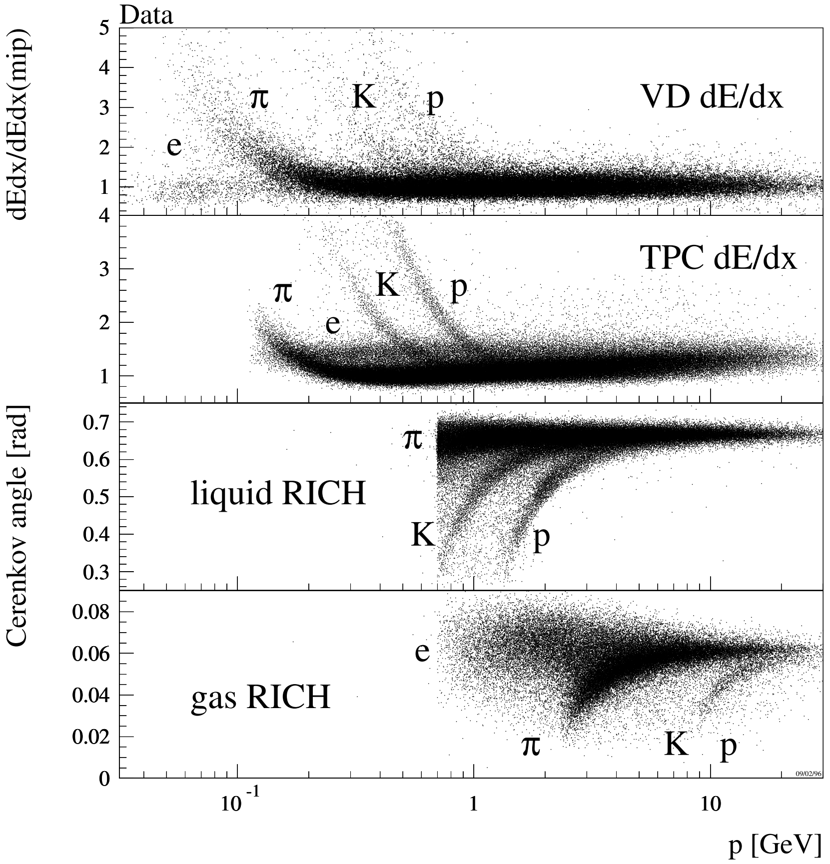

Figure 3.9: Energy loss dE/dx in the Vertex Detector and TPC and average Cherenkov angle in the liquid and gas RICH as a function of the momentum of the track. The plot is taken from [30].

- Particle identification capabilities of the DELPHI detector with dE/dx measurement in the TPC and Vertex Detector as well as with Cherenkov angle measurements in the liquid and gas RICH are shown in Fig.3.9.

- *Muon Chambers*

  The iron of the Hadron Calorimeter acts as a filter which provides effective separation between high-momenta muons and hadrons. Most hadrons are stopped by this material, while muons of momenta above 2 GeV are expected to reach Muon Chambers without too much of Coulomb scattering.
  The DELPHI muon detection system consists of three separate sub-detectors: Barrel, Forward and Surround Muon Chambers. The last ones cover the gap between the barrel and the endcap regions.
  This system of the detectors is not only used to identify muons, but also contributes to the trigger decision at all levels.

  - *Barrel Muon Chambers (MUB)*
    The detector is composed of three layers of modules and is divided into 24 azimuthal sectors. The inner layer lies behind 90 cm of the iron, inside the Hadron Calorimeter. It is built of three layers of staggered drift chambers.

The outer layers are placed behind another 20 cm of the iron, already outside the HCAL. They consist of drift chambers arranged in two active planes. The $r\phi$ coordinates are measured from the arrival time of the ionisation electrons. The z coordinate is determined by the relative timing of the signals travelling on the delay line to the ends of the chamber.

– *Forward Muon Chambers (MUF)*
At each side of the interaction point, the MUF is composed of two detection planes. The first lies behind 85 cm of the iron, inside the HCAL and the second behind another 20 cm of the iron and the layer of scintillators. Each plane consist of two layers of orthogonal drift chambers, operating in limited streamer mode. As in case of MUB, one track coordinate is determined from the anode signal timing. The delay line, parallel to signal wire, is used to determine the orthogonal coordinate.

– *Surround Muon Chambers (MUS)*
The Surround Muon Chambers were installed in 1994 to cover the gap between the MUB and MUF chambers at a polar angle of around 45°. At each side of DELPHI, the MUS are built of eight modules. Each module consist of two staggered layers of streamer tubes.

- *Scintillator counters*

In the DELPHI detector, two systems of scintillator counters are installed, *Time Of Flight counters (TOF)* in the barrel part and *Forward scintillator Hodoscope (HOF)* in the endcaps.
TOF counters are located between the solenoid and the Hadron Calorimeter. They provide fast trigger information which allows to distinguish a cosmic ray event from the beam-beam interactions.
HOF scintillators are situated behind the Forward Hadron Calorimeter and produce fast and practically standalone muon trigger in the endcaps.

3.3 Trigger

The main purpose of a trigger system is to select with the highest possible efficiency all interesting physics events and to keep, at the same time, the background event rate reasonably low.
The collisions at LEP take place every 11 μs for 8×8 bunch configuration or every 22 μs for 4×4 configuration (section 3.1). However, only in a small fraction of beam crossings ($\sim 10^{-5}$) the e^+e^- or $\gamma\gamma$ interaction take place. For example, the cross-section for production of Z^0 boson decaying into hadrons, at the e^+e^- centre-of-mass energy $\sqrt{s} = 91$ GeV is about 32 nb. At the luminosity $\sim 1.5 \times 10^{31}\mathrm{cm}^{-2}\mathrm{s}^{-1}$ such events are produced with the frequency:

$$\frac{dN}{dt} \approx 32[\mathrm{nb}] \times 1.5 \times 10^{31}[\mathrm{cm}^{-2}\mathrm{s}^{-1}] = 0.48Hz$$

comparing with the frequency of beam crossings: 90 kHz or 45 kHz. The rare interesting events have to be thus chosen from the huge amount of empty and background events and from the detector noise.

To cope with this situation, the DELPHI trigger system is composed of four successive levels (T1,T2,T3,T4) of increasing selectivity. The first two levels [31], T1 and T2, are the hardware triggers which are synchronous with the Beam Cross Over signal (BCO). It means that decisions at these levels are always taken after the fixed period of time after bunch crossing. In contrast, the third and fourth [32] level software filters, T3 and T4, are performed asynchronously with respect to BCO.
The T1 and T2 trigger decisions are taken 3.5 μs and 39 μs after BCO respectively, implying that for each positive T1 decision 1 or 3 consecutive beam crossings are lost depending on the number of bunches. The T3 and T4 decisions are taken approximately 20 ms and 500 ms after BCO.
T1 and T2 have been active since the start of DELPHI operation in 1989. T3 was implemented in 1992. T4 was implemented in 1993 to tag and in 1994 to reject, about half of the background events remaining after T3. When the LEP entered into higher-energy phase, T4 trigger was disabled, but it was put in operation again in 1997, on September 16th.

3.3.1 The first level trigger (T1)

T1 acts as a loose pre-trigger. The decision taken relies only on information from individual detectors with fast read-outs (Fig.3.11):

- the fast tracking detectors (ID,OD,FCA,FCB) and endcap wire plane of the TPC),
- the scintillator arrays (TOF,HOF),
- the scintillators inside the HPC,
- Forward Electromagnetic Calorimeter (FEMC),
- Barrel Muon Chambers (MUB).

No correlation between different subdetectors is introduced. At this level the requirements considered in the trigger decision are very simple: low energy single clusters in the calorimeters, simple pattern in track chambers or scintillation counter hits. The trigger rate is typically 700 Hz.

3.3.2 The second level trigger (T2)

At the second level, data from detectors with long drift times, TPC, HPC and MUF, are already available and information from other detectors is more refined. Individual subdetector signals with low counting rates can produce their own triggers. For more noisy subdetectors this would lead to large event rates, so the combination of signals from different subdetectors is used. A positive T2 decision triggers the acquisition of the data collected by the front-end electronics. The trigger rate is about 5Hz.

3.3.3 The third level trigger (T3)

The T3 software trigger has been developed in order to maintain the data logging rate close to 2Hz. It repeats the logic of second level trigger using more detailed detector information. Thus introduction of further algorithms or correlations between subdetectors, in comparison to T2, is avoided.

3.3.4 The fourth level trigger (T4)

The aim of the fourth level software trigger was originally to tag, in real time, all Z^0 decays produced in the detector with emphasis placed upon interesting topologies as predicted by models for new physics. However, it appeared that the relatively low event rates are achieved after T3, so that the complete processing is possible. As a result, T4 is used as a fourth level of the trigger system and reduces about half of the background events remaining after T3.

3.3.5 The Trigger Logic

The main part of the DELPHI trigger system [33] is the central trigger decision box, called PYTHIA. It receives the subtrigger data from the different subdetectors and, on the basis of a programmable logic, takes the trigger decision at first two levels: T1 and T2.
At each of these levels, the trigger logic is constructed in three steps corresponding to a three level structure of look-up-tables (LUT) as shown in Fig.3.10. The look-up tables are in fact the logical functions with n inputs and m outputs. They are programmable, so it is possible to easily modify the trigger decision functions.
At the A-level there are 40 LUTs, at the B-level 4 LUTs and finally at the C-level only 1 look-up-table.

The A-level is feeded by 120 Trigger Data Lines (TDL) coming from different subdetectors. Logical combinations of these inputs, in terms of logical ORs and ANDs, are called Component Functions (CF). These functions are then used to form another set of signals, the Term Functions (TF) which are defined as logical products of CFs. At each level a maximum of 640 programmable CFs and 64 TFs is permitted.
At the B-level, the TFs are joined in different groups according to the specific detector acceptances (barrel, forward, backward, intermediate region) or physics requirements like single tagged $\gamma\gamma$ events. Within each class, a set of coincidences between the components is defined, and at the same time some combinations are forbidden (masked). The logical OR of these possible coincidences is known as a *majority*.
The *level 1 majority* is made of single TFs - in other words there is no coincidence between different components. The *level 2 majority* consist of coincidences between only two TFs, in the *level 3 majority* three TFs form coincidence, etc.

The maximum number of *majorities* for each level is 64. This would correspond to the situation when all possible TFs are regarded as level 1 *majorities*. With these *majorities* the 16 Decision Functions (DF) are built up. Each of these functions may consists of a logical OR made from a group of several *majorities*.
The final DELPHI trigger on the first and second level is then a logical OR of these 16 functions which can be independently masked out (eliminate from the taking of the final decision) or prescaled by a factor of up to 255:

$$\mathrm{i-th\ level\ trigger} = \sum_{j=0}^{15} \alpha_j \beta_j^{-1} \mathrm{DF}_j\,, \quad \alpha_j = 0 \ \text{ or } \ 1, \quad \beta_i \leq 255, \quad i = 1 \ \text{ or } \ 2. \tag{3.1}$$

The decision functions from the first level trigger are used as inputs (TDLs) at the second level. One of the decision function from T2, used in 1994 is shown in Table 3.4 This is an example of *level 2 majority*.

DF07_II, Forward/backward part		
	TF	Description
1	TPCFW_MJ1	single track in TPC, in forward region ($20^\circ < \theta < 43^\circ$)
2	TPCBW_MJ1	single track in TPC, in backward region ($137^\circ < \theta < 160^\circ$)
3	TRFW_MJ1	single track in FCA/FCB, in forward region
4	TRBW_MJ1	single track in FCA/FCB, in backward region
5	MUFW_MJ1	single track in forward muon chambers
6	MUBW_MJ1	single track in backward muon chambers

Table 3.4: One of the trigger decision function at second level in 1994.

This function (and the whole trigger) fires if at least one coincidence of 2 signals out of 6 forming the majority is fired. The following combinations are forbidden: 1-2, 1-3, 1-4, 2-3, 2-4, 3-4, 3-6, 4-5, 5-6.

The example of 1994 decision functions for the first and the second level can be found in Appendix C.

3.4 Off-line data processing

If the event is accepted by the trigger system, it is written to disk and then copied to tape in a form of raw data. The raw data consist of the unprocessed digitised signals from each of the detectors and must be further processed by the DELPHI off-line system to produce data suitable for use in physics analyses. The main part of this processing is performed by the DELphi data ANAlysis package DELANA [35]. This program performs the calibration and alignment of the raw data, track and vertex reconstruction and preliminary particle identification.
The output of DELANA is a Data Summary Tape (DST), called Full DST.
From the Full DST, the condensed versions of DST (Short DST, XShort DST) are produced by DSTANA package. The main aim of this step is not only to save the disk space and reduce the time of the physics analyses. At this stage refitting of the tracks and vertices, final particle identification, b-event tagging and all possible fixings are performed.
A number of standard tools exist in DELPHI for extracting information from DST. The analysis described here relies upon the packages PHDST [36, 30] and SKELANA [30].

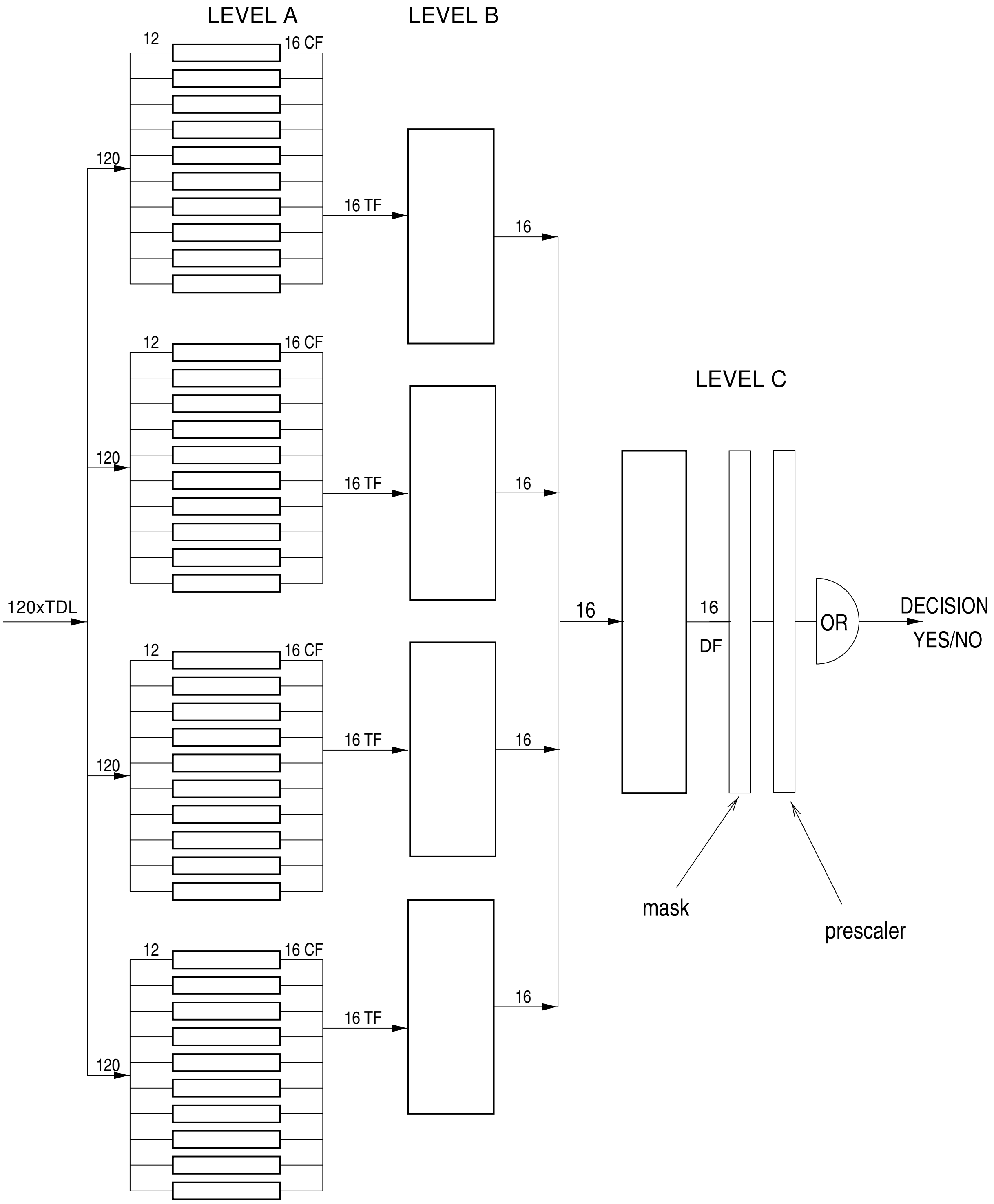

Figure 3.10: Schematic view of the trigger decision box (PYTHIA). Rectangles represent look-up-tables. At the C-level - also masking and prescaling modules. At the A-level, LUTs are organised in four blocks. Each block has a duplication of the 120 TDLs as input.

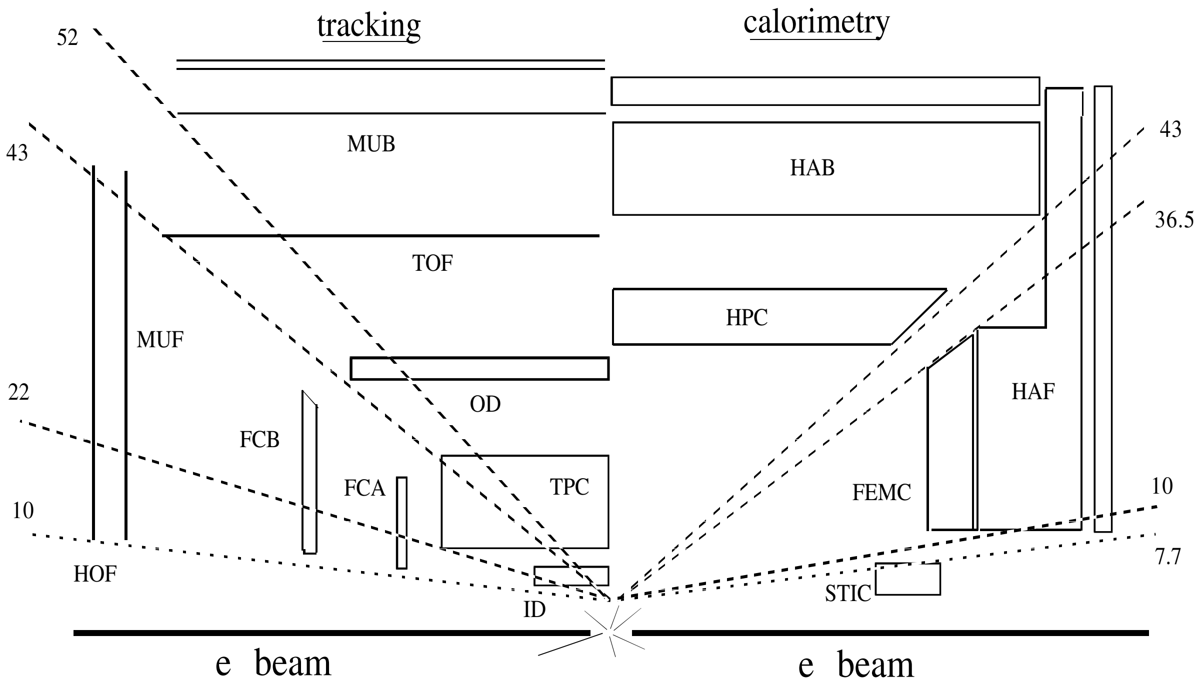

Figure 3.11: Subdetectors participating in the first and second level trigger and their polar angle acceptances in degrees [34].

Chapter 4

Monte Carlo Simulations

4.1 Event generators

In the analysis, several event generators were used to produce four-vectors $(E, \vec{p})$ of final state particles typical of those that would result from a given physics process. These four-vectors were then passed through the detector simulation (see next section).
In the following the main features of the programs are shortly described. For further details the reader is referred to the original publications. An overview can be found in [8, 11].

4.1.1 The Vermaseren 1.01 program

The Vermaseren program [37, 38] is regarded as the standard Monte Carlo for two-photon production of lepton pairs as the full dependence on the lepton masses and on the photon virtualities is kept. In addition to the lepton pair production: $e^+e^- \to e^+e^-l^+l^-$, the other final states, as $e^+e^- \to e^+e^-q\bar{q}$ and $e^+e^- \to e^+e^-\pi^+\pi^-$ can also be generated. The latter includes formation of the resonance $f_2(1270)$ and the continuum with the interference between them. The resonance production is described by the model of Krasemann and Vermaseren [39] where the interacting photons can be quasi-real or virtual. In this model the cross-section for the process $\gamma\gamma^* \to f_2 \to \pi^+\pi^-$ with one real and one virtual photon is:

$$\sigma(\gamma\gamma^* \to f_2 \to \pi^+\pi^-) = 40\pi \frac{\Gamma_{\pi^+\pi^-}\Gamma_{\gamma\gamma}}{(W^2_{\gamma\gamma} - M^2_R)^2 + M^2_R\Gamma^2_{tot}} F(W^2_{\gamma\gamma}, q^2) \tag{4.1}$$

where $F(W^2_{\gamma\gamma}, q^2)$ is the effective form factor given by the formula:

$$F(W^2_{\gamma\gamma}, q^2) = \frac{M^2_R(4W^4_{\gamma\gamma} + 2W^2_{\gamma\gamma}q^2 + \frac{2}{3}q^4)}{(W^2_{\gamma\gamma} - q^2)(W^2_{\gamma\gamma} - 2q^2 + M^2_R)^2} \tag{4.2}$$

For $q^2 = 0$ this form factor gives some dependence on $W_{\gamma\gamma}$ which is however negligible as compared to the Breit-Wigner formula.
The continuum process is approximated by the pure Born term where pions are assumed to be point-like particles. The resonance and continuum can be generated separately.
For the purpose of this thesis, the events from the process $e^+e^- \to e^+e^-l^+l^-$ were generated according to the multipheripheral diagram from Fig.4.1. In case of resonance production, the resonance parameters were taken from [1].

The Vermaseren generator was used to compare muon and pion data with the theoretical models included in the Monte Carlo and to find the detector acceptance.

4.1.2 The BDKRC program

The BDKRC Monte Carlo, called also RADCOR [40] can produce events according to multipheripheral diagram. It is similar to the part of Vermaseren program responsible for two-photon production of fermion pairs but QED radiative corrections to the electron and positron lines have been added. The possible final states are $e^+e^- \to e^+e^-l^+l^-(\gamma)$ $(l = e, \mu, \tau)$ and $e^+e^- \to e^+e^-q\overline{q}(\gamma)$.
This generator was used to check the influence of initial and final state radiation on the final results.

4.1.3 The DIAG36 program

The DIAG36, called also BDK [41, 42] is an event generator for four fermion processes, $l^+l^-f^+f^-$, where l is the charged lepton (e, μ, τ) and f is the charged lepton or a quark. The events are produced according to 36 diagrams which can be divided into four groups shown in Fig.4.1 for the processes $e^+e^-f^+f^-$. The BDK program was used to estimate the background from processes with two electrons and two leptons in the final state, which does not proceed through the two-photon interactions. It includes also full treatment of fermion masses but does not include radiative corrections. This program was especially designed for the untagged two-photon events.

4.1.4 The GALUGA 2.0 program

In the four-fermion generators described above, the differential cross-section is not explicitly decomposed into the functions $\sigma_{\alpha\beta}, \tau_{\alpha\beta}$ (see equation 2.9). The full matrix element is calculated as a whole. This is, however, usually not possible in case of hadronic final states, because the hadronic behaviour of the photon does not have the perturbative origin.
In the GALUGA [43] program the cross-section for two-photon process $e^+e^- \to e^+e^-X$ as a function of $\sigma_{\alpha\beta}, \tau_{\alpha\beta}$ has been implemented. In case of lepton pair production $\sigma_{\alpha\beta}, \tau_{\alpha\beta}$ are well known. In particular, in the program the formulas from the paper by Budnev et al. [2] have been implemented. Much less is known about these functions for hadronic processes. In this case the author of the program has assumed $\tau_{\alpha\beta} = 0$, while for $\sigma_{\alpha\beta}$ the factorisation:

$$\sigma_{\alpha\beta}(W_{\gamma\gamma}^2, Q_i^2) = h_\alpha(Q_1^2)h_\beta(Q_2^2)\sigma_{\gamma\gamma}(W_{\gamma\gamma}^2) \tag{4.3}$$

has been used. This factorisation is valid for $Q_i^2 \ll W_{\gamma\gamma}^2$. The factors h_α and h_β describe the photon-virtuality effects. In this thesis the simple ρ-pole model has been used:

$$h_T(Q^2) = \left(\frac{m_\rho^2}{m_\rho^2 + Q^2}\right)^2 \tag{4.4}$$

$$h_L(Q^2) = \frac{Q^2}{4m_\rho^2}\left(\frac{m_\rho^2}{m_\rho^2 + Q^2}\right)^2 \tag{4.5}$$

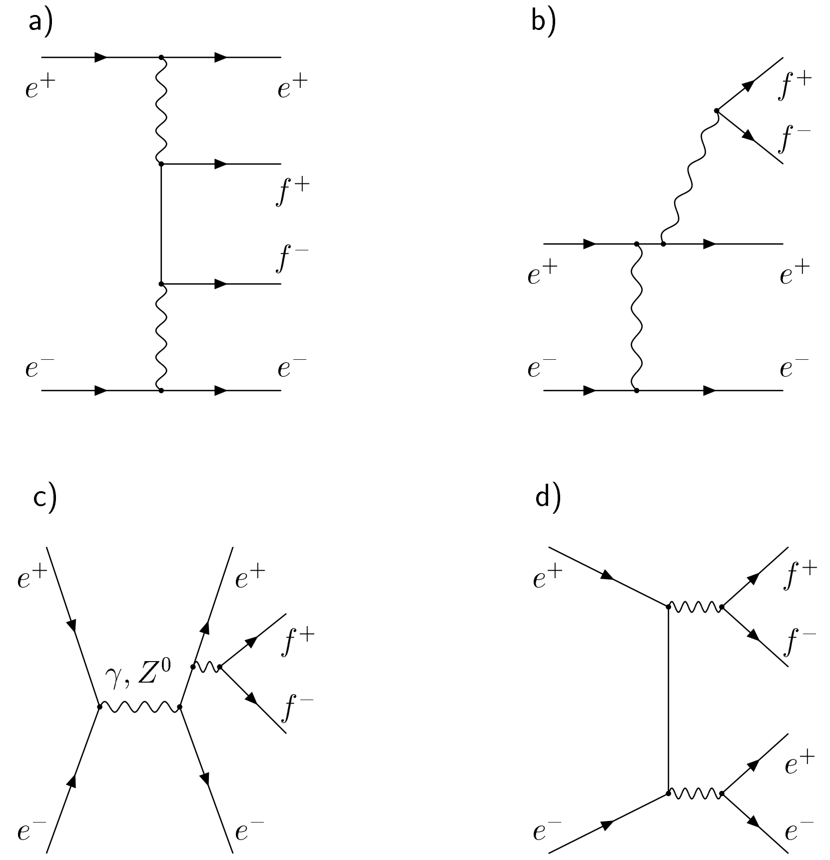

Figure 4.1: The four main diagrams contributing at the lowest order to the processes $e^+e^- f^+f^-$, where $f = e$, μ, τ, q: a) multipheripheral, b) bremsstrahlung, c) annihilation and d) conversion diagrams.

All dependences on the electron mass and the photon virtualities Q_i^2 are fully kept. For the purpose of this analysis the modified version of the GALUGA program, which allows simulation of K^+K^- and $\pi^+\pi^-$ pairs in the final state was used. Meson pairs were generated from the flat distribution in $\cos\theta^*$. The cross-sections for interaction of two real photons in the processes $\gamma\gamma \to \pi^+\pi^-$ and $\gamma\gamma \to K^+K^-$ were taken to be proportional to $1/W_{\gamma\gamma}^6$, as suggested by the QCD-based models [18].

4.2 Detector Simulation

In order to estimate the detector efficiency i.e. to find the ratio of the number of events that are detected to the number of generated ones, the simulation of the particles behaviour in the detector is necessary.
In the DELPHI experiment, the detector simulation program is called DELSIM [44]. The program describes in details all known properties of the detector (geometry of the subdetectors, material distribution, magnetic field) and simulate possible secondary interactions (Compton scattering, photon conversion, bremsstrahlung, δ-ray production, hadronic interactions, positron annihilation, photoelectric effect) and particle decays. Information about hits in all subdetectors is the output from the program. It is written in the same

format as the raw data. For the purpose of this analysis, the four-vectors $(E, \vec{p})$ of produced particles, obtained from event generators, were used as the input to DELSIM, passed through the detector simulation and processed by the same chain of programs as the experimental data (see section 3.4).
In order to avoid processing of the events which have no chance to pass the final selection cuts at the detector level (e.g. particles disappear in the beam pipe), simple cuts on minimal polar angle θ of each particle and on minimal invariant mass of the final system were introduced. Only events which fulfilled these cuts were passed through the detector simulation.
Simulations were done separately for different years, because the detector was modified several times. All informations about simulated data samples are collected in Table B.1 in Appendix B.
The detector resolution in several variables found on the basis of the process $\gamma\gamma \to \pi^+\pi-$ as implemented in Vermaseren Monte Carlo is shown in Fig.4.2. Similar results can be obtained from Galuga Monte Carlo.

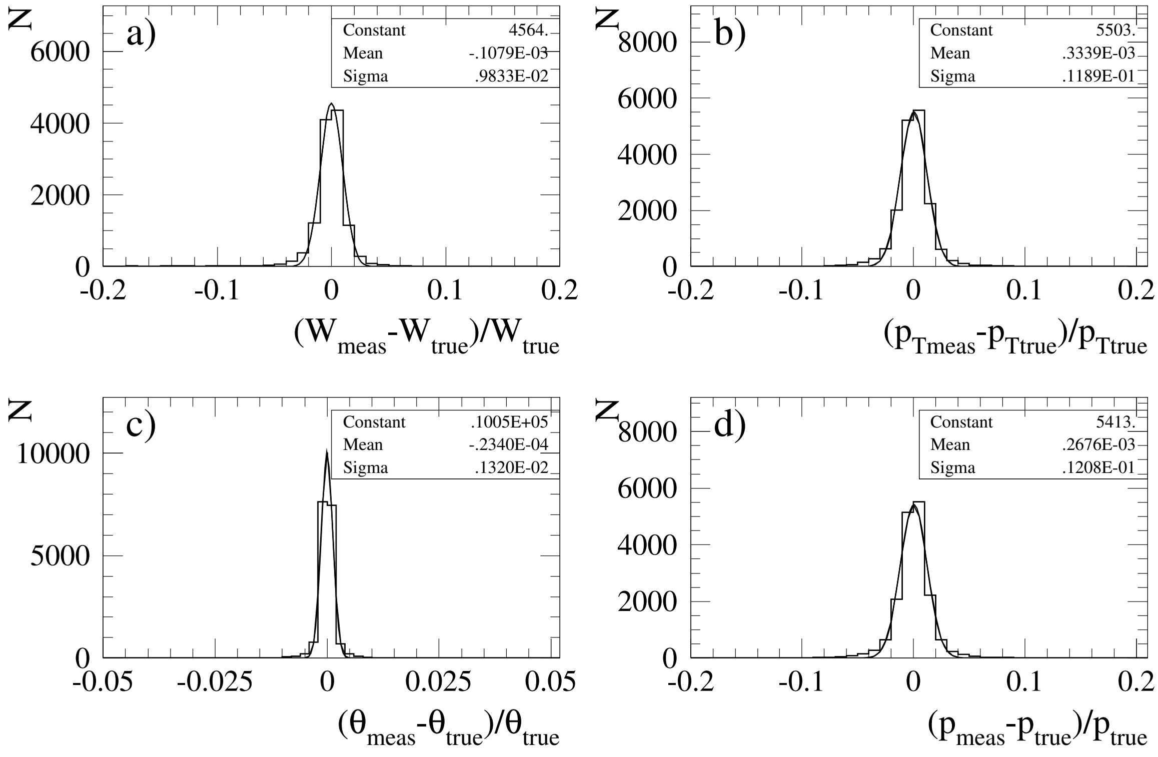

Figure 4.2: Resolution in a) invariant mass, b) transverse momentum, c) polar angle and d) momentum of the track from Vermaseren Monte Carlo for the process $\gamma\gamma \to \pi^+\pi^-$. Gaussian fits to the distributions and their parameters are also shown.

Chapter 5

Data Analysis

5.1 Introduction

The analysis described in this thesis is based on the data collected by the DELPHI experiment in the years 1992-1995 at the e^+e^- centre-of-mass energy $\sqrt{s}$ = 91 GeV and in the year 1997 at $\sqrt{s}$ = 183 GeV.
The investigated process is two-photon production of charged kaon and pion pairs in untagged events where electron and positron scatter at very small angles ($\lesssim 2°$) and disappear in the beam pipe. The Monte Carlo generated Q^2 and energy distribution for the photons is shown in Fig.5.1.
Therefore in the ideal case, only tracks of two charged particles should be seen in the detector. These particles usually have low momenta and their transverse momenta are in the range in which the detector, and especially the trigger system were not optimised for. In this chapter the event selection is described in the first place, starting from the description of how to extract two *good* low momentum tracks from the sea of badly reconstructed tracks and tracks from secondary interactions, beam-gas interactions etc.
Then follows a discussion of particle identification, detector performance and trigger efficiency studies that have been performed. The important part of this chapter is the description of the method used to find the trigger efficiency, implication of this method

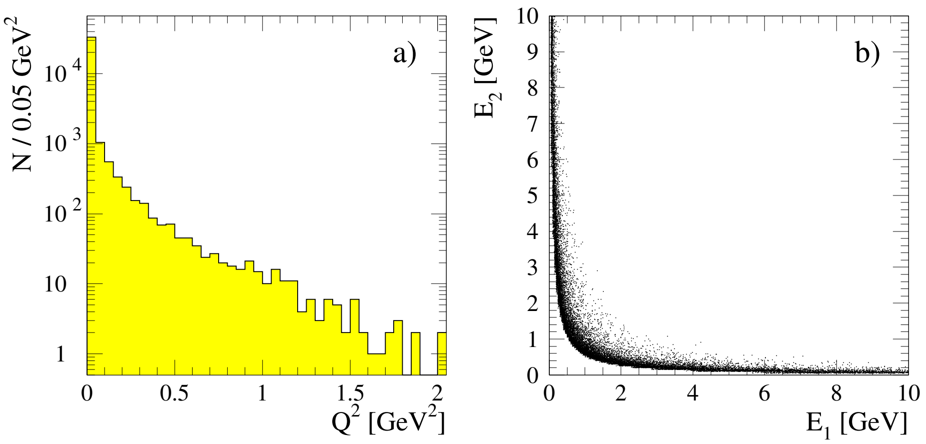

Figure 5.1: Distribution of a) Q^2 of the photons and b) energy of one photon versus energy of the second photon from Galuga Monte Carlo for the process $\gamma\gamma \to \pi^+\pi^-$; $\sqrt{s}$=91 GeV; maximum polar angle of the scattered electrons $\lesssim 2°$.

on the selection of the final sample and results concerning trigger efficiency in the unexplored so far in DELPHI region of low-multiplicity events with low-momenta tracks. Finally, the muon, kaon and pion selection is described, the quality of the data samples and agreement between data and Monte Carlo is checked. The last section contains also the discussion of possible backgrounds.
The experimental data are usually shown together for the years 1992-93, 1994-95 and separately for the year 1997. Data from different years were combined if detector components were basically the same and it was possible to define the same trigger conditions. However, the Monte Carlo simulation was performed for each year separately.
It is worth to stress here that in the following two methods of data presentation are used:

- experimental data and Monte Carlo for signal and background are shown in the same figure; Monte Carlo is normalised to the luminosity of the data; errors are statistical only; experimental data are corrected for the trigger efficiency but not for the detector acceptance and identification efficiency - they are taken into account in the detector simulation (see sections 3.4,4.2);
- cross-sections for the process $\gamma\gamma \rightarrow X$ are presented.

5.2 Event Selection

5.2.1 Two-prong selection

The first step in the two-prong selection is to define *good* charged track, which:

- is not created from the noise hits in a detector,
- is not an effect of imperfect work of the reconstruction program,
- is not a product of a secondary interaction of a particle with the material in the detector,
- is not a cosmic ray particle,
- does not come from beam-gas interactions.

For extracting a cross-section for a given process, it is essential to not to loose good two-prong events because of additional track(s) from the processes mentioned above. It is especially important in case of processes such as beam-gas interactions, which are not included in the detector simulation. Some interesting events are collected in the Appendix A.
The variables which effectively discriminate between *good* and fake tracks are impact parameters. The impact parameter is defined as the distance of closest approach of the track to the electron beam collision point, called beam-spot.
Here, we cut on the distance of closest approach to the beam-spot measured along the z-axis (Imp_z), and on the distance measured in the $r\phi$ plane to this point ($Imp_{r\phi}$) :

- $Imp_z < 4\text{cm}/\sin\theta$
- $Imp_{r\phi} < 4\text{cm}$

The $\sin\theta$ dependence was introduced, because Imp_z is measured less precisely when a particle is travelling in the forward direction.
The sign of the impact parameter of, for example, negatively charged particle travelling from the perigee is defined as positive if the trajectory encircles the origin.
The *good* tracks should in addition satisfy the following criteria:

- polar angle $\theta \in (20°,160°)$,
- momentum $p > 0.2$ GeV,
- the error on the momentum should be smaller than the momentum itself: $\Delta p/p < 1$,
- track length > 30 cm.

Additionally, the good performance levels (see section 5.4) from tracking detectors were required.
An event is selected if exactly two *good*, oppositely charged tracks have been found.

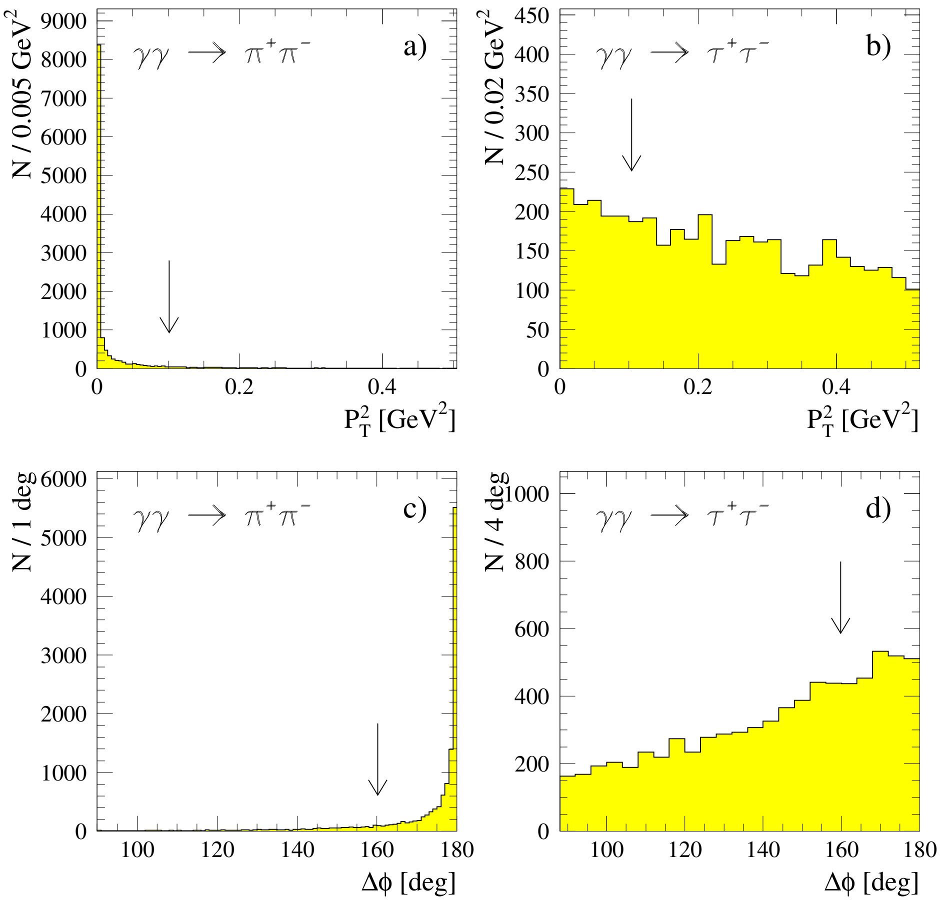

Figure 5.2: Predicted event shape distributions for total transverse momentum squared and angle between the two tracks in the $r\phi$ plane for the production of charged pion (a,c) and taon (b,d) pairs in two-photon interactions. The cuts imposed in the analysis are shown by the arrows. The Vermaseren MC was used to simulate $\gamma\gamma \rightarrow \pi^+\pi^-$ and $\gamma\gamma \rightarrow \tau^+\tau^-$ processes. Note that the bin widths are 4 times wider for $\gamma\gamma \rightarrow \tau^+\tau^-$ distributions.

To ensure that all particles were detected, the total transverse momentum squared of the event was required to be less than 0.1 GeV^2 and the two tracks had to be opposite in the

$r\phi$ plane to within 0.35 rad ($\Delta\phi > 160°$).
The influence of the last two cuts on the $\gamma\gamma \to \pi^+\pi^-$ and $\gamma\gamma \to \tau^+\tau^-$ simulation events is shown in Fig.5.2. The events with two *good* tracks have been selected. For the simulation of the process $\gamma\gamma \to \pi^+\pi^-$ the Vermaseren Monte Carlo was used. The cut on invariant mass, $W_{\gamma\gamma} > 0.8$ GeV was imposed. One of the important backgrounds to the analysis, the process $\gamma\gamma \to \tau^+\tau^-$ was generated without any cuts and the corresponding e^+e^- luminosity for this process was about 10 times bigger than for $\gamma\gamma \to \pi^+\pi^-$. For the simulation of the process $\gamma\gamma \to \tau^+\tau^-$ the Vermaseren Monte Carlo was also used.
From the Fig.5.2 one can see that the cuts used in the analysis (and marked by the arrows on the figure) are very efficient in reducing the background from two-photon tau pairs production and, at the same time, do not introduce a big reduction factor on the signal events.
A plot of the ionisation energy loss normalised to that for minimum ionising particles versus momentum, for events after cuts described above, is shown in Fig.5.3. The electron band is well separated from the pion and muon one, therefore the high $e^+e^- \to e^+e^-e^+e^-$ background can easily be rejected.
The next cut concerns neutral particles: events with energy deposits in the calorimeters not associated with any charged track were rejected. This requirement reduce remaining background from processes with neutral particles and avoids the situation when the event is triggered by a noise in a calorimeter. However, some good events with two charged tracks and noise in the calorimeter are lost. The corresponding correction factor is found by using the calibration process – muon pair production (see section 5.6).
After imposing all cuts described above, the sample was assumed to contain only $e^+e^-e^+e^-$, $e^+e^-\mu^+\mu^-$, $e^+e^-\pi^+\pi^-$, $e^+e^-K^+K^-$ and $e^+e^-p\bar{p}$ final states.
An example of the invariant mass spectrum for two-prong events is shown in Fig.5.4. Pion mass was assumed for all particles. Even without any particle identification, the distinct resonance $f_2(1270)$ signal is seen. For comparison, in Fig.5.5a) the invariant mass of the sum of Monte Carlo for the three dominant processes: $\gamma\gamma \to \pi^+\pi^-$, $\gamma\gamma \to \mu^+\mu^-$ and $\gamma\gamma \to e^+e^-$ is shown. The simulation of the process $\gamma\gamma \to \pi^+\pi^-$ includes production of the resonance $f_2(1270)$ and the point-like continuum. In Fig.5.5b) the invariant mass distribution for the experimental data after two-prong selection is shown in the same histogram binning as in case of the simulation. Monte Carlo was normalised to the luminosity of this data.
As the Monte Carlo events are shown after the detector simulation, these two plots should be very similar. However, the huge discrepancy can be observed. This discrepancy is a reflection of the trigger inefficiency, the simulation of which, unfortunately, is not included in the DELPHI detector simulation program. It will be treated separately using the experimental data.

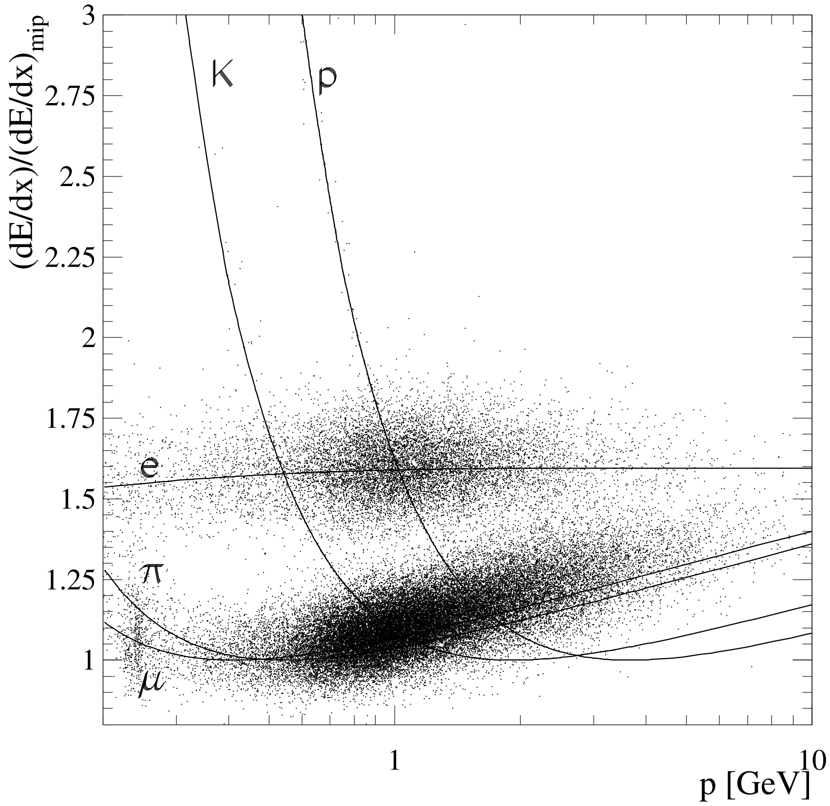

Figure 5.3: Specific ionisation energy loss as a function of particle's momentum from events with two charged tracks in the final state.

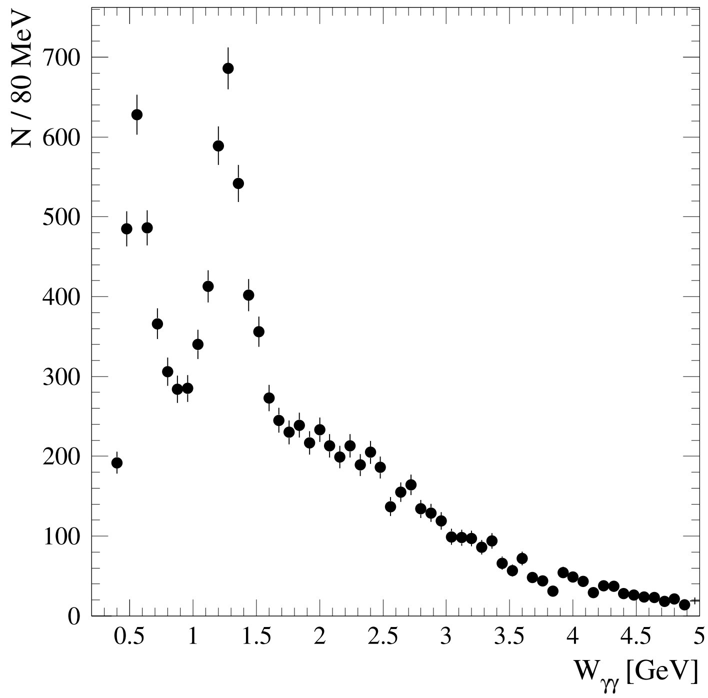

Figure 5.4: Example of invariant mass spectrum of two-prong events, calculated with all tracks considered as pions. Data from the year 1992.

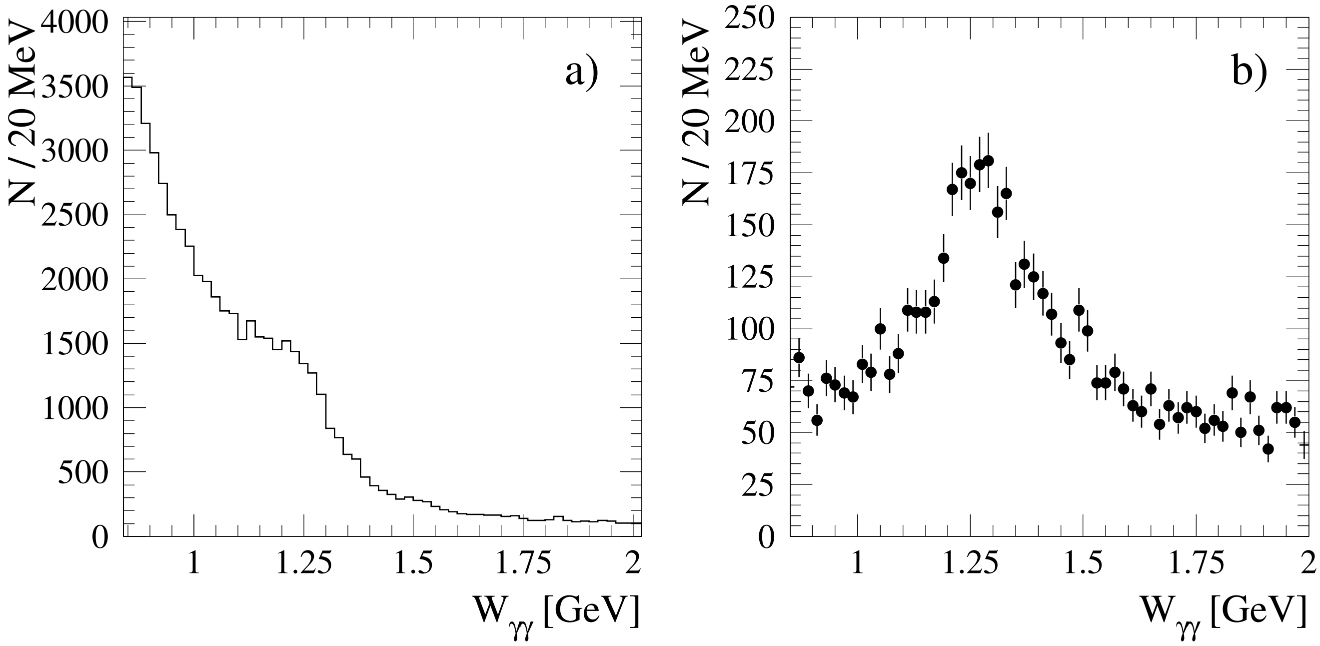

Figure 5.5: Invariant mass distribution for: a) the sum of $\gamma\gamma \to \pi^+\pi^-$, $\gamma\gamma \to \mu^+\mu^-$ and $\gamma\gamma \to e^+e^-$ Monte Carlo after detector simulation; b) data from the year 1992 after two-prong selection. Invariant mass was calculated assuming that all particles are pions. Monte Carlo is normalised to the luminosity of the data.

5.2.2 Polar angle θ^* in the $\gamma\gamma$ centre-of-mass system

If the scattered electron and positron remain undetected, the information about $\gamma\gamma$ system comes mainly from two quantities: an invariant mass of the final state particles and a polar angle θ^* between one of the final state particles (here positive particle was chosen) and the photon direction in the $\gamma\gamma$ centre-of-mass system. However, if electrons are not detected the photon direction is also unknown. As the photons are almost real, one can assume that they are collinear with the electron and positron beams and approximate the $\gamma\gamma$ collision axis by the initial e^+e^- direction. The angle θ^* measured with respect to the beam axis will be further denoted as θ^*_z. The angle θ^* can also be approximated by the angle θ^*_c between one of the final state particles and the flight direction of $\gamma\gamma$ centre-of-mass system. The correlations between generated θ^* and its approximations, θ^*_c and θ^*_z, are shown in Fig.5.6.

For this check, Galuga Monte Carlo for the process $\gamma\gamma \to \pi^+\pi^-$ was used. As it can be seen from Fig.5.6, both angles, θ^*_z and θ^*_c, reproduce well the angle θ^*.

The next step was to check the resolution in $\cos\theta^*_z$ and $\cos\theta^*_c$ i.e. relative differences between measured and generated values. The results are shown in Fig.5.7. The resolution is much better in $\cos\theta^*_z$, therefore in the following the θ^*_z is used as the approximation of θ^* and for simplicity, θ^*_z will be called θ^*.

The influence of detector acceptance on $\cos\theta^*$ distribution is shown in Fig.5.8. At the generator level, the flat $\cos\theta^*$ dependence was assumed. After requirement that two tracks have to be visible within the detector acceptance, one gets the distribution as in Fig.5.8 b).

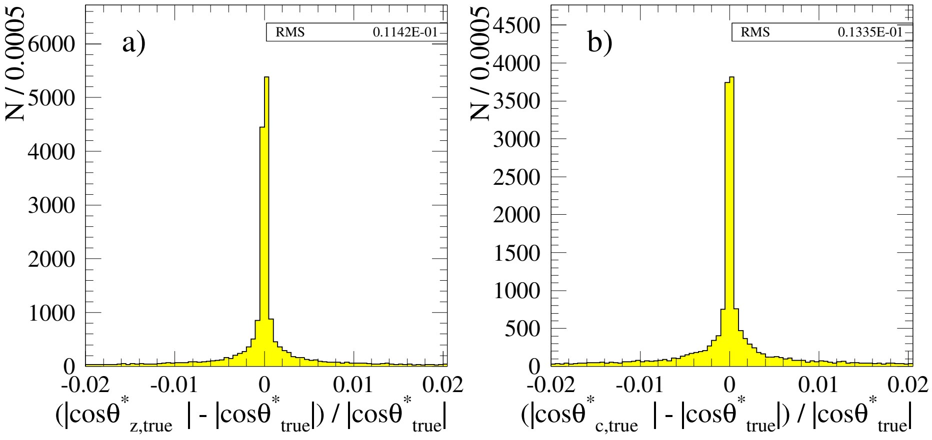

Figure 5.6: Comparison of the $\cos\theta^*$ for two different approximations of the angle θ^* discussed in the text: a) $\theta^*_{z,true}$ and b) $\theta^*_{c,true}$ Generator level of the Galuga Monte Carlo for the process $\gamma\gamma \to \pi^+\pi^-$.

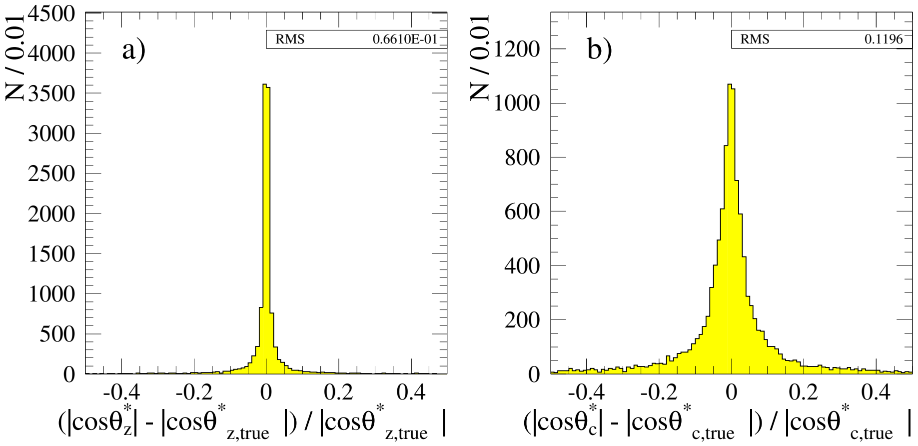

Figure 5.7: Resolution in $\cos\theta^*$. Two different approximations of the angle θ^* discussed in the text have been used: a) θ^*_z and b) θ^*_c. Based on Galuga $\gamma\gamma \to \pi^+\pi^-$ simulation.

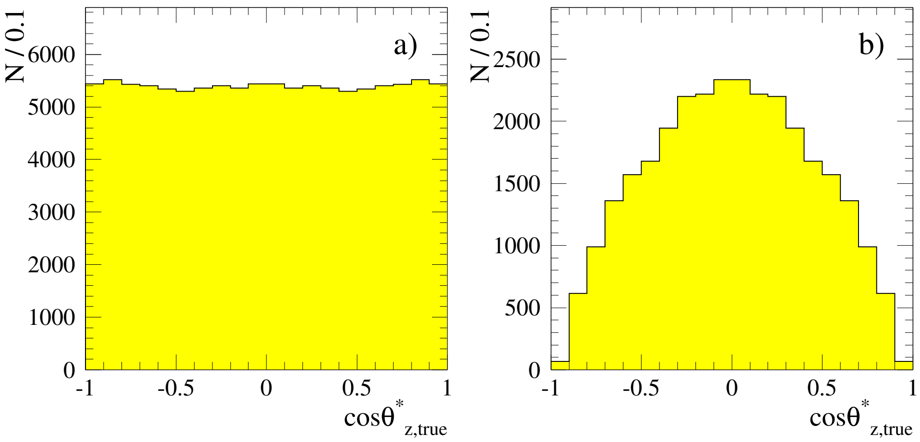

Figure 5.8: Distribution of $\cos\theta^*_z$ at the generator level: a) without any cuts; b) after requirement that the two tracks have to be visible within the detector acceptance.

5.2.3 Particle identification

Identification of kaons and protons is based on the measurement of ionisation energy loss in the TPC and VD and on the measurement of the emission angle of Cherenkov light in the RICH detectors (Figures 3.9,5.3). **Kaons** with momenta below 0.5 GeV can be unambiguously identified by the TPC and VD. These with momenta between 0.7 GeV and 2 GeV - by the liquid RICH. Gas RICH is used to identify kaons with momenta greater than 8 GeV and is not useful in our analysis as particles from two-photon interactions usually have lower momenta.

For evaluation of the kaon identification efficiency, ε_K, the events with at least one particle identified as a good kaon were selected. The quantity ε_K is defined as the number of events with the second particle also identified as a kaon to the number of all events. In case of the experimental data, this method is valid only if the background is small. In the Fig.5.9 the efficiency is presented as a function of kaon momentum and polar angle θ for both data and Galuga Monte Carlo. The obtained agreement is good. Similarly

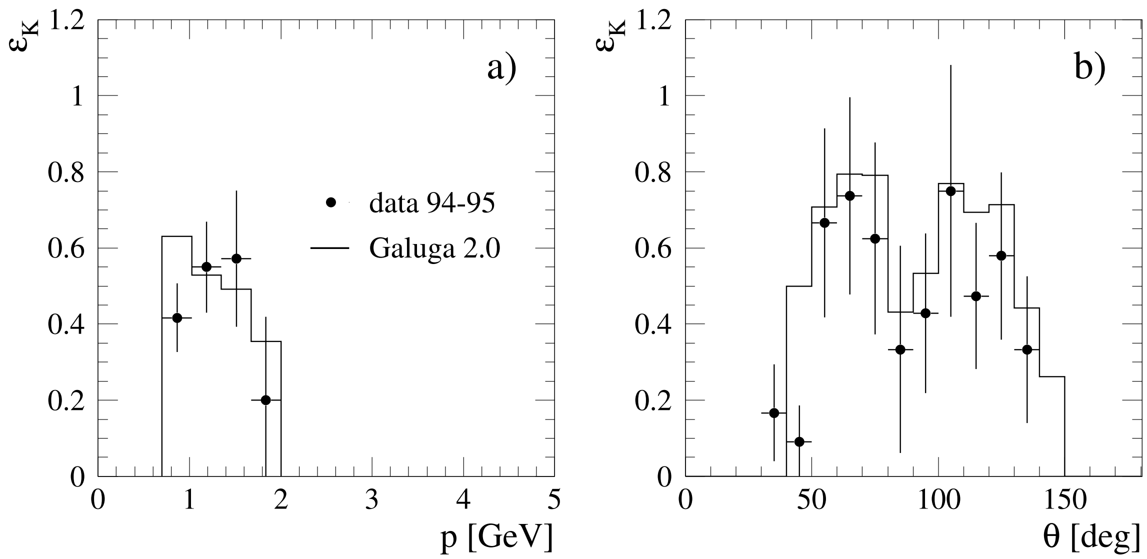

Figure 5.9: Kaon identification efficiency as a function of a) momentum and b) polar angle θ. Data are shown as the solid points, the Monte Carlo simulation (Galuga 2.0) is described by the histogram.

to kaons, **protons** with momenta below 0.9 GeV can be identified by the TPC and VD while protons with momenta between 1.5 GeV and 4 GeV - by the liquid RICH.

Electron identification in the DELPHI experiment is performed mainly using two independent measurements, the measurement of ionisation energy loss (dE/dx) and energy deposition in electromagnetic calorimeters.

A track is identified as a **muon** if it has at least one associated hit in the muon chambers. For evaluation of the muon identification efficiency ε_μ, the events with at least one identified muon were selected. The ε_μ is defined as the number of events with the second particle also identified as a muon by muon chambers to the number of all events. The efficiency is presented as a function of muon momentum and polar angle θ in the Fig.5.10. As for kaons, the obtained agreement between data and Monte Carlo is good, which confirms good understanding of the detector systematics. Muons can be identified with efficiency greater than 50% if they have momenta $\gtrsim 1.8$ GeV.

The muon has a mass very close to the pion mass and the identification methods based

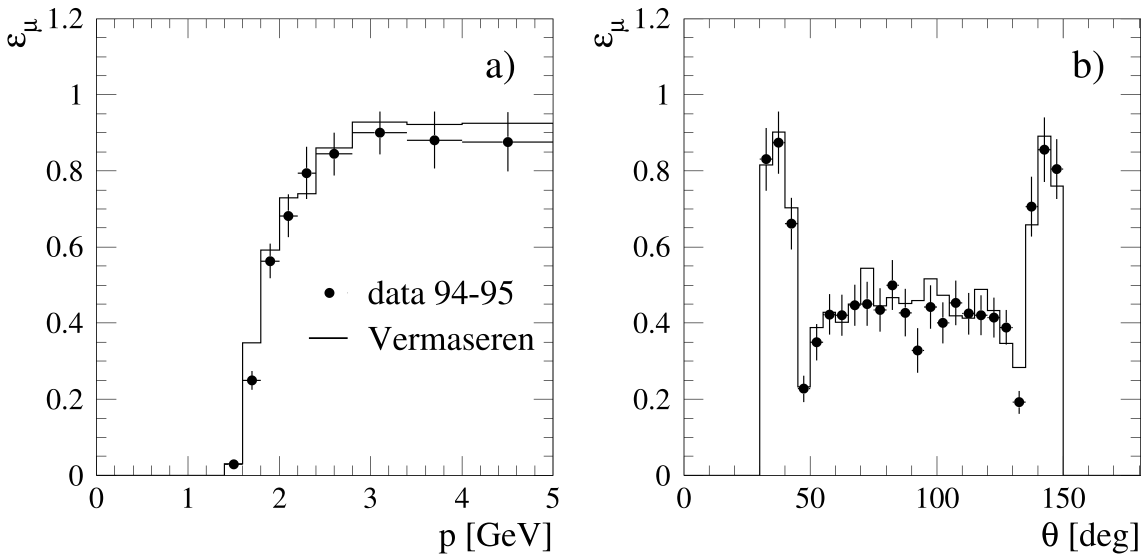

Figure 5.10: Muon identification efficiency as a function of a) momentum and b) polar angle θ. Data are shown as the solid points, the Monte Carlo simulation (Vermaseren) is described by the histogram.

on difference in particle masses cannot be used to distinguish muons from pions.
A particle is identified as a **pion** if it is not classified as kaon, proton, electron or muon. Moreover, all particles with dE/dx close to that of kaons were rejected.
On the basis of the single particle identification, the events have been classified as follows:

- an event was classified as $\mu^+\mu^-$ if at least one of the two particles was identified as a muon,
- an event was accepted as K^+K^- candidate if at least one particle was identified as a good kaon and none of them was identified as muon, electron or proton,
- an event was classified as $\pi^+\pi^-$ if none of the particles were identified as muon, electron, proton or kaon.

Clearly, the kaon sample is characterised by high purity while pion sample is highly contaminated with low-momenta muon pairs.
The particle identification criteria on the basis on TPC dE/dx measurement were specially prepared for this analysis. Some standard DELPHI packages were also used: HADSIGN [30], RIBMEAN [30, 45], MACRIB [46], as well as packages for muon [30, 47] and electron [30, 48] identification.
HADSIGN and RIBMEAN are two packages using information on Cherenkov angle from RICH detectors only, while MACRIB uses neural network technique to identify kaons and protons, with information from TPC, VD and RICH as an input. The invariant mass distributions for $\pi^+\pi^-$ and K^+K^- candidates for data from all considered years separately are shown in Figures 5.11 and 5.12. The year to year changes in the distributions, particularly well seen in the low invariant mass region, are due to the changing in time trigger configurations.

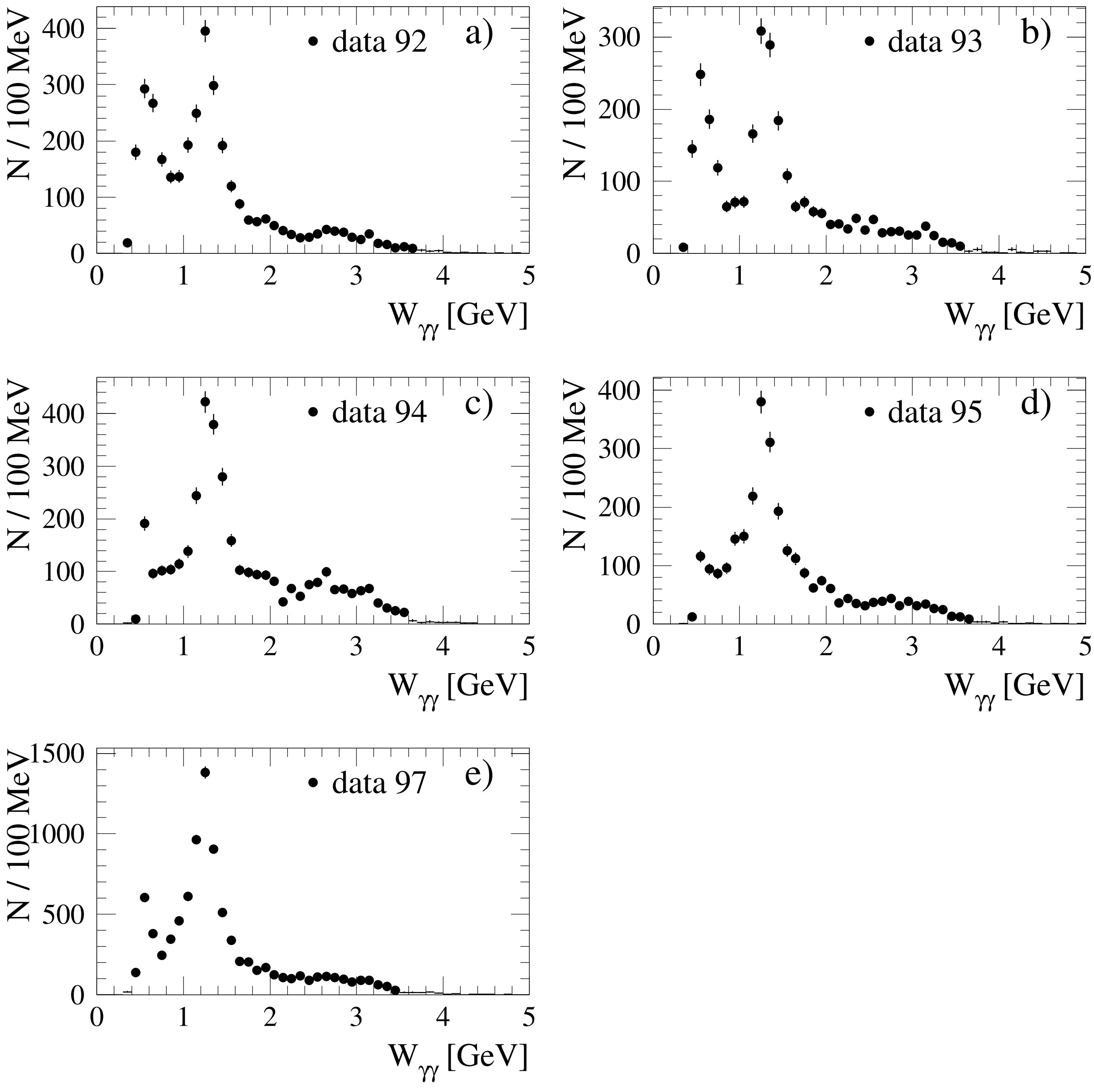

Figure 5.11: Invariant mass spectrum of pion candidates for years: a) 1992, b) 1993, c) 1994, d) 1995 and e) 1997.

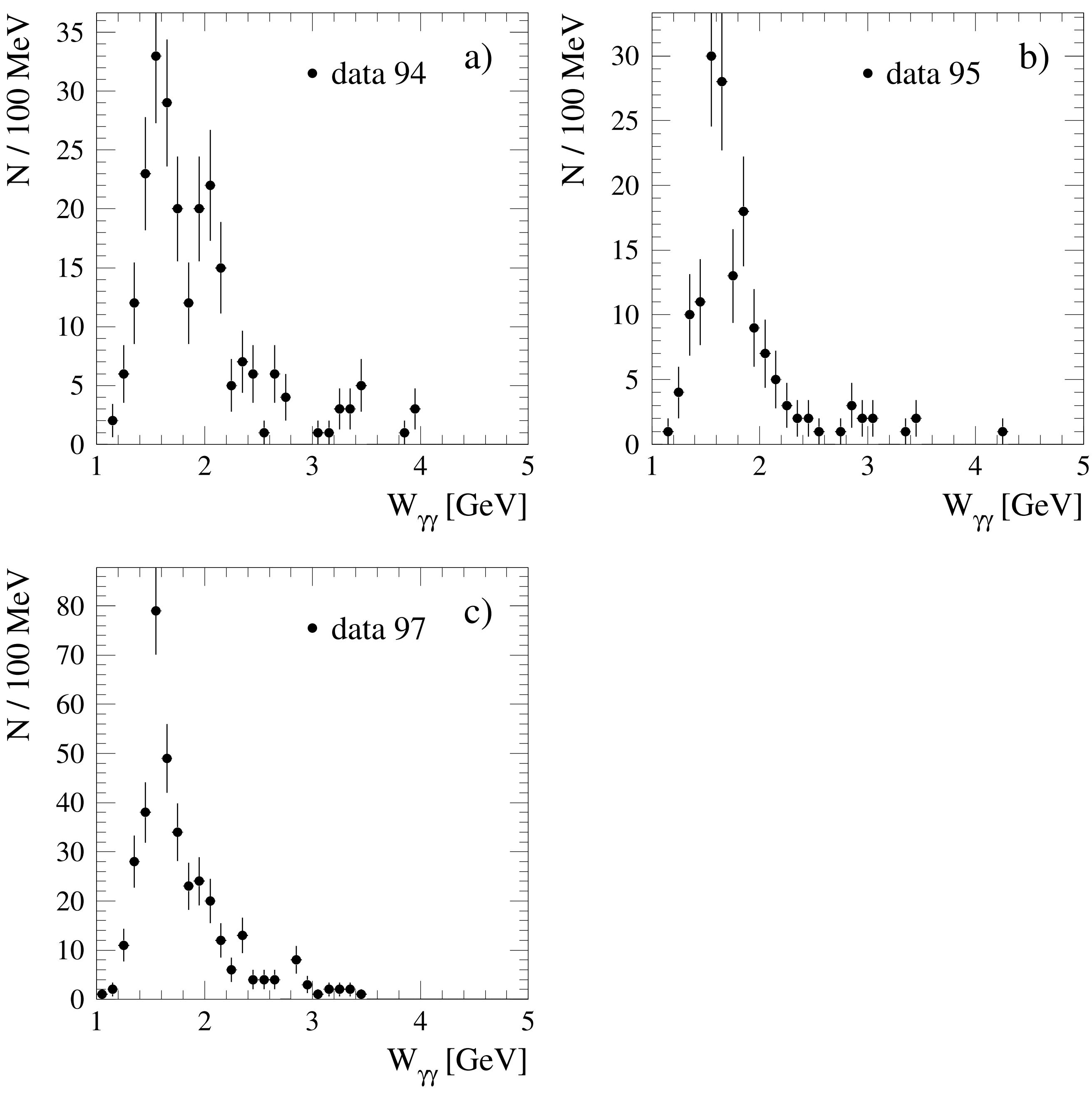

Figure 5.12: Invariant mass spectrum of kaon candidates for years: a) 1992, b) 1993, c) 1994, d) 1995 and e) 1997.

5.3 Trigger efficiency

First selection of the data sample is performed on-line by the trigger system and the events rejected at this level are definitely lost. Proper evaluation of trigger efficiency is crucial for this analysis as the trigger is responsible for a significant reduction of untagged, two-prong data. It is also a challenging task as the simulation of the DELPHI trigger system does not exist and the trigger efficiency can only be extracted from the experimental data. In addition, for most of the time there was not a dedicated trigger for untagged, low p_T and low multiplicity events from photon-photon interactions and two-prong $\gamma\gamma$ events were accepted by different trigger functions in different periods of time.

The method used to estimate the trigger efficiency [49, 33] takes advantage of the fact that in the DELPHI detector the same events can be triggered by independent trigger functions.

If A and B are the two independent groups of trigger functions (TFs) which can fire the trigger system, by N_A and N_B we denote the numbers of events triggered by A and B respectively. N is the total number of events. Then the number of events which were not detected at all equals $N_{nd} = N - (N_A + N_B - N_{AB})$, where N_{AB} denotes the number of events triggered simultaneously by both sets of triggers. Efficiencies of accepting a given kind of events by the trigger groups A and B are given by:

$$\varepsilon_A = \frac{N_A}{N} \qquad \varepsilon_B = \frac{N_B}{N}$$

Triggers A and B are independent, therefore the efficiency of their conjunction is:

$$\varepsilon_{AB} = \varepsilon_A \cdot \varepsilon_B = \frac{N_{AB}}{N}$$

From the above formulas one can find:

$$N = \frac{N_A N_B}{N_{AB}}$$

Total efficiency of both trigger sets can thus be estimated as:

$$\varepsilon_t = \varepsilon_A + \varepsilon_B - \varepsilon_A \varepsilon_B = \frac{N_{AB}}{N_B} + \frac{N_{AB}}{N_B} - \frac{N_{AB}^2}{N_A N_B}$$

The method of estimating errors on the trigger efficiency is presented in Appendix D.

Usually the best possibility was to choose the TPC trigger functions as A and composition of functions from ID, OD, HCAL and TOF as group B. The number of events selected in one of the data samples by the A, B and by both A and B trigger functions as well as obtained efficiencies ε_A, ε_B and total trigger efficiency are shown in Fig.5.13. All distributions are shown as a function of $W_{\gamma\gamma}$ invariant mass. The fitted curve has a standard form:

$$\varepsilon_t = \frac{\mathcal{A}}{1 + \mathcal{B} e^{-\mathcal{C} W_{\gamma\gamma}}}$$

In the calculation of the invariant mass, the pion mass was assumed for all particles. The trigger functions which compose here the A and B groups are following:

- **set A**
  - **CT_MJ1** - TPC contiguity trigger - single track trigger which uses TPC pad information as input to a sophisticated track-finding logic algorithm. It covers the angular range of 29° to 151° in θ.
  - **TPCBB** - Forward-Backward TPC coincidence. These TPC trigger uses only signals from the tracks passing through the endcap wire planes and covers the angular region of 20° to 43° in θ and 137° to 160° in θ.
- **set B**
  - **OD2TOF** - Outer Detector in coincidence with TOF
  - **DF13_I*ID_MJ1** - decision function from the first level (Hadron Forward or Hadron Backward) in coincidence with Inner Detector
  - **DF12_I*ID_MJ1** - decision function from the first level (Hadron Barrel) in coincidence with Inner Detector
  - **TOF_MJ1*(HAFWBWMULO+HABLBBMULO** - TOF in coincidence with trigger from Hadron Calorimeter. HAFWBWMULO stands for Forward-Backward coincidence with energy above 0.5 GeV, HABLBBMULO is back-to-back coincidence with the same energy threshold.

The more detailed description of relations between trigger functions can be found in Appendix C and in [31]. It was always checked, if the decision functions (DF) to which the trigger functions from groups A and B belong, was not masked or prescaled (see section 3.3.5).
The trigger functions from groups A and B must be sensitive to the given type of particles, in our case kaons, pions or muons, and have to operate in the same kinematical, θ, p and p_T, range. In this analysis, the presence of HCAL trigger functions require particles to have momenta and transverse momenta high enough to reach the Hadron Calorimeter. As it was already mentioned, the most effective and most important function - TPC contiguity trigger covers the angular region of 29° to 151° in θ. Thus, the following cuts were imposed:

- momentum $p > 0.7$ GeV,
- transverse momentum $p_T > 0.6$ GeV,
- polar angle $\theta \in (30°,150°)$.

The additional complication is due to the fact that trigger decision in DELPHI is taken at four levels.
Following [33], the first level trigger efficiency was assumed to be 100%. The third level trigger, fortunately follows the logic of the second level trigger. Therefore, the trigger groups (A, B) are constructed as a conjunction of corresponding trigger functions from T2 and T3. The forth level trigger is the software trigger with simple cuts which can be imposed on the Monte Carlo. It was not always used as a trigger - for certain periods of time it only tagged the interesting events. In particular, for the first half of 1997 T4 was used to tag events and starting from the middle of September - also to reject them.
However, after above requirements on the momentum and transverse momentum of the

final state particles, the influence of the fourth level trigger is unseen on the final data samples (see Figs. 5.14c), 5.25c), 5.24b) in sections describing the final data sets).

Therefore the existence of the fourth level trigger was neglected.

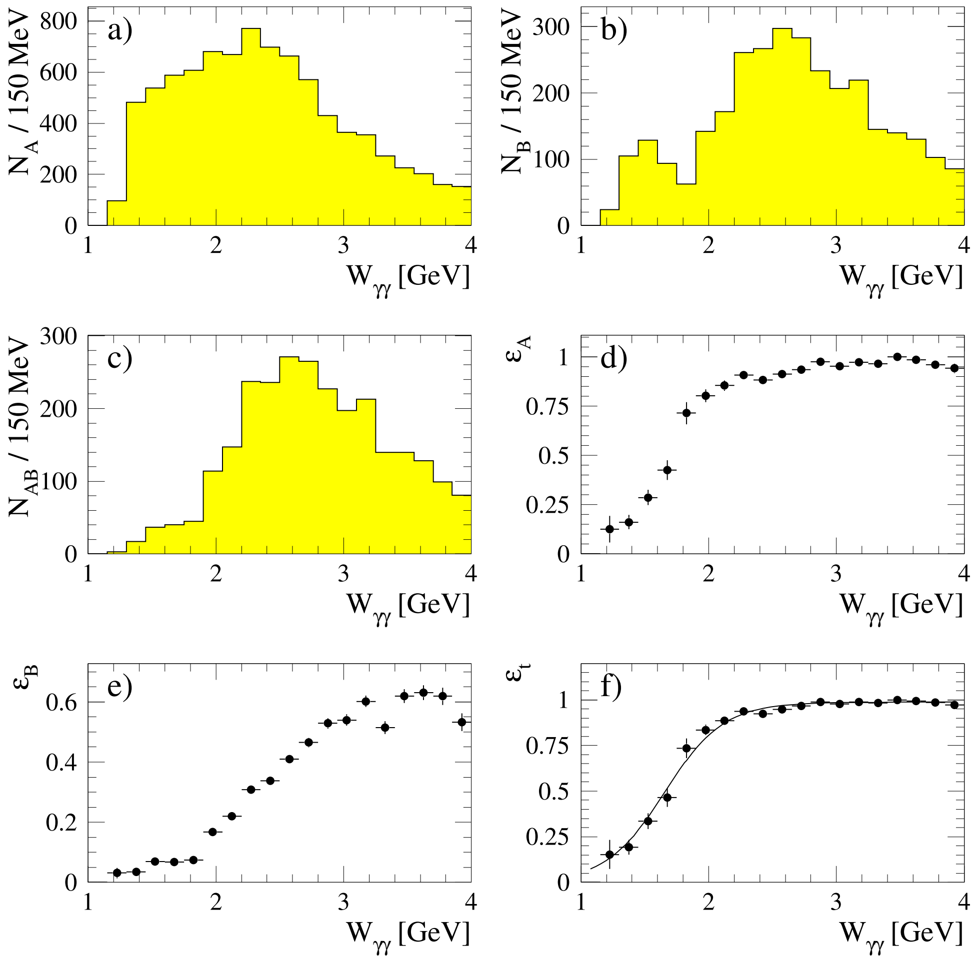

Figure 5.13: Distributions of: a) the number of events accepted by group A of trigger functions; b) the number of events accepted by group B of trigger functions; c) the number of events accepted by both: set A and set B; d) trigger efficiency for group A; e) trigger efficiency for group B; f) total trigger efficiency as a function of invariant mass. Group A consists of two TPC trigger functions and group B is the composition of trigger functions from ID, OD, HCAL and TOF. Data from the years 1994-1995.

5.4 Luminosity e^+e^-

The integrated luminosity $\mathcal{L}$ (for definition of the luminosity see section 2.3.2) for a given period of time is usually calculated as:

$$\mathcal{L} = \int L dt = \frac{N}{\sigma}$$

where$N$ is the number of selected events for any process with a visible cross-section σ. Such a reaction should be characterised by simple experimental signature, large cross-section and have to be calculated theoretically with high precision. The process chosen at

LEP is $e^+e^- \to e^+e^-$ Bhabha scattering at small angles, which proceeds predominantly through the exchange of a photon in the t-channel [50, 51, 29]. In DELPHI, before 1994 the luminosity was measured mainly using the SAT detector with angular acceptance between 43 and 135 mrad in θ. After 1993, the STIC (see section 3.2.2) calorimeter which covers wider angular region between 29 and 185 mrad has been used.
The calculation of the accepted cross-section is based on the Monte Carlo program BHLUMI, which has a theoretical accuracy of 0.11% at LEP1 and 0.25% at LEP2 energies.

The values of the integrated luminosity for successive runs were taken from the standard DELPHI luminosity files. Runs with not known luminosity were rejected. Additionally, for each year only the runs with stable trigger conditions and good performance level from detectors used in the analysis were selected.
The amount of data rejected from the initial data sample depends on the considered final state.

- In case of $\pi^+\pi^-$ and $\mu^+\mu^-$ selection, data were accepted only if:
  - tracking detectors (TPC,OD,ID) data taking efficiency was > 95%,
  - hadronic calorimeter efficiency > 95%,
  - HPC efficiency > 90%,
  - muon chambers efficiency > 95%.

  The condition concerning barrel muon chambers is responsible for the biggest reduction of the data. The good performance level from the muon chambers is however necessary to properly check the data-Monte Carlo agreement in case of muon pair production as well as to properly estimate the dominating muon background to the process $\gamma\gamma \to \pi^+\pi^-$.

- The charged kaon pair selection does not require good performance of muon chambers, so that the luminosity is fortunately not significantly reduced. The quality requirements are:
  - tracking detectors (TPC,OD,ID) data taking efficiency was > 95%,
  - Hadronic calorimeter efficiency > 95%,
  - HPC efficiency > 90%,
  - RICH efficiency > 90%.

  For kaon studies, the data collected before 1994 were not taking into account because RICH detectors started to be fully operational just in 1994.

The good performance level from the TPC, HCAL, OD and ID is fundamental not only because these detectors are used for event reconstruction, but also because they are used to estimate the trigger efficiency (see section 5.3).
The reduction of initial data samples is significant, but the imposed selection guarantees satisfactionary stable conditions of the trigger and allows to use the trigger efficiency as this efficiency was estimated under the condition that certain detectors were operational. The integrated luminosities after successive cuts, for $\pi^+\pi^-/\mu^+\mu^-$ and K^+K^- data samples, for different years are shown in Table 5.1.

<table>
<tr><td>Period of
data taking</td><td colspan="2">Integrated luminosity $\mathcal{L}[pb^{-1}]$ ± (stat.) ± (syst.)</td></tr>
<tr><td></td><td>K^+K^- sample</td><td>$\pi^+\pi^-/\mu^+\mu^-$ sample</td></tr>
<tr><td>1992</td><td>—</td><td>$23.99 \pm 0.03 \pm 0.03$</td></tr>
<tr><td>stable trig. conditions</td><td>—</td><td>$23.27 \pm 0.03 \pm 0.03$</td></tr>
<tr><td>TPC,OD,HCAL,HPC sel.</td><td>—</td><td>$21.75 \pm 0.03 \pm 0.03$</td></tr>
<tr><td>MUB,MUF selection</td><td>—</td><td>$13.85 \pm 0.02 \pm 0.02$</td></tr>
<tr><td>Final selection</td><td>—</td><td>$\mathbf{13.85 \pm 0.02 \pm 0.02}$</td></tr>
<tr><td>1993</td><td>—</td><td>$36.07 \pm 0.04 \pm 0.05$</td></tr>
<tr><td>stable trig. conditions</td><td>—</td><td>$36.07 \pm 0.04 \pm 0.05$</td></tr>
<tr><td>TPC,OD,HCAL,HPC sel.</td><td>—</td><td>$27.82 \pm 0.03 \pm 0.04$</td></tr>
<tr><td>MUB,MUF selection</td><td>—</td><td>$9.539 \pm 0.019 \pm 0.014$</td></tr>
<tr><td>Final selection</td><td>—</td><td>$\mathbf{9.539 \pm 0.019 \pm 0.014}$</td></tr>
<tr><td>1994</td><td colspan="2">$46.11 \pm 0.03 \pm 0.07$</td></tr>
<tr><td>stable trig. conditions</td><td colspan="2">$46.11 \pm 0.03 \pm 0.07$</td></tr>
<tr><td>TPC,ID,OD,HCAL,HPC sel.</td><td colspan="2">$40.45 \pm 0.03 \pm 0.06$</td></tr>
<tr><td>MUB,MUF selection</td><td></td><td>$28.46 \pm 0.03 \pm 0.04$</td></tr>
<tr><td>RICH selection</td><td>$39.66 \pm 0.03 \pm 0.06$</td><td></td></tr>
<tr><td>Final selection</td><td>$\mathbf{39.66 \pm 0.03 \pm 0.06}$</td><td>$\mathbf{28.46 \pm 0.03 \pm 0.04}$</td></tr>
<tr><td>1995</td><td colspan="2">$31.60 \pm 0.02 \pm 0.05$</td></tr>
<tr><td>stable trig. conditions</td><td colspan="2">$31.60 \pm 0.02 \pm 0.05$</td></tr>
<tr><td>TPC,ID,OD,HCAL,HPC sel.</td><td colspan="2">$29.83 \pm 0.02 \pm 0.04$</td></tr>
<tr><td>MUB,MUF selection</td><td></td><td>$7.773 \pm 0.012 \pm 0.011$</td></tr>
<tr><td>RICH selection</td><td>$28.19 \pm 0.02 \pm 0.04$</td><td></td></tr>
<tr><td>Final selection</td><td>$\mathbf{28.19 \pm 0.02 \pm 0.04}$</td><td>$\mathbf{7.773 \pm 0.012 \pm 0.011}$</td></tr>
<tr><td>1997</td><td colspan="2">$53.39 \pm 0.09 \pm 0.55$</td></tr>
<tr><td>stable trig. conditions</td><td colspan="2">$41.43 \pm 0.08 \pm 0.43$</td></tr>
<tr><td>TPC,ID,OD,HCAL,HPC sel.</td><td colspan="2">$36.93 \pm 0.07 \pm 0.38$</td></tr>
<tr><td>MUB,MUF selection</td><td></td><td>$10.76 \pm 0.04 \pm 0.11$</td></tr>
<tr><td>RICH selection</td><td>$33.90 \pm 0.07 \pm 0.35$</td><td></td></tr>
<tr><td>Final selection</td><td>$\mathbf{33.90 \pm 0.07 \pm 0.35}$</td><td>$\mathbf{10.76 \pm 0.04 \pm 0.11}$</td></tr>
</table>

Table 5.1: Integrated luminosities for $\pi^+\pi^-/\mu^+\mu^-$ and K^+K^- data samples. The first line for each year represents the maximal available luminosity. The last line shows the integrated luminosities used in this analysis.

5.5 Muon pair production

The process $e^+e^- \to e^+e^-\mu^+\mu^-$ is theoretically well understood and the cross-section is calculated to high precision within QED. As it has the characteristics similar to the studied here $e^+e^- \to e^+e^-K^+K^-$ and $e^+e^- \to e^+e^-\pi^+\pi^-$ interactions, it was used to check the main steps of the analysis, our understanding of trigger and detector efficiencies and quality of the experimental data description by the detector simulation program for low-multiplicity events with low-momenta tracks. The modeling used at the generator level and accuracy of the Equivalent Photon Approximation was checked. Also the correction factor due to existence of noise in the calorimeters was found.
The muon-pair candidates, in addition to the two-prong selection cuts should satisfy the following criteria:

- at least one muon must be identified by muon chambers,
- θ of both tracks $\in$ (30°,150°),

- momenta greater than 2 GeV and transverse momenta greater than 1 GeV,
- $|\cos\theta^*| < 0.8$,
- total transverse momentum squared $P_T^2 < 0.05\mathrm{GeV}^2$.

After cuts which ensure exclusivity of the event and define the muon sample, we assume that all low-energy neutral showers accompanying two charged tracks are calorimeters' noise. Therefore events with neutral showers of energy less than 1.5 GeV are not rejected. To demonstrate the uniformity in time of the data selection procedure, the number of $\mu^+\mu^-$ events per unit luminosity was calculated as a function of accumulated luminosity for all data samples (Fig.5.14). Different rates of accepted events for subsequent data samples result from the different detector acceptance and trigger efficiencies. The Fig.5.14 proves also that data were grouped correctly, as the number of accepted events is constant within whole data samples. In Figs. 5.15-5.20 the comparison between data and

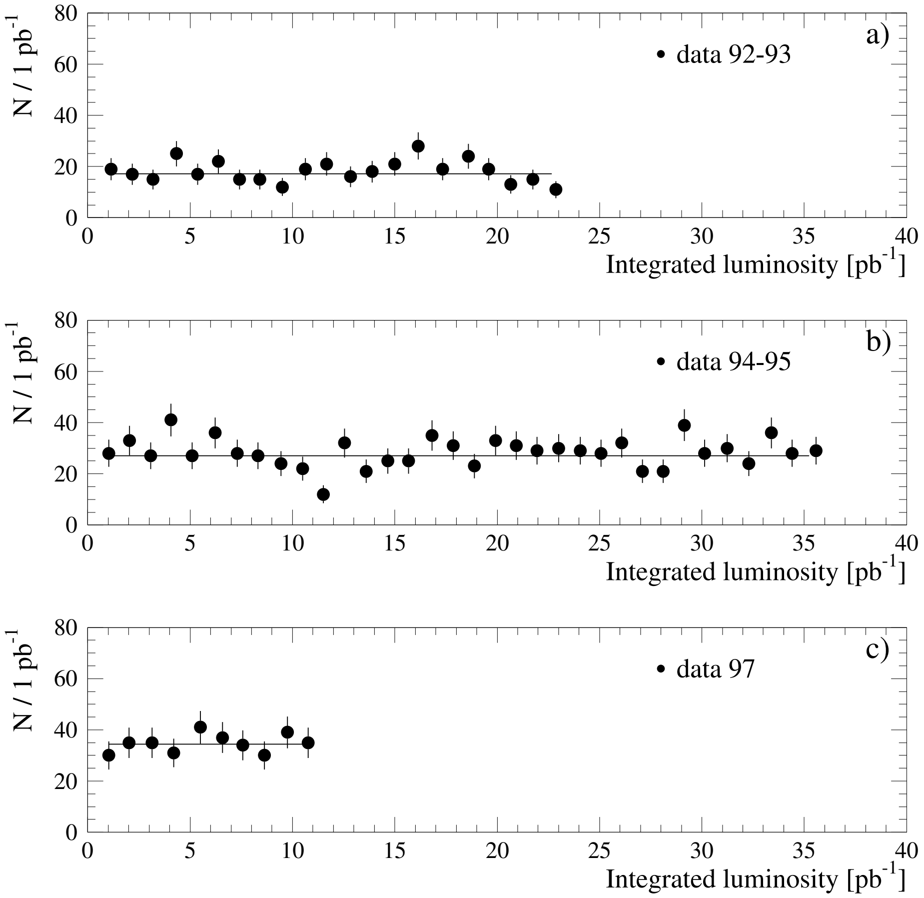

Figure 5.14: Number of accepted muon events per $1pb^{-1}$ of collected luminosity as a function of accumulated luminosity for all data samples. The horizontal lines represent fits to the data points.

Vermaseren Monte Carlo is shown for the years 1992-1993, 1994-1995 and 1997. The distributions of invariant mass, total transverse momentum squared, $\cos\theta^*$ and angle between the two tracks in the $r\phi$ plane as well as momentum, transverse momentum, polar angle and impact parameter in z of the tracks are presented. Data were corrected for the trigger efficiency, however trigger efficiency exceeds everywhere 95%. All Monte

Carlo distributions have been normalised to the luminosity of the data. The integrated luminosities of the generated Monte Carlo samples are about two times bigger than the corresponding luminosities of the experimental data.
The same distributions are shown for all data groups, to demonstrate that detector and trigger is well understood in all periods of time. The absolute normalisation without any arbitrary normalisation factor has been achieved. Data - Monte Carlo agreement for all years is satisfactory. Background from the processes $e^+e^- \to e^+e^-\tau^+\tau^-$, $e^+e^- \to e^+e^-e^+e^-$, $e^+e^- \to e^+e^-\pi^+\pi^-$ and $e^+e^- \to e^+e^-K^+K^-$ was found to be negligible.

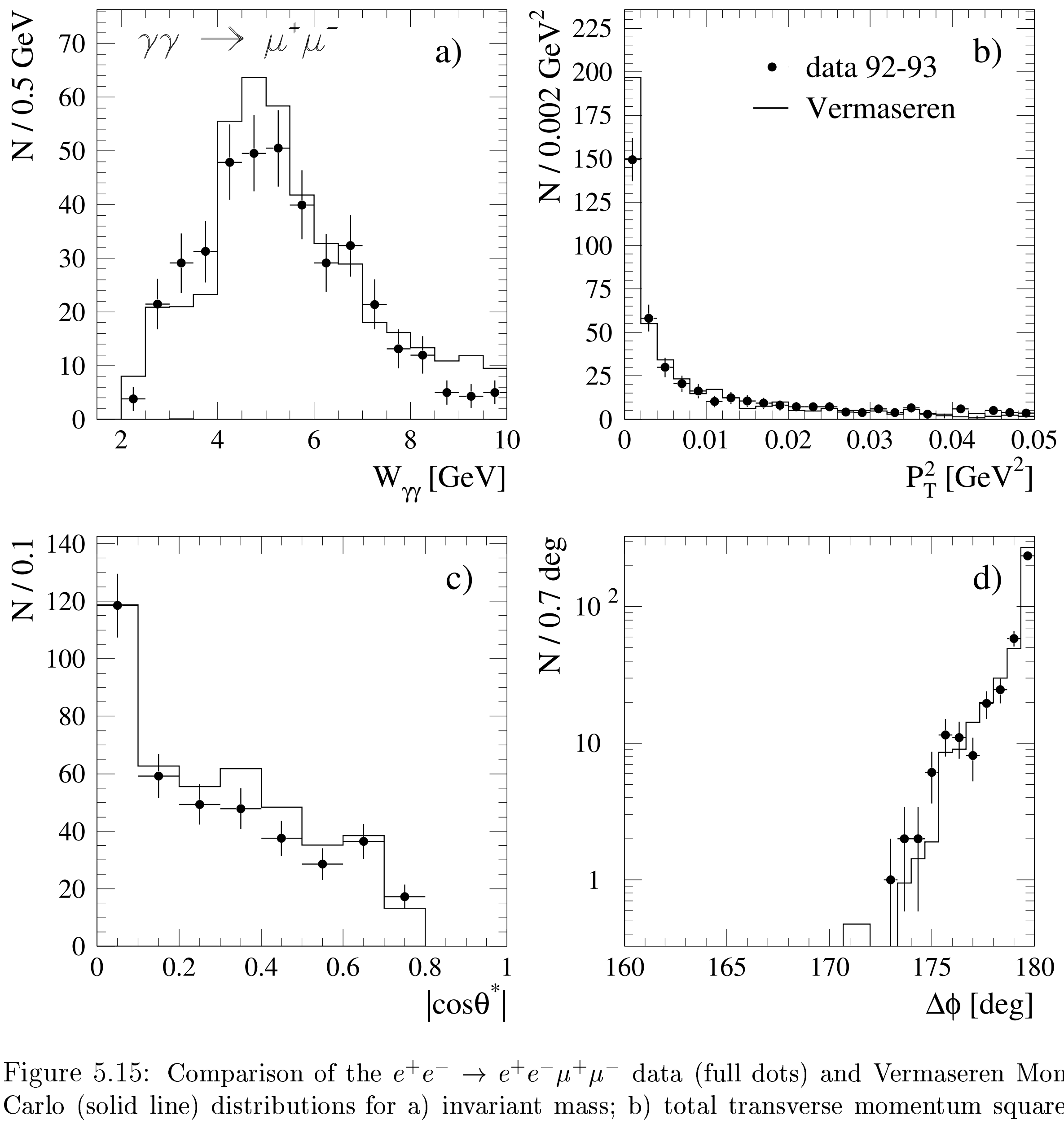

Figure 5.15: Comparison of the $e^+e^- \to e^+e^-\mu^+\mu^-$ data (full dots) and Vermaseren Monte Carlo (solid line) distributions for a) invariant mass; b) total transverse momentum squared; c) $\cos\theta^*$ (with cut $|\cos\theta^*| < 0.8$); d) angle between the tracks in the $r\phi$ plane. Monte Carlo distributions have been normalised to the luminosity of the data. Data from the years 1992-1993, $\sqrt{s} = 91$ GeV.

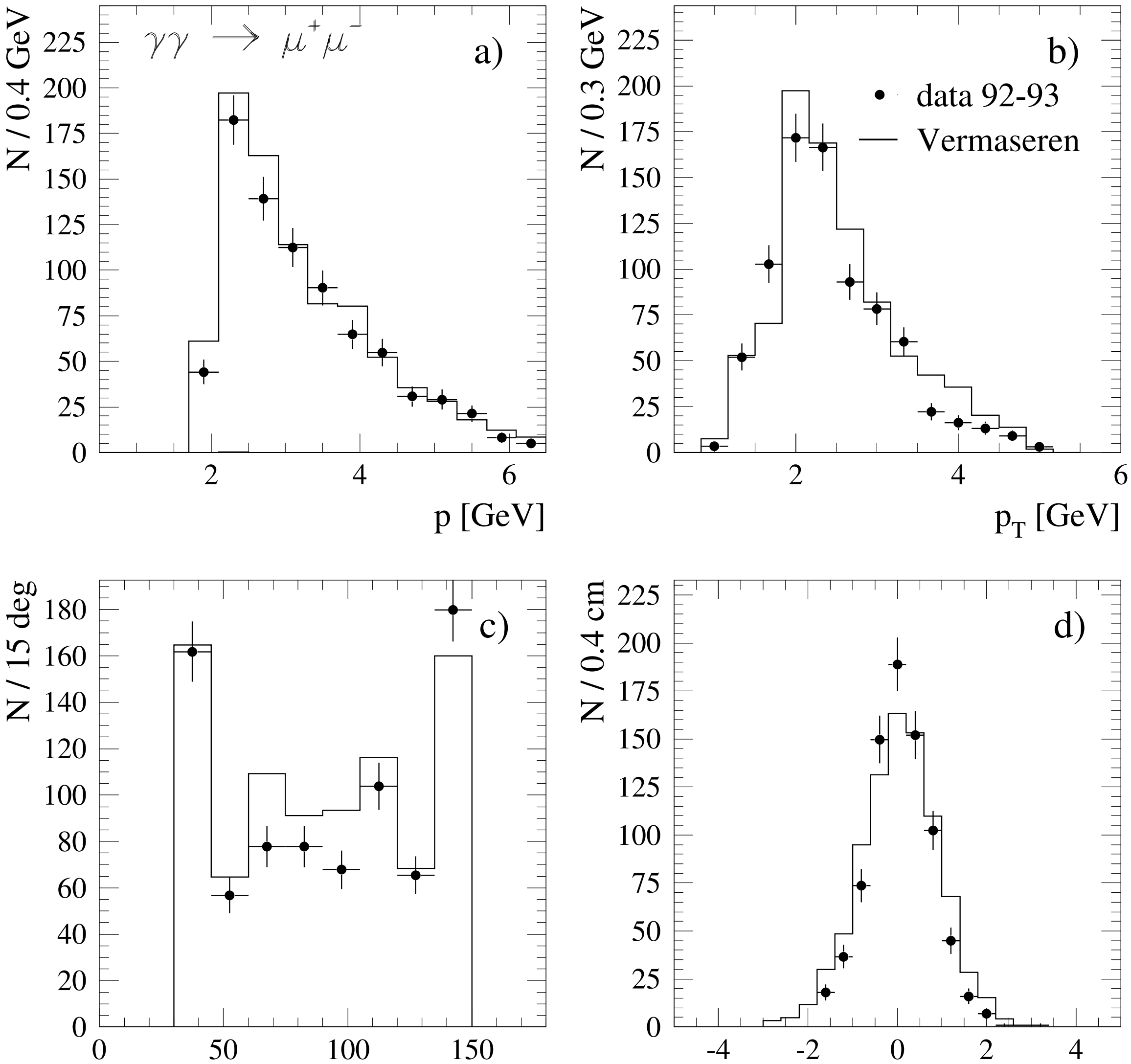

Figure 5.16: Comparison between data (full dots) and Vermaseren Monte Carlo (solid line) for a) momentum p, b) transverse momentum p_T, c) polar angle θ and d) impact parameter in z of the muon. Monte Carlo distributions have been normalised to the luminosity of the data. Data from the years 1992-1993, $\sqrt{s} = 91$ GeV.

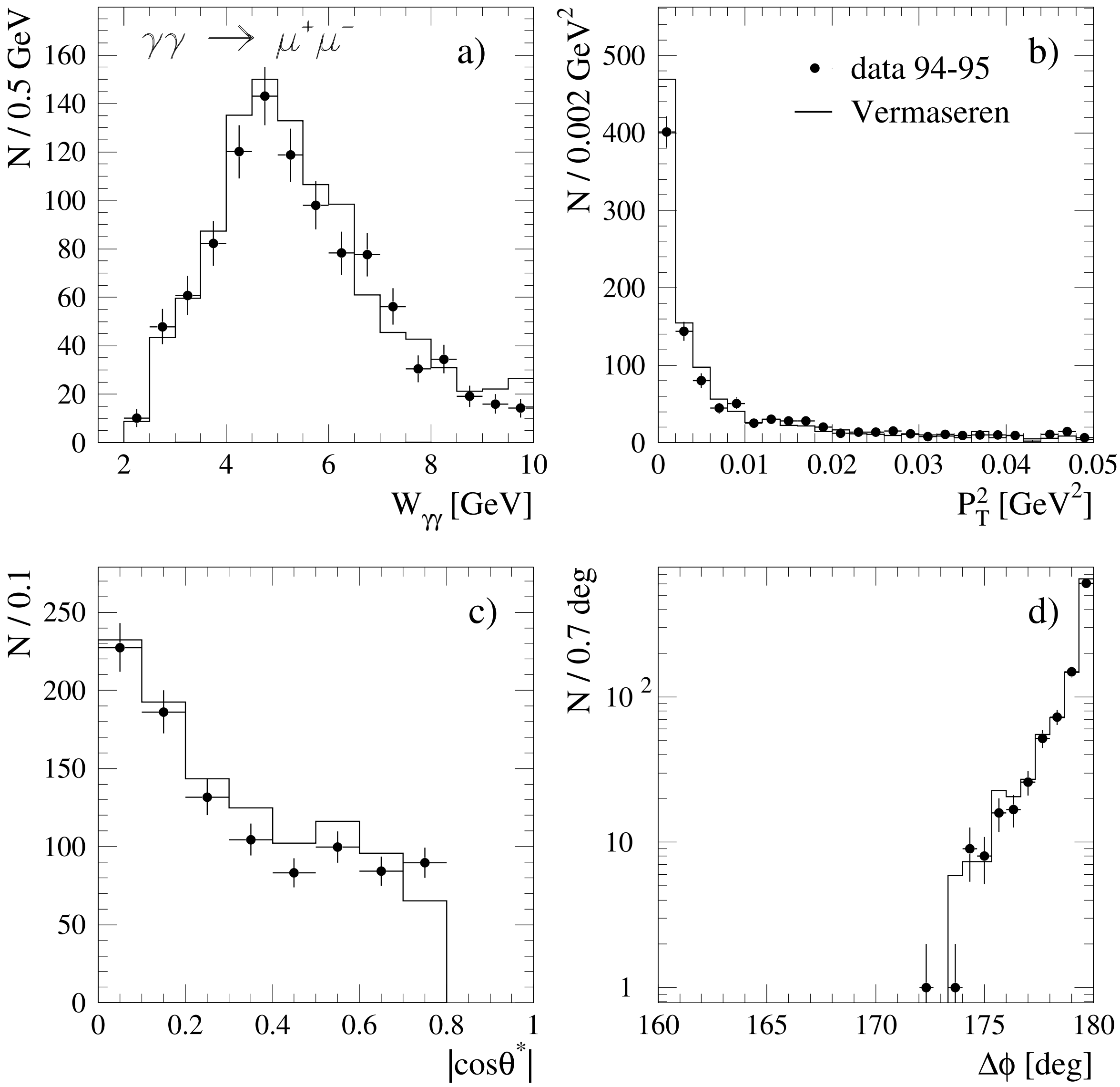

Figure 5.17: Comparison of the $e^+e^- \rightarrow e^+e^-\mu^+\mu^-$ data (full dots) and Vermaseren Monte Carlo (solid line) distributions for a) invariant mass; b) total transverse momentum squared; c) $\cos\theta^*$ (with cut $|\cos\theta^*| < 0.8$); d) angle between the tracks in the $r\phi$ plane. Monte Carlo distributions have been normalised to the luminosity of the data. Data from the years 1994-1995, $\sqrt{s} = 91$ GeV.

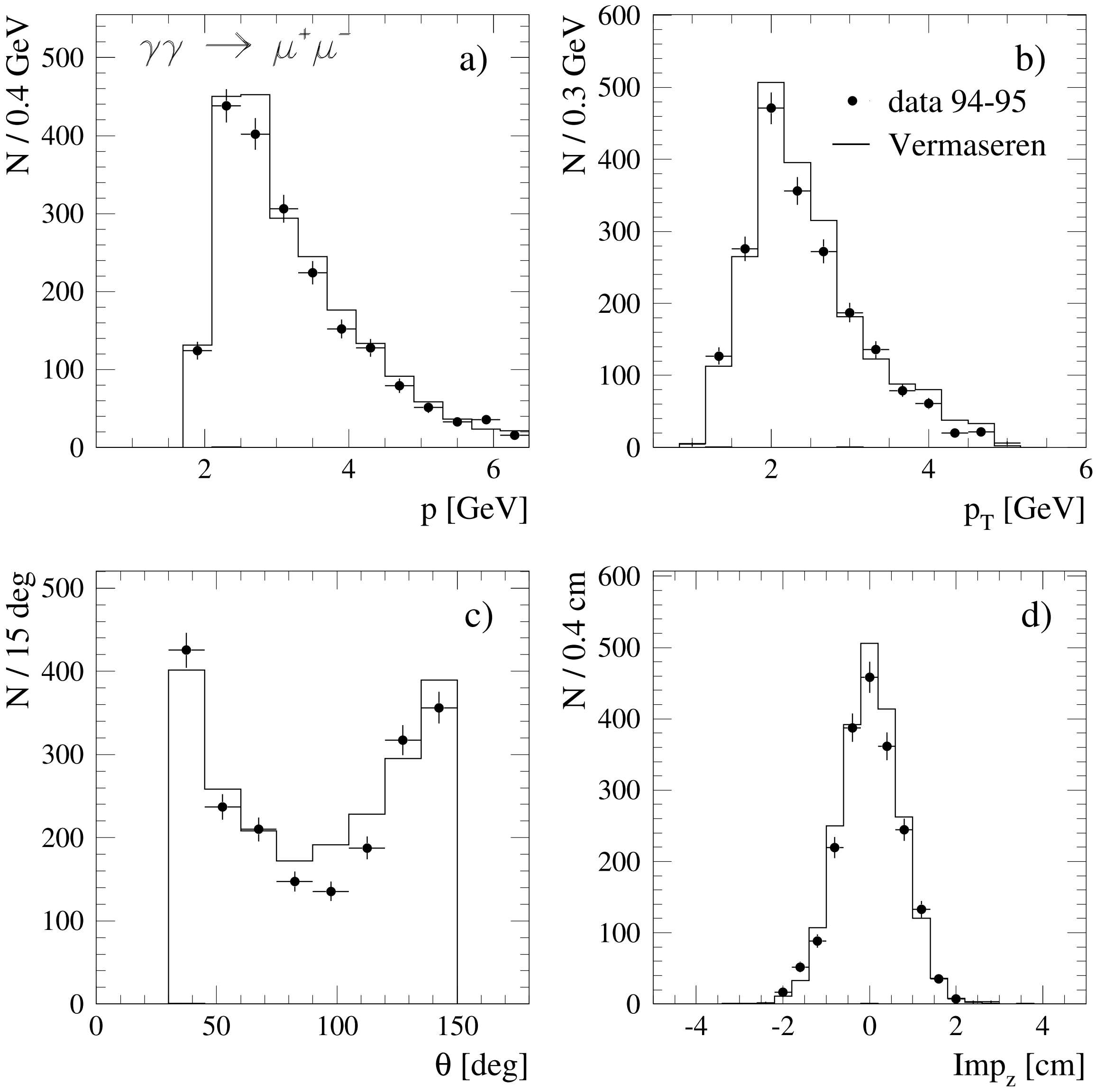

Figure 5.18: Comparison between data (full dots) and Vermaseren Monte Carlo (solid line) for a) momentum p, b) transverse momentum p_T, c) polar angle θ and d) impact parameter in z of the muon. Monte Carlo distributions have been normalised to the luminosity of the data. Data from the years 1994-1995, $\sqrt{s} = 91$ GeV.

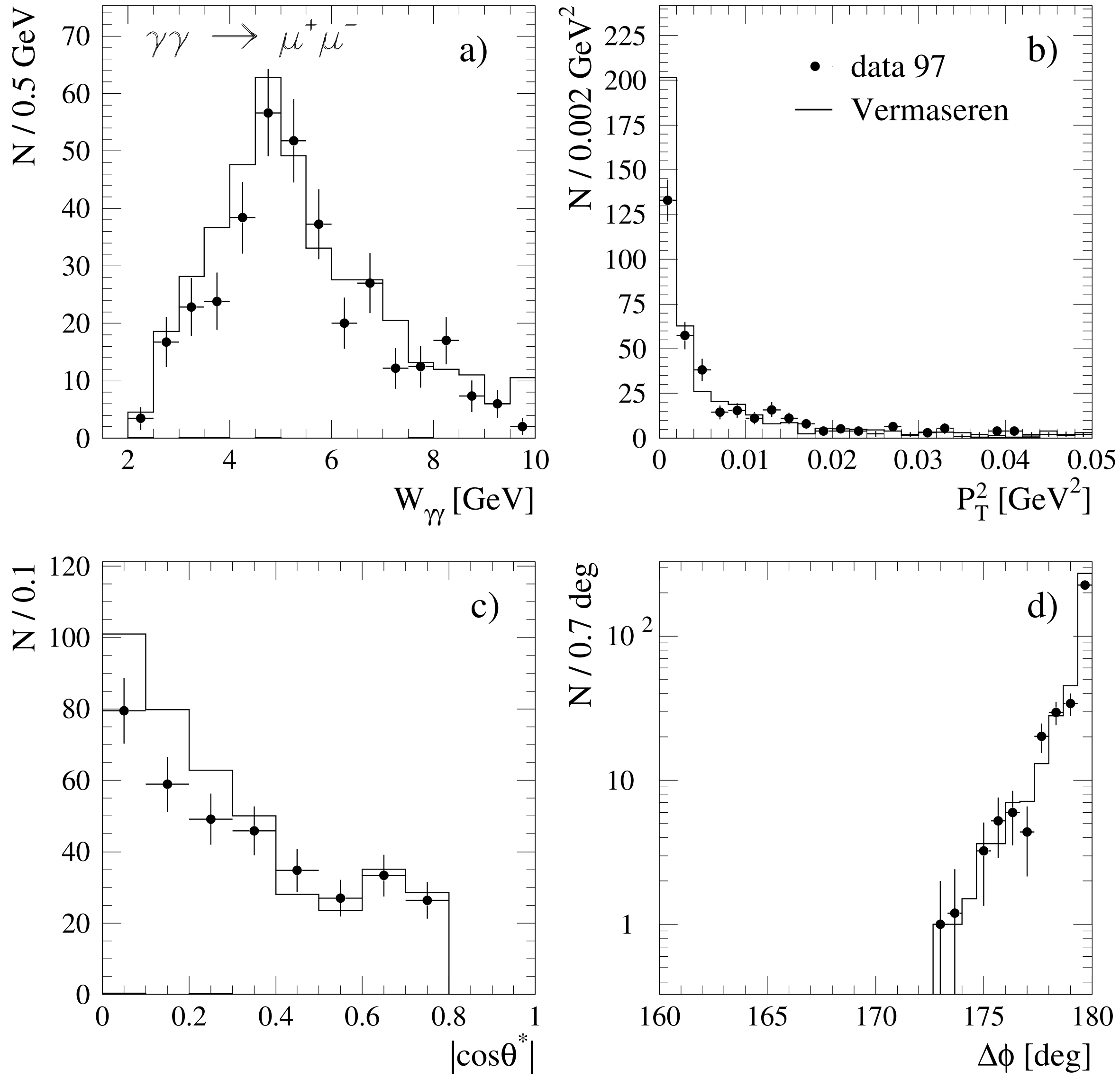

Figure 5.19: Comparison of the $e^+e^- \rightarrow e^+e^-\mu^+\mu^-$ data (full dots) and Vermaseren Monte Carlo (solid line) distributions for a) invariant mass; b) total transverse momentum squared; c) $\cos\theta^*$ (with cut $|\cos\theta^*| < 0.8$); d) angle between the tracks in the $r\phi$ plane. Monte Carlo distributions have been normalised to the luminosity of the data. Data from the year 1997, $\sqrt{s}$ = 183 GeV.

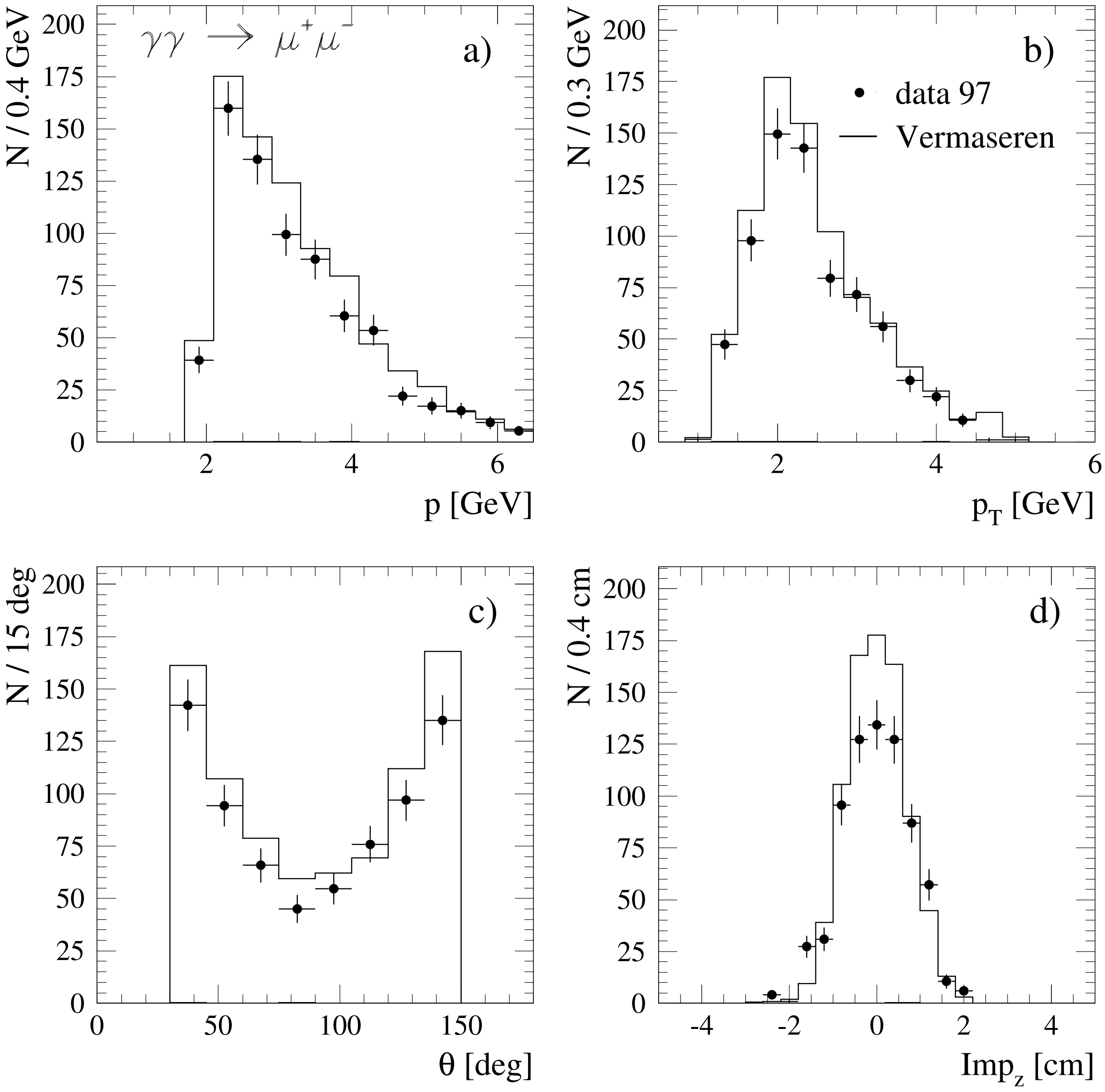

Figure 5.20: Comparison between data (full dots) and Vermaseren Monte Carlo (solid line) for a) momentum p, b) transverse momentum p_T, c) polar angle θ and d) impact parameter in z of the muon. Monte Carlo distributions have been normalised to the luminosity of the data. Data from the year 1997, $\sqrt{s} = 183$ GeV.

5.6 Kaon and pion pair production

The kaon and pion candidates, in addition to the two-prong selection cuts should satisfy the following criteria:

- θ of both tracks $\in$ (30°,150°),
- momenta greater than 0.7 GeV and transverse momenta greater than 0.6 GeV,
- $|\cos\theta^*| < 0.6$,
- total transverse momentum squared $P_T^2 < 0.1\mathrm{GeV}^2$ in case of kaon selection or $P_T^2 < 0.05\mathrm{GeV}^2$ in case of pion selection,
- at least one kaon identified (kaon selection) or two particles which are not identified as muons, kaons, electrons or protons (pion selection),
- invariant mass greater than 1.5 GeV for pions and greater than 1.6 GeV for kaons.

In case of pion pair production, to reduce cosmic rays background remaining after cuts on the impact parameters, the two tracks had to pass an acolinearity cut, $|\Delta\eta - \pi| > 0.1$ rad, where $\Delta\eta$ is the angle between the tracks in three dimensions.
The events with neutral showers not associated with any charged track were rejected. Some of the events with fake showers were thus lost, but corresponding correction factor, c_f, was found using the muon sample. The ratio of the number of identified muon events, to the number of muon events without any neutral shower as a function of different kinematical variables is shown in Figs. 5.21,5.22,5.23. The fact that correction factor is constant in all variables supports the hypothesis that low-energy neutral showers accompanying the muon events, are the noises. The correction factors used in the analysis of the kaon and pion pair production are collected in Table 5.2. Finally, the 127 K^+K^- candidates and 1106 $\pi^+\pi^-$ candidates highly contaminated with $\mu^+\mu^-$ events were selected in years 1992-1995 (1994-1995 for kaons) at $\sqrt{s} = 91$ GeV. The corresponding numbers for events collected in the year 1997 at energy $\sqrt{s} = 183$ GeV are: 60 events for kaon sample and 276 events for pion sample.

Data sample	Correction factor c_f
1992-1993	1.33 ± 0.07
1994-1995	1.25 ± 0.06
1997	1.33 ± 0.08

Table 5.2: Correction factors due to the existence of noises in the calorimeters

Table 5.3 summarises all $\pi^+\pi^-$ and K^+K^- selection cuts.

In Figs. 5.24, 5.25 the number of accepted events per unit of luminosity is shown for K^+K^- and $\pi^+\pi^-$ selection, respectively. The different rates of selected events in different years is a result of the different detector acceptance and trigger efficiencies.

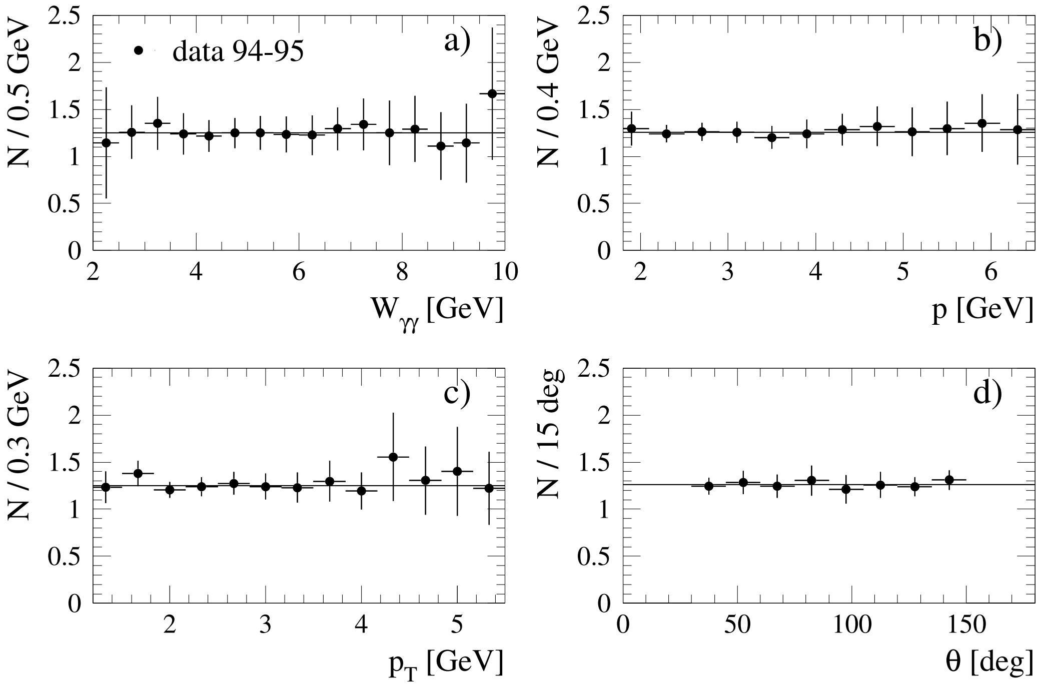

Figure 5.21: Ratio of the number of identified muon events to the number of muon events without any neutral shower as a function of: a) invariant mass, b) momentum, c) transverse momentum and d) polar angle of the final state particles. Data from the years 1994-1995.

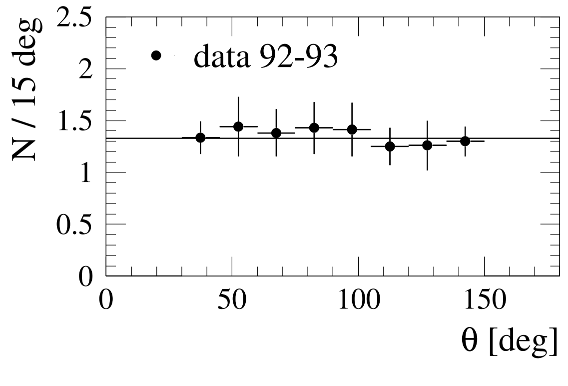

Figure 5.22: Ratio of the number of identified muon events to the number of muon events without any neutral shower as a function of polar angle of the final state particles. Data from the years 1992-1993.

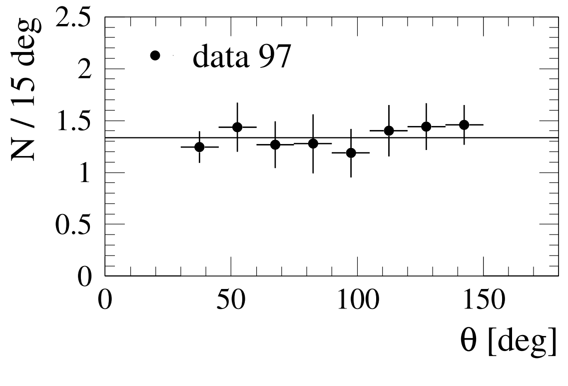

Figure 5.23: Ratio of the number of identified muon events to the number of muon events without any neutral shower as a function of polar angle of the final state particles. Data from the year 1997.

Selection cuts	Description
$N_{track} = 2$	Exactly two charged tracks
$\sum Q_i = 0$	Zero net charge
$Imp_z < 4\text{cm}/\sin\theta$	Small impact parameter in the z direction
$Imp_{r\phi} < 4$ cm	Small impact parameter in the $r\phi$ plane
$\Delta p/p < 1$	Relative momentum error less than 100%
track length > 30 cm	Long track
$30° < \theta < 150°$	Polar angle of the track
$p > 0.7$ GeV	Momentum of the particle
$p_T > 0.6$ GeV	Transverse momentum of the particle
$P_T^2 < 0.1\text{GeV}^2$ (kaon selection)	Transverse momentum balance
$P_T^2 < 0.05\text{GeV}^2$ (pion selection)	
$\lvert\pi - \Delta\phi\rvert < 0.35$ rad	Tracks back-to-back in the $r\phi$ plane
$\lvert\pi - \Delta\eta\rvert > 0.1$ rad (pion selection)	Tracks not back-to-back in 3D
$N_{neut} = 0$	Rejection of events with neutral showers
	not associated with any charged track
$\lvert\cos\theta^*\rvert < 0.6$	Large angle scattering in
	the $\gamma\gamma$ centre-of-mass system
Known luminosity	Rejection of runs with unknown $\mathcal{L}$
Good detector performance:	TPC,ID,OD,HCAL,HPC
	+ MUF,MUB (muon/pion selection)
	+ RICH (kaon selection)
Trigger requirement	Events triggered by at least
	one function from A or B groups
$W_{\gamma\gamma} > 1.6$ GeV (kaon selection)	High invariant masses
$W_{\gamma\gamma} > 1.5$ GeV (pion selection)	
Not a muon	Rejection of muons
Not an electron	Rejection of electrons
At least one good kaon	Kaon selection
Two pions (not kaon and not proton)	Pion selection

Table 5.3: Cuts used in the kaon and pion pairs selection.

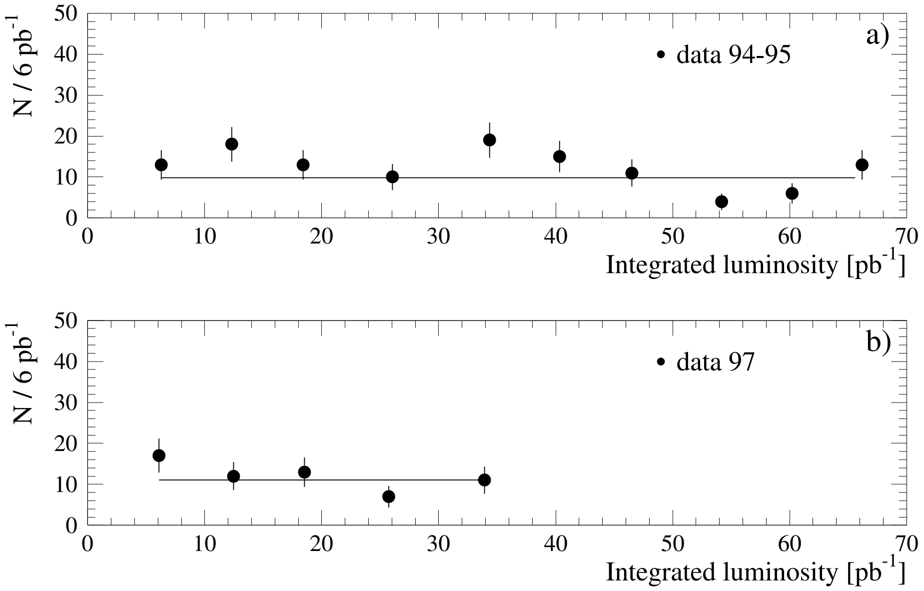

Figure 5.24: Number of accepted kaon events per $6pb^{-1}$ of collected luminosity as a function of accumulated luminosity for all data samples. The horizontal lines represent fits to the data points.

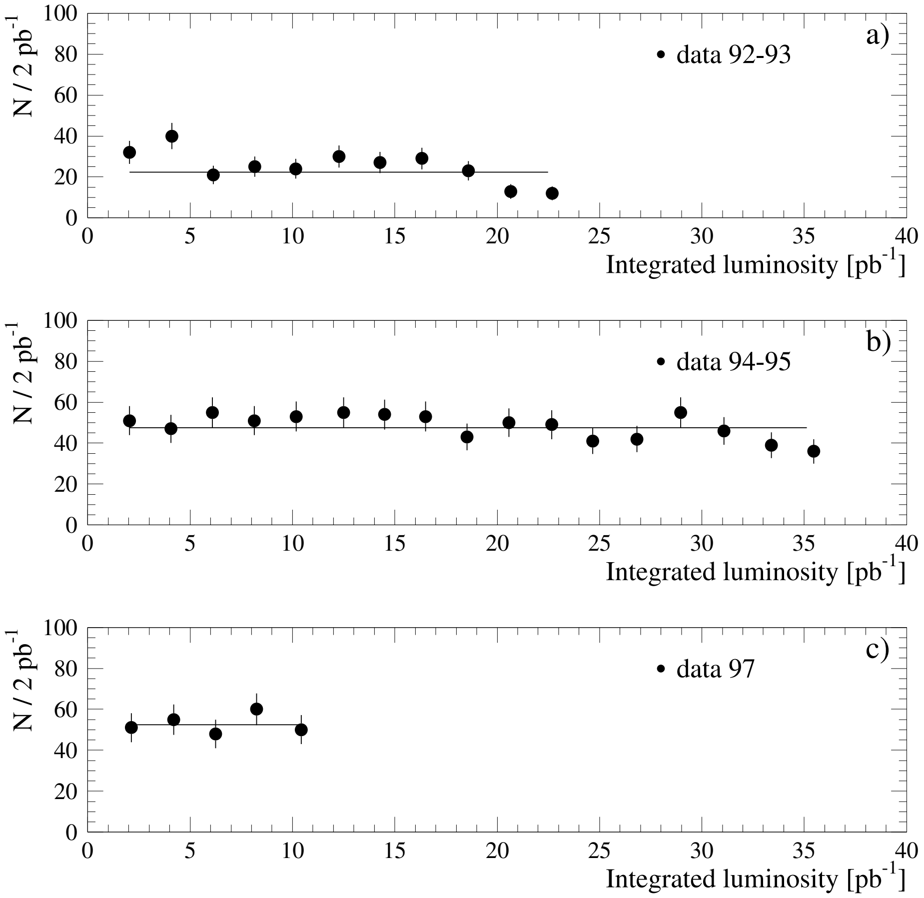

Figure 5.25: Number of accepted pion/muon events per $2pb^{-1}$ of collected luminosity as a function of accumulated luminosity for all data samples. The horizontal lines represent fits to the data points.

In Fig. 5.26 the comparison between data and the sum of background and Galuga Monte Carlo for the process $\gamma\gamma \to K^+K^-$ is shown for the highest statistics data sample from years 1994-1995. In Fig. 5.27 the comparison between data and the sum of background and two Monte Carlo (Galuga and Vermaseren) for the process $\gamma\gamma \to \pi^+\pi^-$ is shown for the same data taking period as in case of kaons. The distributions of invariant mass, transverse momentum, momentum and polar angle of the tracks are presented. Data were corrected for the trigger efficiency. All Monte Carlo distributions have been normalised to the luminosity of the data. The background is shown as hatched histogram. In case of kaon sample the agreement between data and the Galuga Monte Carlo is good, but this model does not describe the pion data. Much better agreement is obtained with the Vermaseren Monte Carlo.

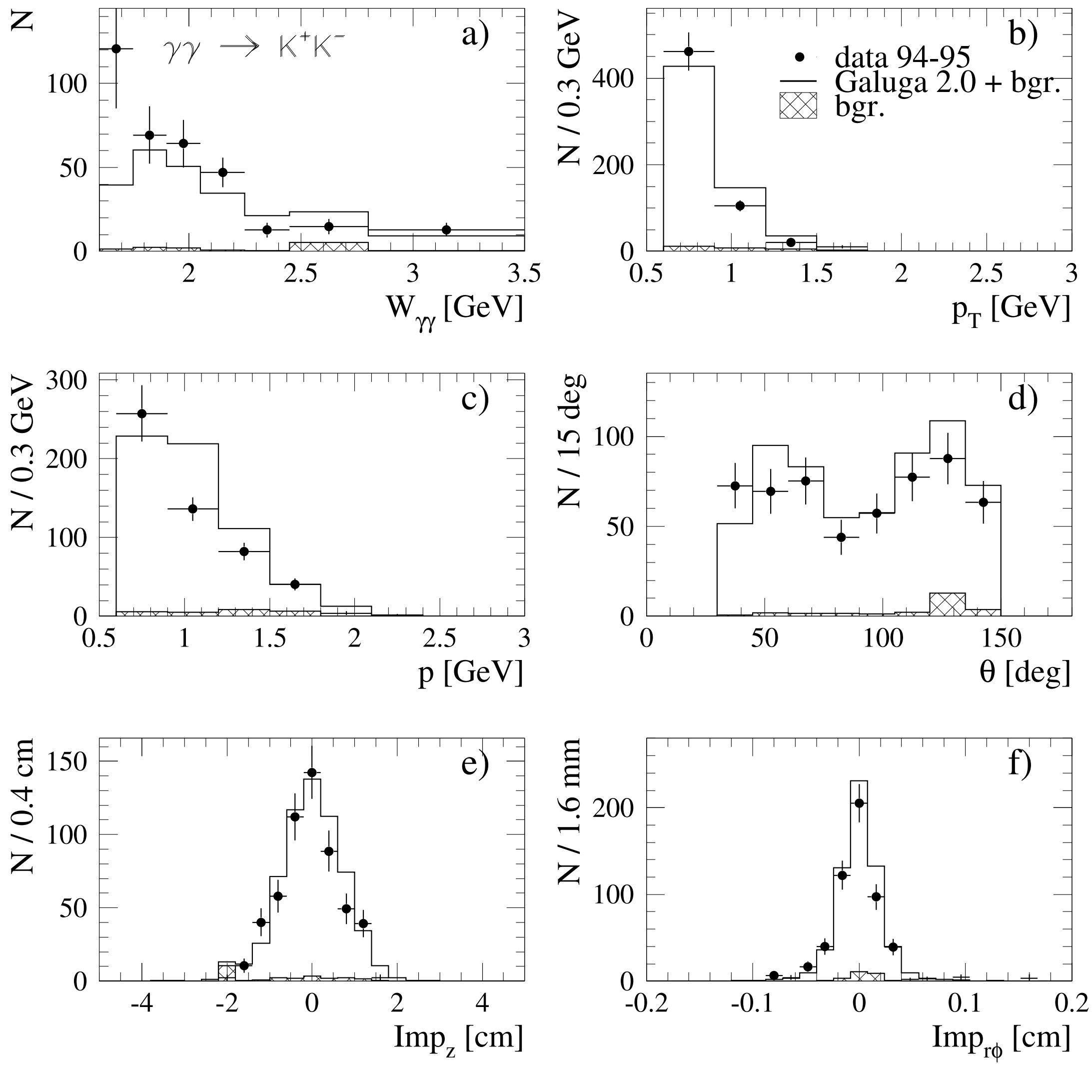

Figure 5.26: Comparison between data (full dots) and Galuga Monte Carlo (solid line) for a) invariant mass, b) transverse momentum, c) momentum, d) polar angle, e) impact parameter in the z direction and f) impact parameter in the $r\phi$ plane. The simulation background from $e^+e^- \to e^+e^-\tau^+\tau^-$, $e^+e^- \to e^+e^-e^+e^-$, $e^+e^- \to e^+e^-\pi^+\pi^-$ and $e^+e^- \to e^+e^-\mu^+\mu^-$ processes is shown as hatched histograms. Monte Carlo distributions have been normalised to the luminosity of the data. Data from the years 1994-1995, $\sqrt{s} = 91$ GeV.

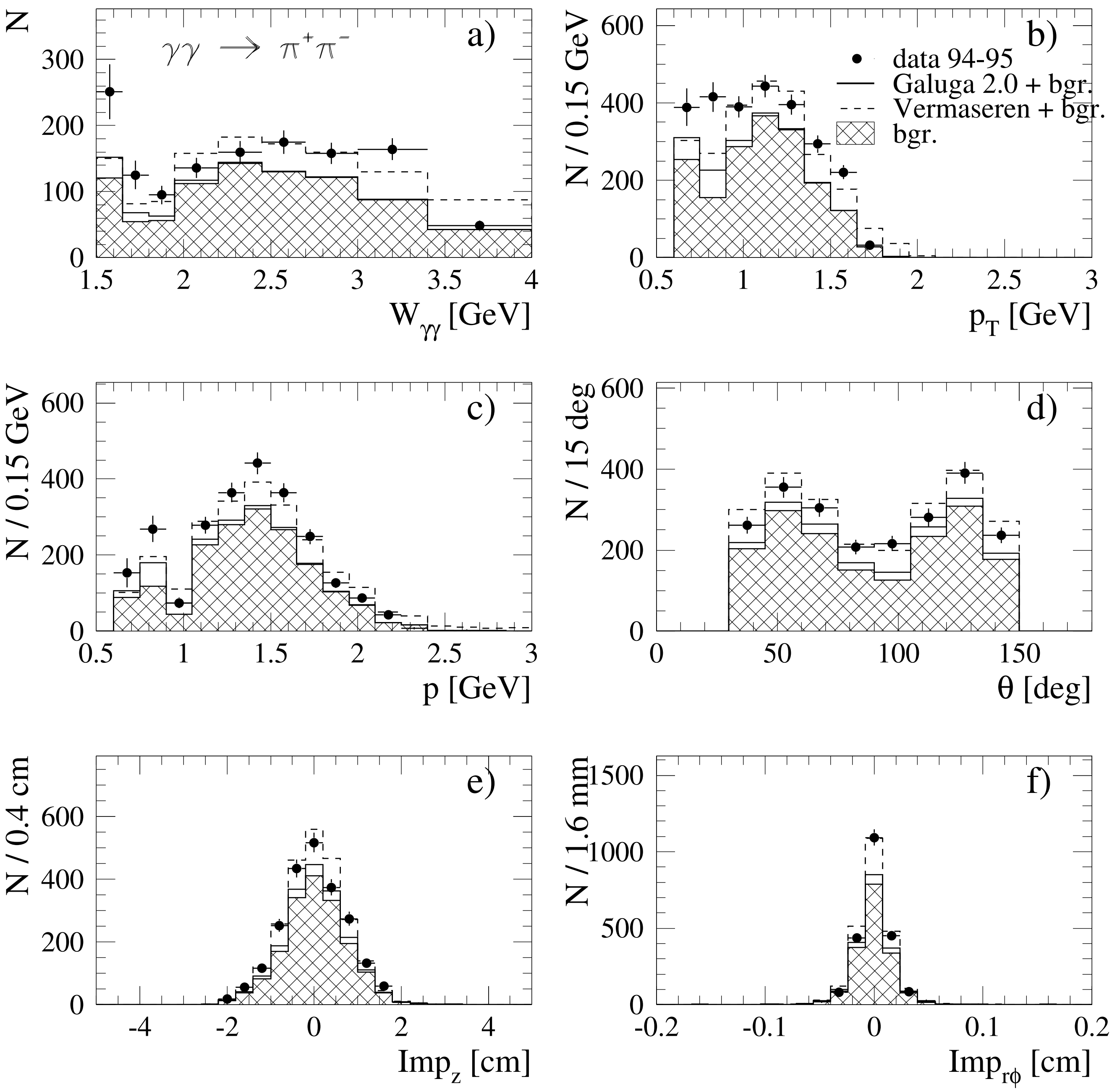

Figure 5.27: Comparison between data (full dots), the sum of the Galuga Monte Carlo and background (solid line) and the sum of the Vermaseren Monte Carlo and background for: a) invariant mass, b) transverse momentum, c) momentum, d) polar angle, e) impact parameter in the z direction and f) impact parameter in the $r\phi$ plane. The simulation background from $e^+e^- \rightarrow e^+e^-\mu^+\mu^-$, $e^+e^- \rightarrow e^+e^-\tau^+\tau^-$, $e^+e^- \rightarrow e^+e^-e^+e^-$ and $e^+e^- \rightarrow e^+e^-K^+K^-$ processes is shown as hatched histograms. Monte Carlo distributions have been normalised to the luminosity of the data. Data from the years 1994-1995, $\sqrt{s} = 91$ GeV.

5.6.1 Backgrounds

In the following, the knowledge about possible backgrounds to the kaon and pion pair production is summarised, starting from the backgrounds common for K^+K^- and $\pi^+\pi^-$ final state.

- Beam-gas interactions

  Introducing the cuts on the impact parameters removes most of this background. As beam-gas events are uniformly distributed in z, the number of events falling outside the cut on Imp_z was used to estimate the remaining background inside the cut and beam-gas contamination is found to be negligible (Figs. 5.26, 5.27).

- Four-fermion processes

  The bremsstrahlung, annihilation and conversion diagrams (Fig.4.1) are the most important in case of process $e^+e^- \to e^+e^-e^+e^-$ as the electron has a small mass. The BDK generator was used to find the ratios of these cross-sections to the cross-section for multiperipheral process. For $W_{\gamma\gamma} > 0.8$ GeV and polar angle θ of electrons from $\gamma\gamma$ interaction $\in (20°,160°)$, contribution of bremsstrahlung, annihilation and conversion diagrams to the channel $e^+e^- \to e^+e^-e^+e^-$ are less than 0.05%. Consequently, the background from similar diagrams with two electrons replaced by heavier particles (muons, taons, pions or kaons) is as well negligible.

- Electron pair production

  The $\gamma\gamma \to e^+e^-$ process is characterised by a large cross-section, in comparison to the investigated processes. However, for low-momenta particles the very good electron separation can be achieved on the basis of the dE/dx measurement alone. The remaining background was examined using the Vermaseren Monte Carlo. For Monte Carlo luminosity comparable with the luminosity of the data, not a single e^+e^- event was accepted as a K^+K^- or $\pi^+\pi^-$ candidate.

- Proton pair production

  The events with at least one particle identified as a proton were rejected. However, even without rejection of the protons, the two-photon production of proton-antiproton pairs can be neglected due to the steep $W_{\gamma\gamma}$ dependence of the cross-section [52].

- Tau pair production and other higher multiplicity final states

  Events with more than two particles in the final state are effectively reduced by the cuts on total transverse momentum of the event and by requirement that tracks should be produced back-to-back in the $r\phi$ plane, where is no influence of the boost. The example of such process is taon pair production in the two-photon interactions. On the basis of Vermaseren and BDKRC Monte Carlo, the residual background from that process to the pion as well as to the kaon sample was found to be negligible. The background from processes with additional neutral particle/particles is neglected as all events with neutral showers not associated with charged tracks were removed from the final data samples.

- Cosmic ray background

Cosmic ray events are removed very effectively after imposing cuts on the impact parameters. In case of pion pair production, where this background is more important, the two tracks had to pass in addition an acolinearity cut: the angle $\Delta\eta$ between the tracks had to be greater than 0.1 rad. After above cuts this background is negligible.

- Muon pair production

The dominant background to the two-pion signal is the $\gamma\gamma \to \mu^+\mu^-$ process. At low energies, typical for the two-photon interactions, muons and pions cannot easily be distinguished from each other and the high cross-section for the $\gamma\gamma \to \mu^+\mu^-$ process leads to a substantial contamination of the pion sample. To reduce background, events containing at least one identified muon were rejected.
With a sample of $\gamma\gamma \to \mu^+\mu^-$ events from Vermaseren Monte Carlo, it was found that after all cuts which define the $\pi^+\pi^-$ sample the efficiency of muons rejection is 100% for events with invariant masses greater than 4 GeV. Below this value, the rejection efficiency falls off rapidly, being only around 20% for $W_{\gamma\gamma} = 2$ GeV.
The muon pair identification efficiency as a function of invariant mass (with pion mass assumed for both muons to see impact of muon background on the $\pi^+\pi^-$ sample) is shown in Fig.5.28.

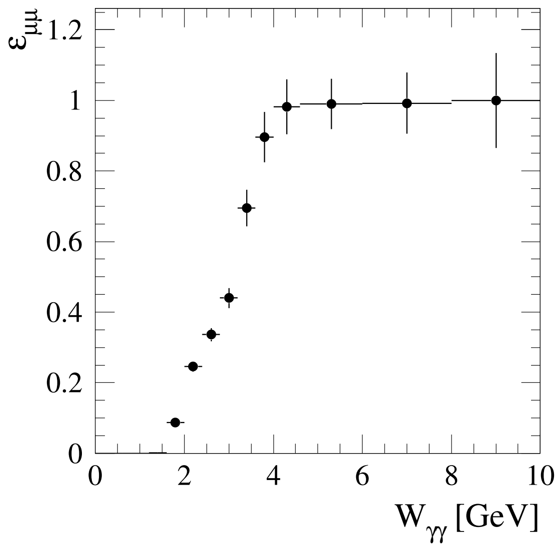

Figure 5.28: Muon pair identification efficiency as a function of invariant mass. Pion mass was assumed for both muons. Vermaseren Monte Carlo for the process $\gamma\gamma \to \mu^+\mu^-$.

- Kaon pair production

  Due to the possible particle misidentification, the process $\gamma\gamma \to K^+K^-$ can be a background to the pion pair production. To avoid this possibility, the tracks with dE/dx within one standard deviation of the expected ionisation for a kaon were rejected. After this cut, the kaon contamination in the pion sample was examined using the Galuga Monte Carlo and found to be negligible.

- Pion pair production

  In the opposite to the described above kaon background, the process $\gamma\gamma \to \pi^+\pi^-$ has to be considered as the possible background to the kaon pair production. On the basis of Galuga Monte Carlo, the background from that process was found to be about 6%. The other argument that this background should not be bigger comes from the fact that kaon identification efficiency, as found in section 5.2.3 on the basis of the experimental data, agrees with the one determined from the Monte Carlo.

5.7 Invariant masses above 2.5 GeV

As it was shown in the section 5.3, for the high mass region ($W_{\gamma\gamma} \gtrsim 2.5$ GeV) the 100% trigger efficiency can be assumed. In Fig.5.29 the distributions of invariant mass of the $\pi^+\pi^-$ candidates are shown for all considered data samples. The simulated background, in majority coming from $\gamma\gamma \to \mu^+\mu^-$ process, is shown as a histogram. The sum of all considered data in two histogram binnings (50 MeV and 100 MeV) is shown in Fig.5.30. Some excess of data is seen around invariant mass of 3.15 GeV. Furthermore, this excess can be seen in data from 1994, 1995 and 1997 and cannot be excluded in the 1992-1993 data. It becomes more significant after cut on $|\cos\theta^*| < 0.6$ and does not disappear after changing the histogram binning. All events from this region in years 1994-1995 were scanned and nothing particular was found. The mass around 3.1 GeV suggest the production of the J/ψ resonance as the sample is highly contaminated with low-momenta muons. However, the J/ψ cannot be formed in $\gamma\gamma$ interactions alone, as it has quantum numbers $J^{PC} = 1^{--}$. One can consider diffractive J/ψ production of the type $\gamma\gamma \to J/\psi X$ where the state X remained undetected in the beam pipe, but the cross-section for a process of this kind is expected to be very small. For example, cross section for the process $\gamma\gamma \to J/\psi\rho^\circ$ has been estimated to be of the order of 0.01 nb which corresponds to 30 expected events in the whole data sample. [53].
Also if the above excess is a reflection of J/ψ production, it should also be seen in the invariant mass distribution of the sum of pion and muon pair candidates. Such distribution is shown in Fig.5.31 and no excess is observed.

In conclusion, the statistic significance of the observed excess is too low to allow for any definite statement and more data are needed to interpret the mass spectrum in this region.

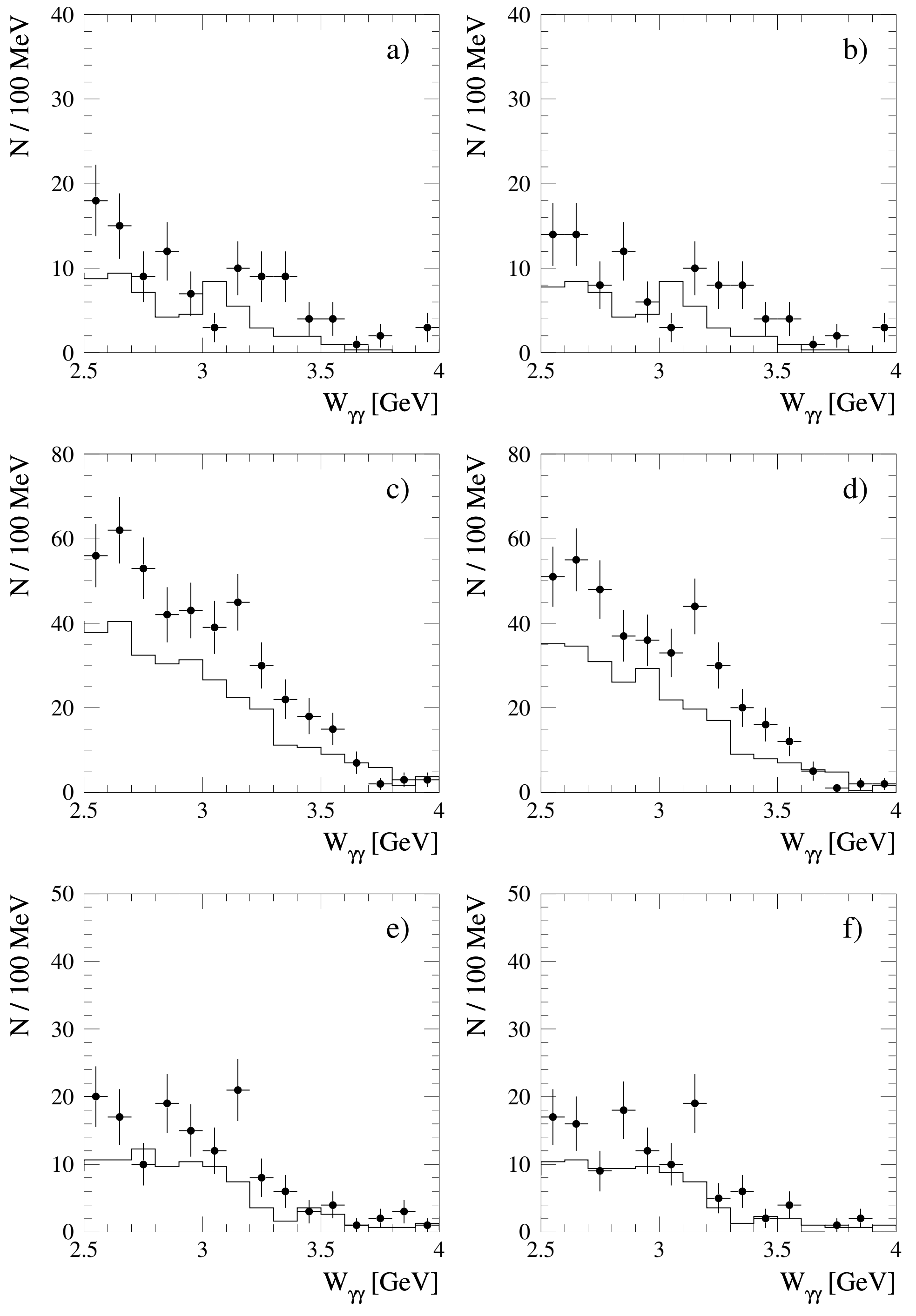

Figure 5.29: Distributions of invariant mass for pion candidates in years 1992-1993 (a,b); 1994-1995 (c,d) and 1997 (e,f). In b),d) and f) the cut on $|\cos\theta^*| < 0.6$ was imposed. The simulated background, in majority coming from $\gamma\gamma \to \mu^+\mu^-$ process, is shown as a histogram.

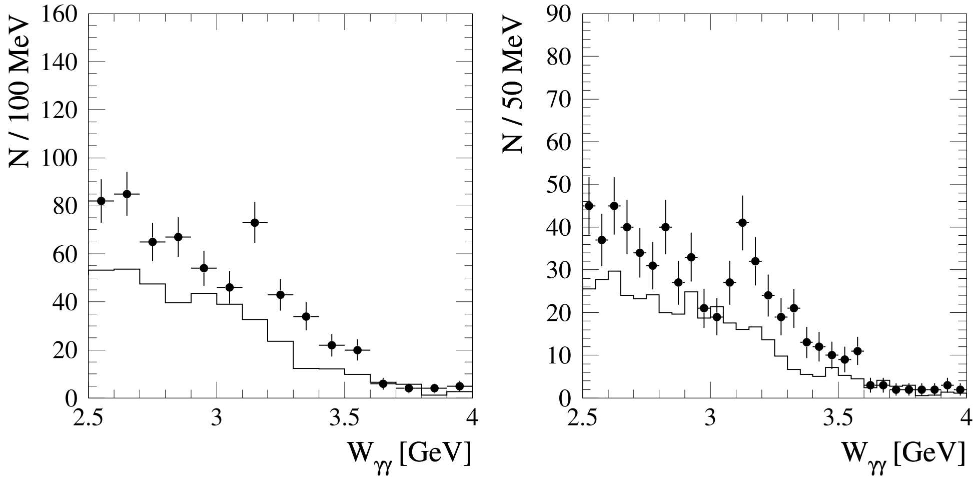

Figure 5.30: Distributions of invariant mass for pion candidates. Sum of all considered data, $|\cos\theta^*| < 0.6$. The simulated background, in majority coming from $\gamma\gamma \rightarrow \mu^+\mu^-$ process, is shown as a histogram.

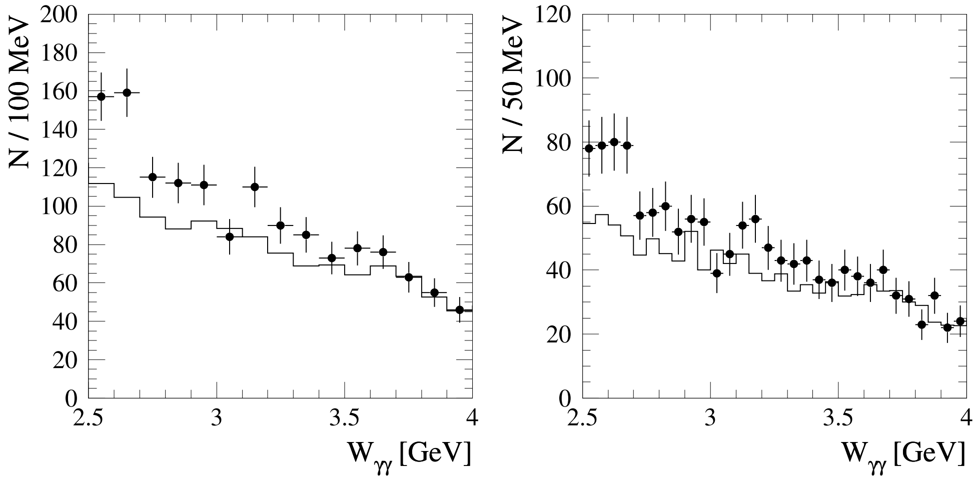

Figure 5.31: Distributions of invariant mass for pion and muon candidates. Sum of all considered data, $|\cos\theta^*| < 0.6$. The sum of the simulation background from $e^+e^- \rightarrow e^+e^-\tau^+\tau^-$, $e^+e^- \rightarrow e^+e^-e^+e^-$ and $e^+e^- \rightarrow e^+e^-K^+K^-$ processes and the $e^+e^- \rightarrow e^+e^-\mu^+\mu^-$ Monte Carlo is shown as a histogram.

Chapter 6

Results

6.1 Cross-sections

In the following, the cross-sections for two-photon production of charged meson pairs are presented for $W_{\gamma\gamma} > 1.5$ GeV in case of $\pi^+\pi^-$ and for $W_{\gamma\gamma} > 1.6 GeV$ in case of K^+K^- final state. There are three reasons to concentrate on the high invariant mass region. First, there is hope that the perturbative QCD description becomes valid there. Second, the role of the strong f_2 and f_2' resonance production is small in this region. Third, the trigger efficiencies and all other corrections are well controlled, which is not the case for smaller $W_{\gamma\gamma}$.

The cross-section for two-photon production of $M\overline{M}$ pairs as a function of $W_{\gamma\gamma}$ was determined from the number $N_{M\overline{M}}$ of events which passed all selection cuts, using the following equation:

$$\sigma(\gamma\gamma \to M\overline{M}) = \frac{dN_{M\overline{M}}/dW_{\gamma\gamma}}{\varepsilon \mathcal{L} d\mathcal{L}_{\gamma\gamma}/dW_{\gamma\gamma}} \tag{6.1}$$

where $\mathcal{L}$ is the integrated e^+e^- luminosity, ε - total detection efficiency of $M\overline{M}$ events and $d\mathcal{L}_{\gamma\gamma}/dW_{\gamma\gamma}$ is the $\gamma\gamma$ luminosity function approximated by the formula 2.21, with $Q^2_{max} = m^2_\rho$ [2].
The efficiency ε can be factorised into trigger efficiency ε_t, detector efficiency ε_{MC} determined from Monte Carlo simulation and $\varepsilon_{cf} = 1/c_f$ with correction factor c_f as shown in Table 5.2. Then $\varepsilon = \varepsilon_t \varepsilon_{MC} \varepsilon_{cf}$.
As the formula 2.21 overestimates the exact luminosity function [54] by about 10%, the corresponding scaling factor on $\mathcal{L}_{\gamma\gamma}$ were introduced.

The resulting cross-sections for charged kaon pair production at $\sqrt{s} = 91$ GeV and $\sqrt{s} = 183$ GeV as a function of K^+K^- invariant mass are shown in Figs. 6.1 and 6.2. The cross-sections for charged pion pair production at $\sqrt{s} = 91$ GeV and $\sqrt{s} = 183$ GeV are shown for all considered data samples in Figs. 6.3, 6.4 and 6.5.
The DELPHI data (this analysis) are shown as full dots. Open circles represent data from the TPC/Two–Gamma experiment, collected at $\sqrt{s} = 29$ GeV. All errors (for the DELPHI data as well as for the TPC/Two–Gamma data) are statistical only.
The solid curves in all figures correspond to Brodsky and Lepage leading order QCD predictions. The very good agreement has been obtained between all considered data samples in case of cross-section for the process $\gamma\gamma \to \pi^+\pi^-$ as well as for the process $\gamma\gamma \to K^+K^-$. It is worth to stress here that the agreement was obtained for data samples with different incident e^+e^- energies and different acceptance and trigger corrections.

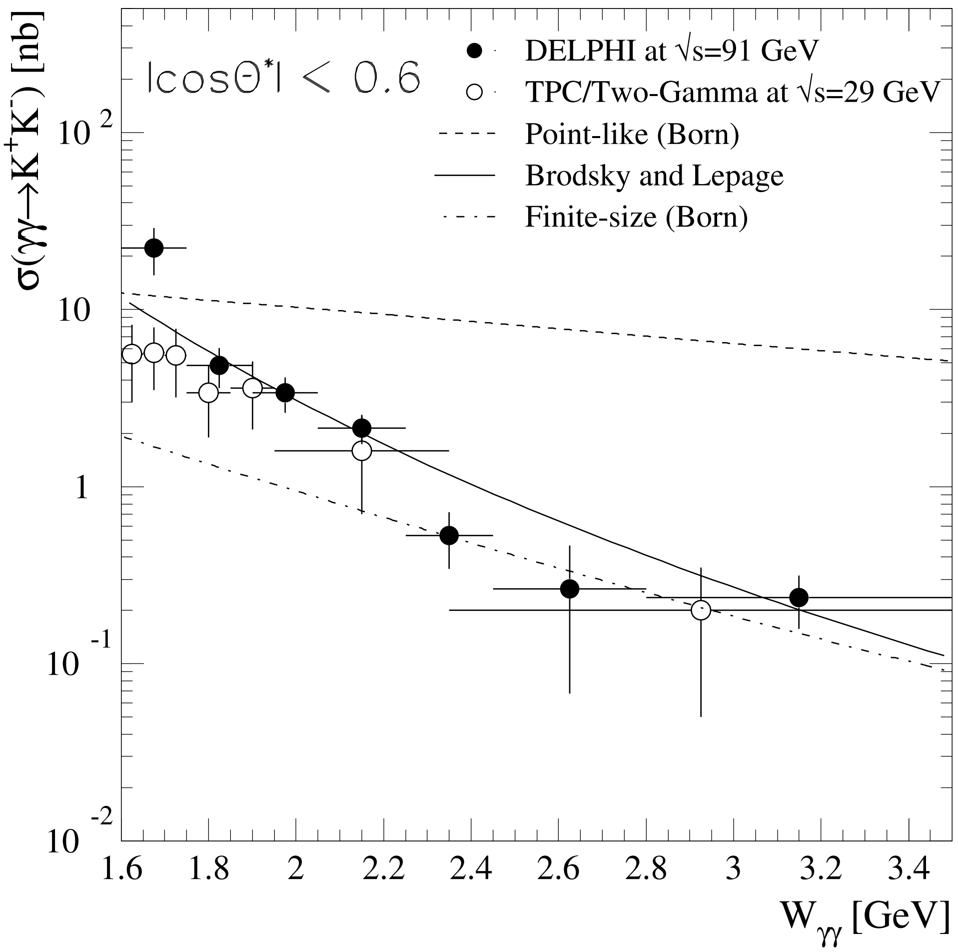

Figure 6.1: Cross-section for two-photon production of kaon pairs as a function of invariant mass $W_{\gamma\gamma}$ for $|\cos\theta^*| < 0.6$ and $\sqrt{s} = 91$ GeV. The DELPHI data (1994-1995) are shown as full dots. The leading order (Brodsky and Lepage) QCD predictions are shown as the solid line. The QED predictions (point-like kaons) and results of calculations in the finite-size model are shown as the dashed and the dashed-dotted lines, respectively. The TPC/Two–Gamma data are shown as open circles. Errors are statistical only.

In case of charged kaon production, the measured cross-section agrees both in shape and in absolute normalisation with leading-order QCD predictions. The point-like as well as the finite-size models do not describe the data. The data are also in good agreement with the only data available so far for kaon production from the TPC/Two–Gamma collaboration.

Up to now three measurements of high mass continuum production of charged kaon and pion pairs are available. However, the TPC/Two–Gamma was the only experiment to measure separately cross sections for K^+K^- and $\pi^+\pi^-$ pair production. The MARK II [3] and CLEO [5] collaborations measured only combined K^+K^- and $\pi^+\pi^-$ cross-sections. Pion data in the region below invariant mass of 2 GeV are in a good agreement with results obtained by TPC/Two–Gamma, but they are not described by the QCD predictions as in the invariant mass region from 2 GeV to about 3.5 GeV the cross-section depends very weekly on the $W_{\gamma\gamma}$.

The QED curves in the point-like meson approximation, lie above the data. In the $\pi^+\pi^-$ case the same model with interference between the f_2 resonance and the continuum in-

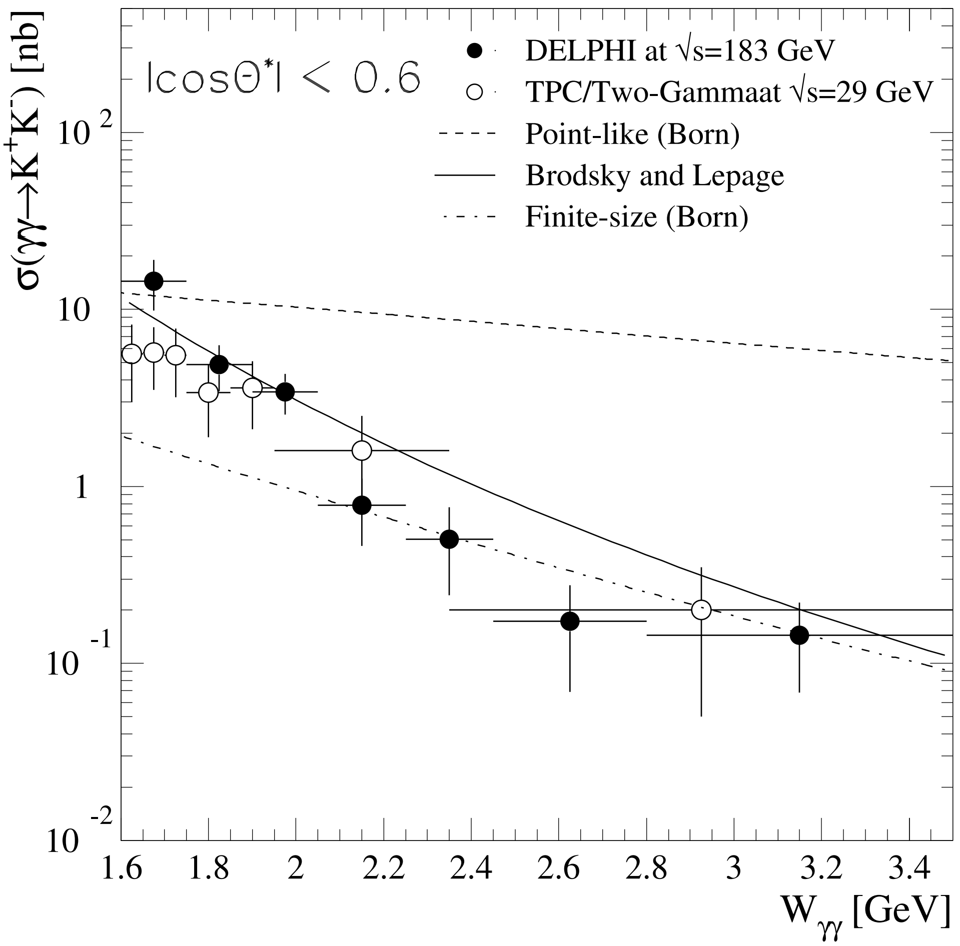

Figure 6.2: Cross-section for two-photon production of kaon pairs as a function of invariant mass $W_{\gamma\gamma}$ for $|\cos\theta^*| < 0.6$ and $\sqrt{s} = 183$ GeV. The DELPHI data (1997) are shown as full dots. The leading order (Brodsky and Lepage) QCD predictions are shown as the solid line. The QED predictions (point-like kaons) and results of calculations in the finite-size model are shown as the dashed and the dashed-dotted lines, respectively. The TPC/Two–Gamma data are shown as open circles. Errors are statistical only.

cluded, describes the data better. The finite-size curve lie much below the data.
For the K^+K^- pair production, the interference between the continuum and resonances in principle could also change the behaviour of the QED curve, but the all existing data are not statistically significant enough to extract the phase of the interference terms.
The angular distributions in the $\gamma\gamma$ centre-of-mass system of the produced meson pairs can help to distinguish between the different models. In case of the decay of the tensor resonance produced in the interactions of two quasi-real photons, the angular distribution is proportional to the $\sin^4\theta$. The $|\cos\theta^*|$ distribution obtained in the Born approximation is almost flat for the $|\cos\theta^*|$ <0.6, whereas the perturbative QCD models predict the peaking in the forward direction.
The measurement of differential cross-sections $d\sigma/d|\cos\theta^*|$ for four $W_{\gamma\gamma}$ bins for the process $\gamma\gamma \to \pi^+\pi^-$ and in two $W_{\gamma\gamma}$ bins in case of the $\gamma\gamma \to K^+K^-$ production is presented in Figs. 6.6, 6.7. The general data behaviour is in good agreement with the CLEO results for mixed kaon and pion sample. The two other collaborations did not show the $d\sigma/d|\cos\theta^*|$ distributions. The statistics is too low to allow for any definite statement,

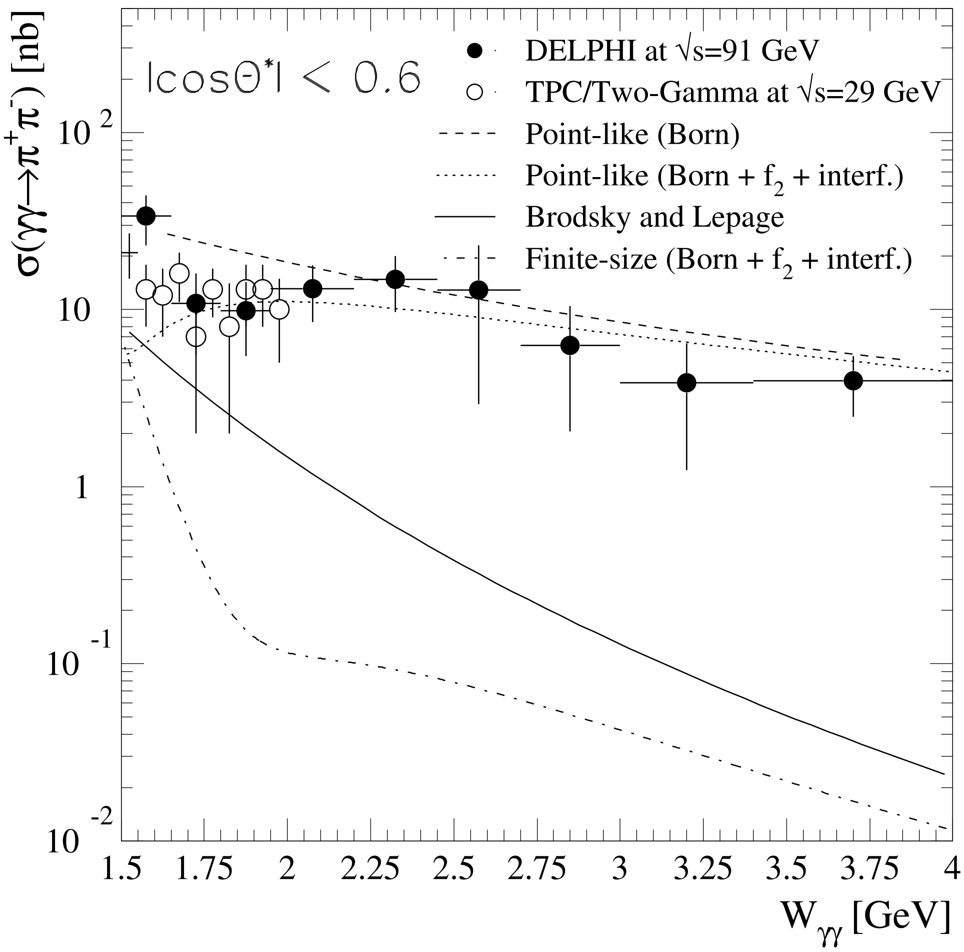

Figure 6.3: Cross-section for two-photon production of pion pairs as a function of invariant mass $W_{\gamma\gamma}$ for $|\cos\theta^*| < 0.6$ and $\sqrt{s} = 91$ GeV. The DELPHI data (1992-1993) are shown as full dots. The leading order (Brodsky and Lepage) QCD predictions are shown as the solid line. The QED calculations (point-like pions) with and without interference between the f_2 resonance and the continuum are shown as dotted and dashed curve, respectively. Results of calculations in the finite-size model, with the interference included are shown as dashed-dotted line. The TPC/Two–Gamma data are shown as open circles. Errors are statistical only.

but the measured $\pi^+\pi^-$ differential cross-section show some rise at small scattering angles as expected by leading order perturbative QCD at the highest invariant masses.

6.2 Systematic effects

There are four main sources of systematic uncertainties for the measurement: model dependent detector acceptance corrections, trigger efficiency, correction for two-prong events lost due to detector noise (c_f), and normalisation of the muon or pion backgrounds for $\pi^+\pi^-$ or K^+K^x- selection, respectively.
The systematic error introduced by the detector acceptance corrections were estimated on the basis of the differences between two Monte Carlo programs: Galuga and Vermaseren. For the total $\pi^+\pi^-$ and K^+K^- cross-sections the substantial effect were found for low invariant masses below 2 GeV and the extracted cross-section in this region differ by up

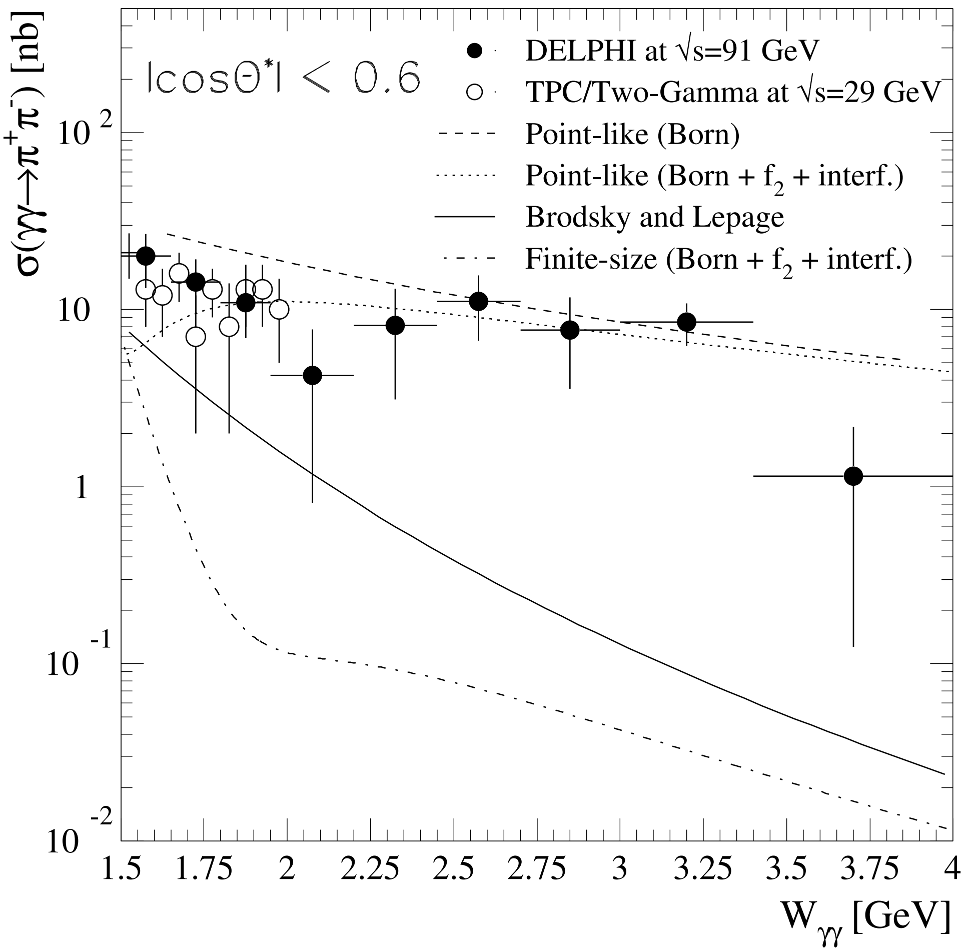

Figure 6.4: Cross-section for two-photon production of pion pairs as a function of invariant mass $W_{\gamma\gamma}$ for $|\cos\theta^*| < 0.6$ and $\sqrt{s} = 91$ GeV. The DELPHI data (1994-1995) are shown as full dots. The leading order (Brodsky and Lepage) QCD predictions are shown as the solid line. The QED calculations (point-like pions) with and without interference between the f_2 resonance and the continuum are shown as dotted and dashed curve, respectively. Results of calculations in the finite-size model, with the interference included are shown as dashed-dotted line. The TPC/Two–Gamma data are shown as open circles. Errors are statistical only.

to 20%.

The trigger efficiency uncertainties play significant role at small invariant masses, up to about 2 GeV, where trigger efficiency is changing rapidly as a function of the invariant mass. The estimated systematic error does not exceed 4% for both processes under consideration.

The systematic uncertainty of the factor c_f were estimated by studying the variation of this factor for the different data samples, in particular for data sample with two muons identified and the sample with at least one muon identified. The influence of the different cuts on the energy of the neutral showers considered as a noise were also studied. The uncertainty due to the c_f factor was found to be equal to 7%, common for pions and kaons.

In the case of pion pairs a significant component of the systematic error is due to uncertainties in the level of muon background. This was estimated from the comparison of the data and Monte Carlo for muon pair production and from difference between BDKRC

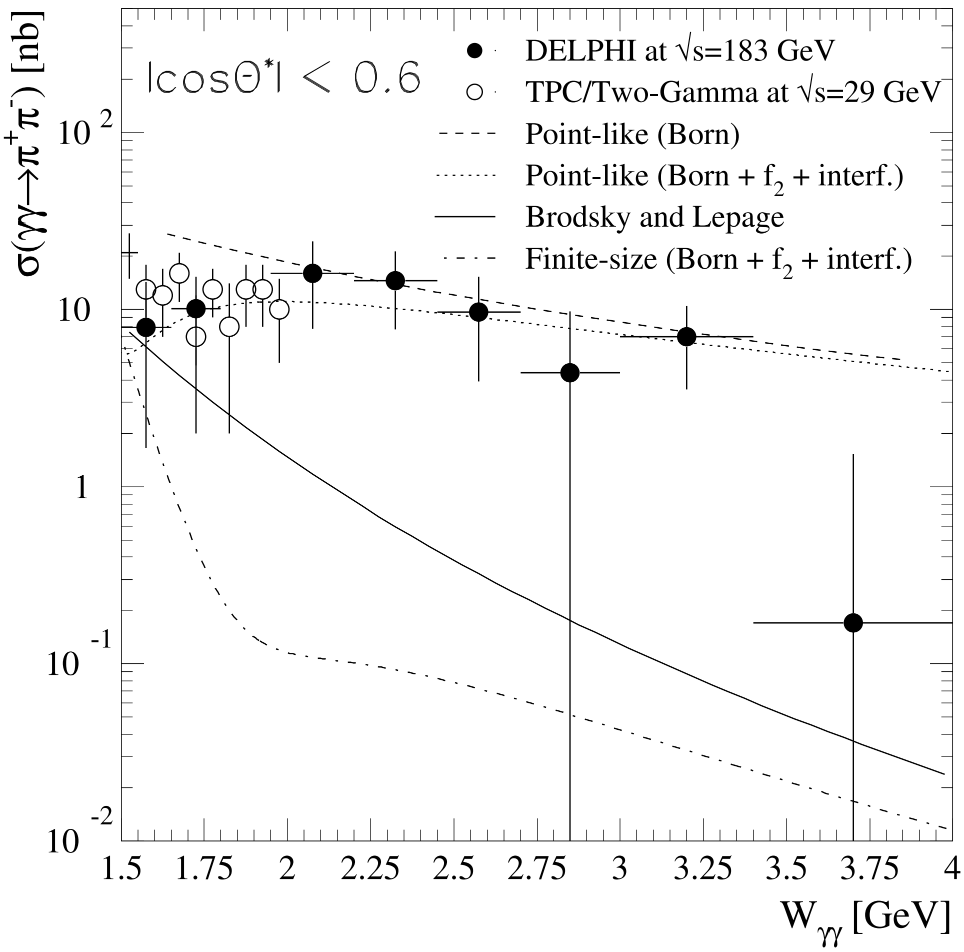

Figure 6.5: Cross-section for two-photon production of pion pairs as a function of invariant mass $W_{\gamma\gamma}$ for $|\cos\theta^*| < 0.6$ and $\sqrt{s} = 183$ GeV. The DELPHI data (1997) are shown as full dots. The leading order (Brodsky and Lepage) QCD predictions are shown as the solid line. The QED calculations (point-like pions) with and without interference between the f_2 resonance and the continuum are shown as dotted and dashed curve, respectively. Results of calculations in the finite-size model, with the interference included are shown as dashed-dotted line. The TPC/Two–Gamma data are shown as open circles. Errors are statistical only.

and Vermaseren Monte Carlo. The uncertainty of the muon background normalisation does not exceed 12% (for the 1997 data where the worst agreement between the data and Monte Carlo was observed).
Background from particle misidentification in case of kaon pair production was discussed in section 5.6.1. The estimated uncertainty due to the contamination of pions in the kaon sample is about 5%. The uncertainty due to the e^+e^- luminosity measurement is for both e^+e^- energies less than 1% and were neglected.
The combined systematic error on the cross-sections in case of kaon pair production does not exceed 22%, while corresponding error for pion production equals 25%.

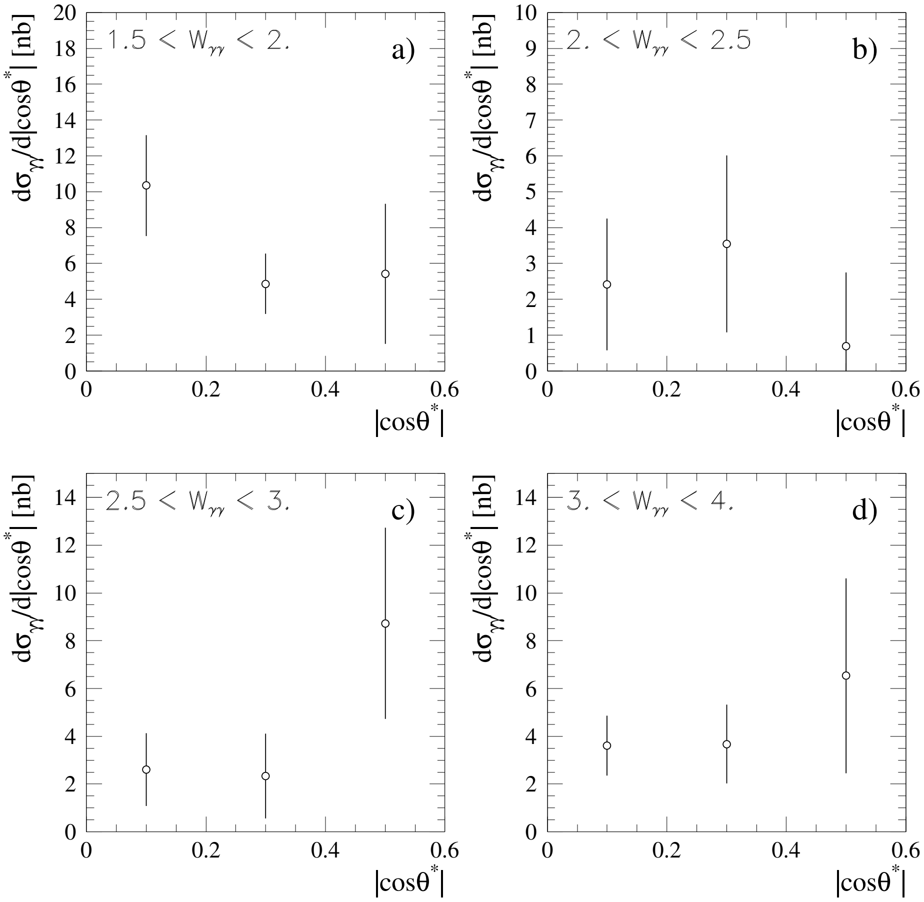

Figure 6.6: The $|\cos\theta^*|$ dependence of the two-photon cross-section for production of pion pairs for four bins in $W_{\gamma\gamma}$: a) $1.5 < W_{\gamma\gamma} < 2.$, b) $2. < W_{\gamma\gamma} < 2.5$, c) $2.5 < W_{\gamma\gamma} < 3.$ and d) $3. < W_{\gamma\gamma} < 4.$. Errors are statistical only.

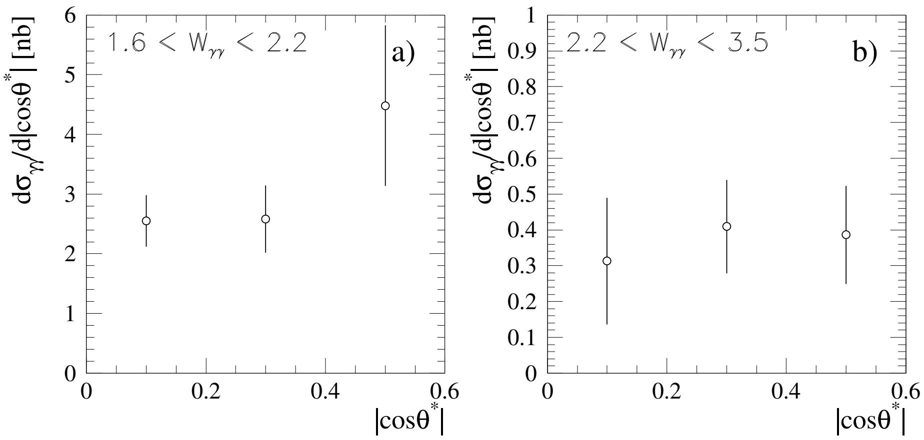

Figure 6.7: The $|\cos\theta^*|$ dependence of the two-photon cross-section for production of kaon pairs for two bins in $W_{\gamma\gamma}$: a) $1.6 < W_{\gamma\gamma} < 2.2$, b) $2.2 < W_{\gamma\gamma} < 3.5$. Errors are statistical only.

Chapter 7

Conclusions and outlook

Two-photon exclusive production of charged kaon and pion pairs was studied in untagged events collected by the Delphi experiment at $\sqrt{s}$=91 GeV and $\sqrt{s}$=183 GeV. The cross-section measurements were performed for invariant masses between 1.6 GeV and 3.5 GeV for kaons and between 1.5 GeV and 4 GeV for pions. These are the first results coming from LEP experiments, concerning exclusive two-photon production of kaons and pions at high-invariant masses.
The distinct resonance structure has been observed in the uncorrected data sample. Detailed analysis of the trigger efficiency, detector acceptance and particle identification was performed. It has been found that reliable corrections for all these effects and consequently the cross-sections measurements can be done only after relatively tight cuts on the momenta, transverse momenta and polar angle of the final state particles. For this reason precise measurements in the f_2 and f_2' mass region were not possible. However, after these cuts, for the processes $\gamma\gamma \to \pi^+\pi^-$ and $\gamma\gamma \to K^+K^-$ we have presently the highest statistics at high invariant masses (greater than 2.5-3 GeV) of the $\gamma\gamma$ system.
The good agreement between experimental data and theoretically well known process of muon pair production proved that Monte Carlo simulation, trigger efficiency determination and other important steps of the analysis were done correctly. This good agreement between data and Monte Carlo for the process $\gamma\gamma \to \mu^+\mu^-$, was obtained without any arbitrary normalisation factor. Such agreement was observed for the distributions of different kinematical variables, for all studied data samples.
The very good description of the muon pair production processes was the remedy for the fact that low-momenta muons cannot be distinguished from pions. Thus only small part of the $\mu^+\mu^-$ events were rejected on the event-by-event basis and the cross-section for the process $\gamma\gamma \to \pi^+\pi^-$ was obtained by the statistical subtraction of $\gamma\gamma \to \mu^+\mu^-$ Monte Carlo generated background. On the contrary, the background to $\gamma\gamma \to K^+K^-$ process is small.
The 127 K^+K^- candidates and 1106 $\pi^+\pi^-$ candidates highly contaminated with $\mu^+\mu^-$ events were selected in years 1992-1995 (1994-1995 for kaons) at $\sqrt{s}$ = 91 GeV. The corresponding numbers for events collected in the year 1997 at energy $\sqrt{s}$ = 183 GeV are: 60 events for kaon sample and 276 events for pion sample. The obtained cross-sections were compared to the available data from other experiments and theoretical predictions: QCD-based calculations and QED models of point-like pions (kaons) as well as with the extension of QED models where mesons are treated as extended objects parametrised by relevant form-factors (finite-size model). In case of charged kaon production, the measured cross-section agrees both in shape and in absolute normalisation with leading-order

QCD predictions. The data are also in good agreement with the previous measurement by TPC/Two–Gamma collaboration.
For pions the agreement with QCD prediction as well as with results from some other experiments is much poorer. The smaller slope of the $\pi^+\pi^-$ invariant mass distribution as compared to the K^+K^- one, support the hypothesis that the high mass resonances are seen in the $\pi^+\pi^-$ channel and/or the point-like contribution in case of pions is still not negligible.
An enhancement in the $\pi^+\pi^-$ invariant mass at about 3.1 GeV, at the three sigma level, can be interpreted as a possible diffractive J/ψ production with some final state particles escaping the detection in the beam pipe. It looks interesting that the high statistics CLEO data also show certain enhancement in the region 3-3.5 GeV. As it was stated before, low-momenta muons may mimic pions, so from this point of view the observation of the J/ψ resonance in the $\pi^+\pi^-$ sample is well possible. However, in a combined sample of $\pi^+\pi^-$ and $\mu^+\mu^-$ samples, an enhancement is statistically non significant.

Comparing the DELPHI data with the data from the previous experiments one should underline that in case of DELPHI, the available e^+e^- energy is much higher than in previous experiments. The TPC/Two–Gamma data were collected at $\sqrt{s} = 29$ GeV and the CLEO data at $\sqrt{s} \simeq 10$ GeV. Thus the experimental conditions are not identical and the imposed cuts not always have the same meaning. In particular at LEP the photons of higher energies can be produced and the role of the diffractive events grows with energy.
In conclusion, the statistic significance of the observed excess in the $\pi^+\pi^-$ spectrum does not allow for definite statement, but there is an indication that something interesting can happen in this region.
From the theoretical side, the first results concerning cross-section for the process $\gamma\gamma \to \pi^+\pi^-$ in modified perturbative approach were shown [55] at the Photon 2000 conference. The new approximations of hard scattering amplitude have been investigated. The first one is Brodsky and Lepage approach, where the T_H amplitude has been computed with quarks collinear with the outgoing mesons. In the new, more precise approach, the parton transverse momentum has been taken into account. The curve in this approximation is less steep than in Brodsky and Lepage approach, but the overall normalisation is similar.
There is hope that new data from LEP, collected in year 2000 with lower trigger thresholds, at e^+e^- energy above 200 GeV can shed new light on the exclusive two-meson production mechanisms. The new data are also expected from the B-factories.

Acknowledgements

I would like to express gratitude to my supervisor Prof. Krzysztof Doroba for the constant support during my work on this thesis.

I would like to thank all the members of the DELPHI Warsaw and Cracow groups, and in particular those of the two-photon analysis groups, for the fruitful discussions and the friendly atmosphere.

I am indebted to Prof. Hans Paar for expressing interest in my work. I have benefited very much from discussions with him, unfortunately only few ones.

I would like to thank Lech Mankiewicz for helpful discussions of some theoretical aspects of my work and for reading the chapter concerning theory of photon-photon interactions.

I am indebted to Mariusz Przybycień for a critical reading of the big parts of the manuscript and correcting some logical and linguistic errors.

I am very grateful to Prof. Helena Bialkowska for her patience in answering my endless questions concerning English vocabulary and stylistics.

The support of Polish State Committee for Scientific Research, grant no. 2P03B01612, is also acknowledged.

Last, but by no means least, I would like to thank my family for their continuous encouragement and support.

Appendix A

Events from Delphi Graphic Event Display

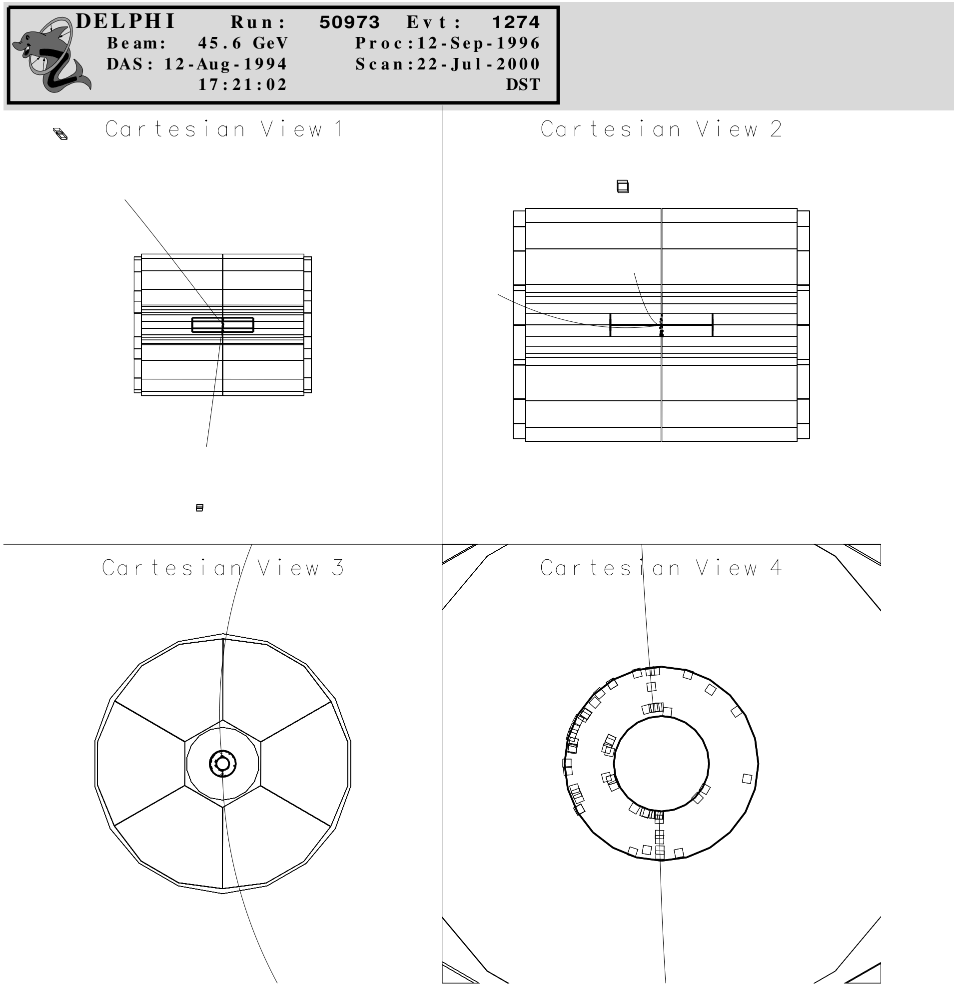

Figure A.1: One of the $\pi^+\pi^-$ candidate from the DELPHI Event Display. The event is shown in the three projections: yz, xz and xy. Out of the whole DELPHI detector sketch of Time Projection Chamber and Vertex Detector is shown only. Small squares represent energy deposits in the Hadron Calorimeter and hits in the Vertex Detector. Lines are the reconstructed tracks.

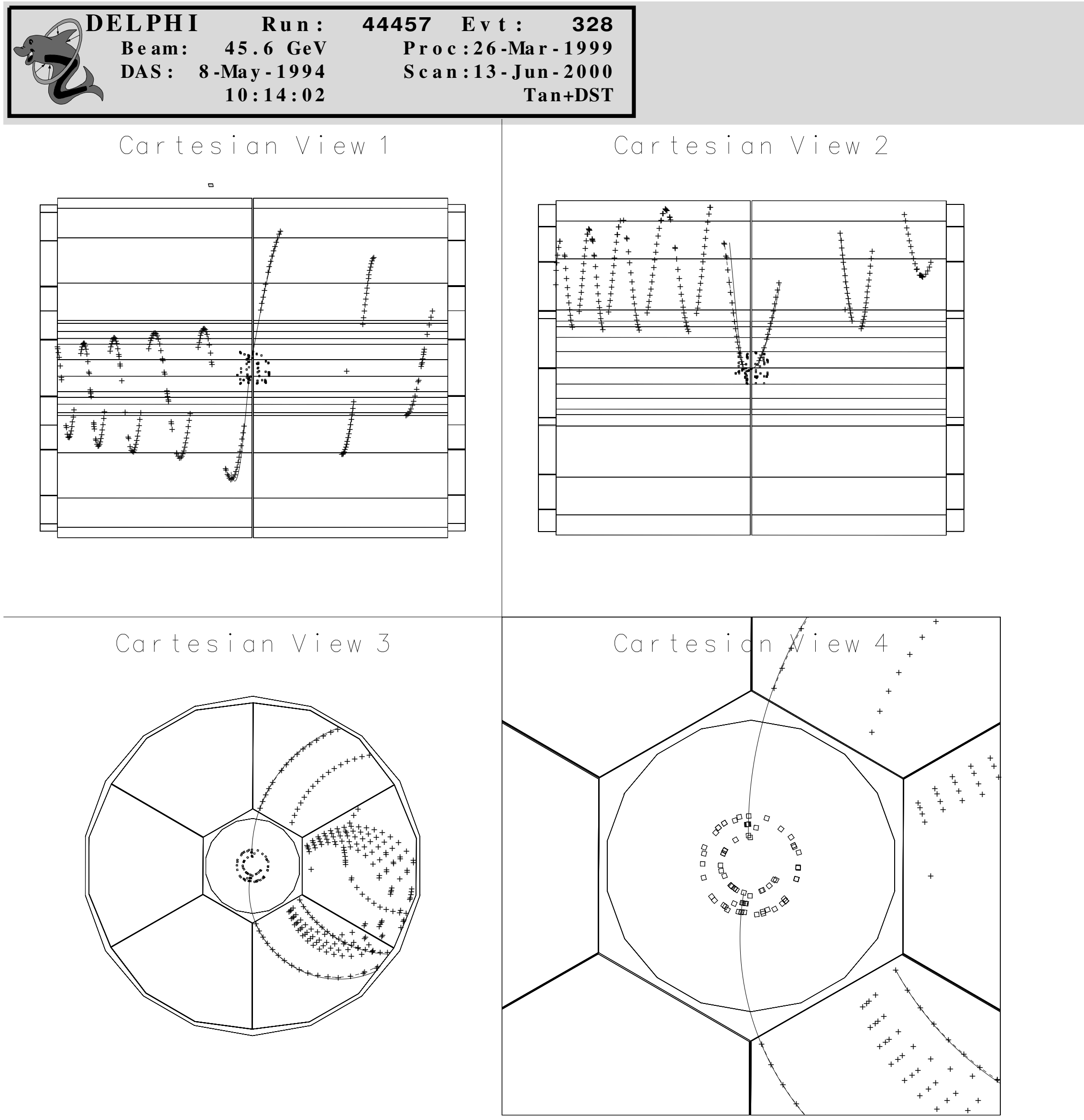

Figure A.2: An example of a badly reconstructed event from the DELPHI Event Display. The event is shown in the three projections: yz, xz and xy. Out of the whole DELPHI detector sketch of Time Projection Chamber is shown only. Crosses and small squares represent hits in the TPC and in the Vertex Detector. Lines are the reconstructed tracks. In the event shown here only two low-momentum particles were produced but the reconstruction program found the three tracks with two of them belonging to the same helicy.

Appendix B

Monte Carlo samples

Only the simulation events for the process $\gamma\gamma \to \tau^+\tau^-$ at $\sqrt{s} = 183$ GeV ('97) were taken from the set of centrally created DELPHI Monte Carlo samples. The simulation events for the other processes didn't exist because the physics processes studied in this thesis are not typical for DELPHI experiment.

Process	Generator	Year	$W_{\gamma\gamma}$ [GeV]	θ [deg]	$\sigma_{e^+e^-}$ [pb]	Nb of events
$\gamma\gamma \to \pi^+\pi^-$	Galuga	'97	> 1.4	20-160	152*	72614**
	Galuga	'95	> 1.2	20-160	298**	62749**
	Galuga	'94	> 1.4	20-160	110**	61436**
	Galuga	'92	> 1.2	20-160	299**	63316**
f_2 + cont.	Vermaseren	'97	$> 2m_\pi$	10-170	8821	100000
f_2 + cont.	Vermaseren	'95	> 0.8	20-160	5059**	61000**
f_2 + cont.	Vermaseren	'94	> 1.4	20-160	195	20000
f_2 + cont.	Vermaseren	'92	$> 2m_\pi$	10-170	7694	100000
$\gamma\gamma \to K^+K^-$	Galuga	'97	> 1.4	20-160	319**	82088**
	Galuga	'95	> 1.3	20-160	375**	72762**
	Galuga	'94	> 1.4	20-160	220**	69608**
$f_2 + f_2'$	Vermaseren	'97	$> 2m_K$	10-170	64	50000
$f_2 + f_2'$ + cont.	Vermaseren	'97	$> 2m_K$	10-170	485	100000
$f_2 + f_2'$ + cont.	Vermaseren	'94	$> 2m_K$	10-170	408	130000
$f_2 + f_2'$ + cont.	Vermaseren	'94	> 1.6	20-160	119	10000
$\gamma\gamma \to \mu^+\mu^-$	Vermaseren	'97	> 0.8	10-170	9625	100000
	Vermaseren	'97	> 1.3	20-160	1802	20000
	BDKRC	'95	> 0.8	0-180	28152	100000
	Vermaseren	'95	> 0.8	20-160	4117	100000
	Vermaseren	'94	> 0.8	10-170	8285	100000
	Vermaseren	'94	> 1.3	20-160	1541	20000
	Vermaseren	'93	> 0.8	20-160	4117	100000
	Vermaseren	'92	> 0.8	10-170	8285	100000
	Vermaseren	'92	> 1.3	20-160	1541	20000
	BDKRC	'92	> 0.8	0-180	28152	100000
$\gamma\gamma \to \tau^+\tau^-$	Vermaseren	'95	$> 2m_\tau$	0-180	272	25000
	Vermaseren	'94	$> 2m_\tau$	0-180	272	25000
$\gamma\gamma \to e^+e^-$	Vermaseren	'97	> 1.4	20-160	1566	20000
	DIAG36	'95	> 0.8	20-160	4228	96000
	Vermaseren	'95	> 0.8	20-160	4231	100000
	Vermaseren	'94	> 1.4	20-160	1331	20000
	Vermaseren	'93	> 0.8	20-160	4231	82000
	Vermaseren	'92	> 0.8	10-170	8285	100000

Table B.1: Monte Carlo samples created for the purpose of this analysis. A ** denotes the cross-sections and corresponding number of events before imposed cuts.

Appendix C

Trigger decision functions

Decision function	Components (TFs)	Description
DF00_I	B1	B1 signal
DF01_I	BBHH	Bhabha in STIC
	BBLL	
DF02_I	VSAT_T1Y_I	Bhabha in VSAT
	VSAT_T2Y_I	
DF03_I	PSCAC	STIC single arm
DF04_I	ID_OR_OD	ID*OD
DF05_I	TRFW_MJ1_I	Single track in FCA*FCB forw.
	TRBW_MJ1_I	Single track in FCA*FCB backw.
DF06_I	MUFW_I	Signals in HOF
	MUBW_I	
	MUVFW_I	
	MUVBW_I	
DF07_I	MUBL	Muon in barrel
	TOF_MJ1_I	Signal in TOF
	TPCFW_MJ1_I	Single track in TPC forw.
	TPCBW_MJ1_I	Single track in TPC backw.
DF08_I	EMFWLO_MJ1_I	FEMC, low energy
	EMVFWLO_MJ1_I	threshold, different
	EMBWLO_MJ1_I	angular regions
	EMVBWLO_MJ1_I	
DF09_I	HOFBB	HOF back-to back
DF10_I	EMBLLO_MJ2_I	HPC - signal in two sectors,
		low energy threshold
DF11_I	EMBLLO_MJ1_I	HPC - signal in one sector,
		low energy threshold
DF12_I	HAMU_FW	HCAL forw., muon threshold
	HALO_FW	HCAL forw., low energy threshold
	HAMU_BW	HCAL backw., muon threshold
	HALO_BW	HCAL backw., low energy threshold
DF13_I	HAMU_BL_MJ1	HCAL barrel, muon threshold
	HALO_BL_MJ1	HCAL barrel, low energy threshold
DF14_I	BBDE	Bhabha delayed
	TPCLASER	TPC laser
DF15_I	(TRFW_MJ1_I)*(TRBW_MJ1_I)	Forw.-backw. track coincidence

Table C.1: Example of the first level trigger decision functions in 1994.

Decision function	Components (TFs)	Level of coincidencies (*majorities*)	Forbidden coincidencies	Description
DF00_II	DF00_I	1		**B1 signal**
DF01_II	DF01_I	1		**Bhabha in STIC**
DF02_II	VSAT_T2Y	1		**Bhabha in VSAT**
DF03_II	DF03_I	1		**STIC single arm**
DF04_II		1		**Barrel Part 1**
	CT_MJ1			TPC contiguity trigger
	IDOD_6_MJ1			ID*OD in the TPC cracks
	TPCBB			2 tracks in oppos. endcaps in TPC
	DF10_I			Deposits in two sectors of HPC
	(DF11_I)*(TOF_MJ1)			HPC*TOF
	OD2TOF			(OD-multiplicity $\geq$ 2)*TOF
	(DF11_I)*(OD_MJ1)			HPC*OD
DF05_II		2	2-3	**Barrel Part 2**
	1) ID_MJ1			ID
	2) MUBLLC_MJ1			Hits in one octant of MUB
	3) DF13_I			HCAL barrel
DF06_II		2	1-4,1-5,	**Intermediate Region**
	1) ID_MJ1		2-3,2-5,	ID
	2) DF12_I		3-4,4-5	HCAL forw.
	3) MUFB1			Track in muon det. forw. or backw.
	4) DF11_I			HPC
	5) EMFBLO1			FEMC - deposit in forw. or backw.
DF07_II		2	1-2,1-3,	**Forw./Backw. Part 1**
	1) TPCFW_MJ1		1-4,2-3,	Track in TPC forw.
	2) TPCBW_MJ1		2-4,3-4,	Track in TPC backw.
	3) TRFW_MJ1		3-6,4-5,	Track in FCA/FCB forw.
	4) TRBW_MJ1		5-6	Track in FCA/FCB backw.
	5) MUFW_MJ1			Track in forw. muon chamb.
	6) MUBW_MJ1			Track in backw. muon chamb.
DF08_II		2	1-2,1-4,	**Forw./Backw. Part 2**
	1) TRFW_MJ1		2-3,3-4	Track in FCA/FCB forw.
	2) TRBW_MJ1			Track in FCA/FCB backw.
	3) EMFWLO1			Deposit in forw. FEMC, low thresh.
	4) EMBWLO1			Deposit in forw. FEMC, low thresh.

Table C.2: Example of the second level decision functions in 1994. First part.

Decision function	Components (TFs)	Level of coincidencies (*majorities*)	Forbidden coincidencies	Description
DF09_II		2	1-2,3-4	**Forw./Backw. Part 3**
	1) MUBB			Forw.-backw. track coincidence
	2) DF12_I			HCAL forw. or backw.
	3) TRFW_MJ1			Track in FCA/FCB forw.
	4) TRBW_MJ1			Track in FCA/FCB backw.
DF10_II		1		**Forw./Backw. Part 4**
	EMFWLO2			FEMC Forw., low thresh., mult. 2
	EMBWLO2			FEMC Backw., low thresh., mult. 2
	EMFBHI1			FEMC Forw. or Backw., high thresh.
	MUPARAL			Parallel muons
	DF14_I			Bhabha delayed + TPC laser
	DF15_I			Forw.-Backw. track coincidence
	B1_HOFBB			HOF back-to-back from B1
DF11_II		2	2-3	**Single tagged $\gamma\gamma$**
	1) TPCFWBW1			TPC Forw. or Backw.
	2) EMFBHI1			FEMC Forw. or Backw., high thresh.
	3) DF3_I			STIC single arm
DF12_II		2	1-2,1-3,	**HCAL*TOF**
	1) HAFWBWMULO		2-3	HCAL Forw. and Backw., muon thresh.
	2) HABLBBMULO			HCAL barrel back-to-back, muon thresh.
	3) HABLHI			HCAL single cluster, high thresh.
	4) TOF_MJ1			TOF
DF13_II		2		**HCAL and MUB**
	1) HABLHI			HCAL single cluster, high thresh.
	2) MUBLLC_MJ1			Hits in one octant of MUB
DF14_II		2	1-2,1-3,	**Forw./Backw. Part 5**
	1) (TRFW_MJ1)		2-4,3-4	Track in FCA/FCB and TPC Forw.
	*(TPCFW_MJ1)			
	2) (TRBW_MJ1)			Track in FCA/FCB and TPC Backw.
	*(TPCBW_MJ1)			
	3) TPCFW_MJ1			Track in FCA/FCB forw.
	4) TPCBW_MJ1			Track in FCA/FCB backw.
DF15_II	EMBLCOR_MJ1	1		**HPC T1*T2**

Table C.3: Example of the second level decision functions in 1994. Second part.

Appendix D

Trigger efficiency errors

To estimate the trigger efficiency errors one has to define the independent quantities. The simplest choice is:

$$N_a \equiv N_A - N_{AB}$$
$$N_b \equiv N_B - N_{AB}$$

and

$$N_{AB}$$

The graphic interpretation of this variables are shown in Fig.D.1. The above quantities

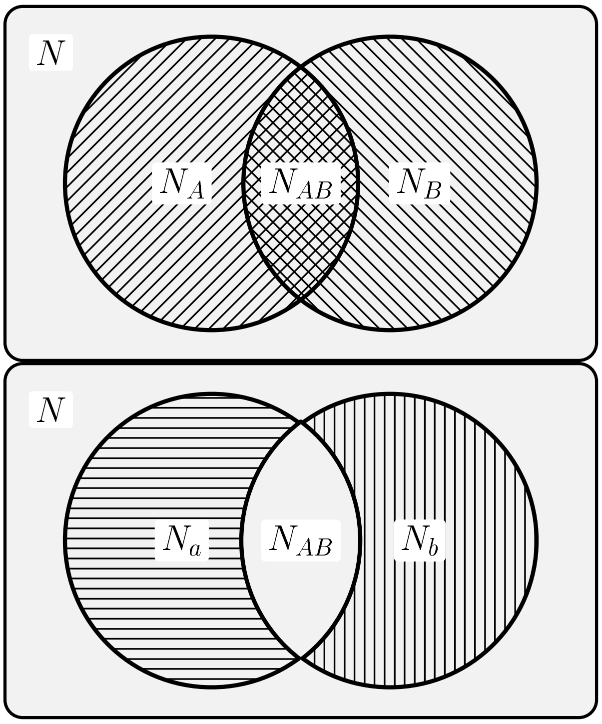

Figure D.1: Graphic definition of variables used in estimation of trigger efficiency and trigger efficiency errors.

are distributed according to the binomial distributions and the total efficiency error is found by applying the law of propagation of errors to equation:

$$\varepsilon_t = \varepsilon_A + \varepsilon_B - \varepsilon_A \varepsilon_B = \frac{N_{AB}(N_a + N_b + N_{AB})}{(N_a + N_{AB})(N_b + N_{AB})}$$

As a result the error of ε_t estimation is given by the expression:

$$\sigma_{\varepsilon_t} = \sqrt{\frac{1}{N\varepsilon_A\varepsilon_B}\left[D_1 + D_2 + D_3\right]}$$

where

$$D_1 = (1-\varepsilon_A)^2(1-\varepsilon_B)\varepsilon_B^3(1-\varepsilon_A+\varepsilon_A\varepsilon_B)$$

$$D_2 = (1-\varepsilon_B)^2(1-\varepsilon_A)\varepsilon_A^3(1-\varepsilon_B+\varepsilon_A\varepsilon_B)$$

$$D_3 = (1-\varepsilon_B)^2(1-\varepsilon_A)^2(1-\varepsilon_A\varepsilon_B)(\varepsilon_A+\varepsilon_B)^2$$

and

$$N = \frac{N_A N_B}{N_{AB}}$$

Bibliography

[1] Review of Particle Physics, Eur. Phys. J. C 3, 1-794 (1998).

[2] V.M.Budnev, I.F.Ginzburg, G.V.Meledin, V.G.Serbo, Phys. Rep. 15,181 (1975).

[3] J.Boyer et al., Phys. Rev. Lett. 56,207 (1986).

[4] H.Aihara, Phys. Rev. Lett. 57,404 (1986);
W.G.J.Langeveld, Ph.D. thesis, 1985.

[5] J.Dominick et al., Phys. Rev. D50,3027 (1994);
D.A.Acosta, Ph.D. thesis, University of California, San Diego, 1993.

[6] H.Kolanoski, *Two-Photon Physics at* e^+e^- *Storage Rings* , Springer Tracts in Modern Physics 105 (1984).

[7] M.Poppe, Int. J. Mod. Phys. A1,545 (1986)

[8] R.Nisius, Phys. Rep. 332,165 (2000).

[9] Ch.Berger and W.Wagner, Phys. Rep. 146,2 (1987).

[10] Physics at LEP2, CERN Yellow Report, CERN 96-01, Vol.1.

[11] Physics at LEP2, CERN Yellow Report, CERN 96-01, Vol.2.

[12] Phys. Rev. 120 (1960) 582.

[13] B.Muryn, First observation of the $\pi_2(1670)$ in $\gamma\gamma$ scattering, Scientific Bulletins of AGH, No. 1346

[14] J.Harjes, Ph.D. thesis, Hamburg University, 1991;
M.Feindt, Ph.D. thesis, Hamburg University, 1988;
T.Podobnik, Ph.D. thesis, Univerza v Ljubljani, 1995.

[15] I.Adachi et al., Phys. Lett. B234,185 (1990);
A.Courau et al., Phys. Lett. B147, 227 (1984);
Ch.Berger et al., Z. Phys. C26, 199 (1984);
H.Behrend et al., Z. Phys. C23, 223 (1984);
J.Boyer et al., Phys. Rev. D42, 1350 (1990);
A.Blinov et al., Z. Phys. C53,33 (1992);
F.Yabuki et al., J. Phys. Soc. Jap. 64, 435 (1995).

[16] D. Morgan et al., J. Phys. G.20, A1 (1994).

[17] M. Althoff et al., Phys. Lett. B121, 216 (1983); H.Albrecht et al., Z. Phys. C, 183 (1990).

[18] S.J.Brodsky, G.P.Lepage, Phys. Rev. D24,1808 (1981).

[19] S.J.Brodsky, G.P.Lepage, Phys. Rev. D22,2157 (1980).

[20] V.L.Chernyak, A.R.Zhitnisky, Phys. Rep. 112,173 (1984).

[21] V.M.Braun, A.Khodjamirian, M.Maul, Phys. Rev. D61, 073004 (2000).

[22] B.Nižić, Phys. Rev. D35,34 (1987).

[23] M.Benayoun, V.L.Chernyak, Nucl. Phys. B329,285 (1990).

[24] V.L.Chernyak, A.R.Zhitnisky, I.R.Zhitnisky, Nucl. Phys. B204,477 (1982).

[25] C.-R.Ji, F.Amiri, Phys. Rev. D42, 3764 (1990).

[26] Z.Dziembowski, L.Mankiewicz, Phys. Rev. Lett. 58,2175 (1987).

[27] G.von Holtey et al., CERN-SL/97-40

[28] P.Aarnio et al., Nucl. Instr. and Meth. A303,233 (1991).

[29] P.Abreu et al., Nucl. Instr. and Meth. A378,57 (1996).

[30] DELPHI www page

[31] J.A.Fuster, C.Lacasta, G.Valenti, J.A.Valls, DELPHI note 93-42, 1993.

[32] B.Bouquet, Ph.Gavillet, J-Ph.Laugier, DELPHI note 93-29, 1993.

[33] V.Bocci et al., Nucl. Instr. and Meth. A362,361 (1995).

[34] V.Canale et al., DELPHI note 99-7, 1999.

[35] DELPHI note, 89-44, 1989.

[36] DELPHI note, 91-85 PROG 176

[37] J.A.Vermaseren, Nucl. Phys. B229,347 (1983).

[38] R.Bhattacharya, J.Smith, G.Grammer, Jr., Phys. Rev. D15, 3267 (1977)

[39] H.Krasemann, J.A.M.Vermaseren, Nucl. Phys. B,269 (1981).

[40] F.A.Berends, P.H.Daverveldt, R.Kleiss, Comp. Phys. Comm. 40,271 (1986)

[41] F.A.Berends, P.H.Daverveldt, R.Kleiss, Nucl. Phys. B253,441 (1985)

[42] F.A.Berends, P.H.Daverveldt, R.Kleiss, Comp. Phys. Comm. 40,285 (1986)

[43] G.A.Schuler, Comput. Phys. Commun. 108,279 (1988); G.A.Schuler, CERN-TH-96-313.

[44] DELPHI notes: 87-96, 1989 and 87-98, 1989.

[45] DELPHI note, 96-133 RICH 90

[46] DELPHI note, 99-150 RICH 95

[47] DELPHI notes: 93-13 PHYS 262, 93-14 PHYS 263, 95-140 PHYS 565, 97-37 PHYS 690

[48] DELPHI note 96-82 PROG 217

[49] A.G.Frodesen, O.Skjeggestad, H.Tofte, Probability and statistics in particle physics.

[50] T.Camporesi et al., DELPHI note 97-08, 1997

[51] M.Dam, L.Bugge, DELPHI note 87-81, 1987

[52] M.Artuso et al., Phys. Rev. D50,5484 (1994);
A.Aihara et al., Phys. Rev. D36,3506 (1987);
H.Albrecht et al., Z. Phys. C 42, 543 (1989).

[53] G.Schuler, T.Sjostrand, CERN/TH/96-119

[54] G.A.Schuler, CERN-TH-96-297.

[55] C.Vogt, talk at the Photon 2000 conference, Ambleside, England 26th-31st August